

https://dspace.org/

Long distance data transfer using spatial modes of light

Gailele, Lucas Mushimanekgapi

2018

https://hdl.handle.net/10539/26895

Gailele, Lucas Mushimanekgapi, (2018) Long distance data transfer using spatial modes of light, University of the Witwatersrand, Johannesburg, https://hdl.handle.net/10539/26895

Downloaded from a DSpace repository. https://dspace.org/

UNIVERSITY OF THE WITWATERSRAND

MASTERS OF SCIENCE

Long distance data transfer using spatial modes of light

Author:
Lucas Mushimanekgapi
GAILELE

Supervisors:
Prof. Andrew FORBES
Dr. Angela DUDLEY



A dissertation submitted in partial fulfilment of the requirements for the degree of Master of Science

in the

Faculty of Science
School of Physics

Declaration of Authorship

I, Lucas Mushimanekgapi GAILELE, declare that this thesis titled, "Long distance data transfer using spatial modes of light" and the work presented in it are my own. I confirm that:

- This work was done wholly or mainly while in candidature for a research degree at this University.
- Where any part of this thesis has previously been submitted for a degree or any other qualification at this University or any other institution, this has been clearly stated.
- Where I have consulted the published work of others, this is always clearly attributed.
- Where I have quoted from the work of others, the source is always given. With the exception of such quotations, this thesis is entirely my own work.
- I have acknowledged all main sources of help.
- Where the thesis is based on work done by myself jointly with others, I have made clear exactly what was done by others and what I have contributed myself.

Signed:

Date:

UNIVERSITY OF THE WITWATERSRAND

Abstract

Faculty of Science
School of Physics

Master of Science

Long distance data transfer using spatial modes of light

by Lucas Mushimanekgapi GAILELE

Free space optical communication has been the subject of interest recently and has been identified as an alternative to fibre communication. Communication using the spatial modes of light is the focus of this dissertation. While propagating in free space, spatial modes are able to carry orbital angular momentum (OAM). OAM carrying spatial modes are orthogonal throughout their propagation and they span the discrete infinite dimensional Hilbert space allowing for (in theory) infinite information transfer to be carried throughout propagation. We are particularly interested in Laguerre-Gaussian (LG) modes and the azimuthal (Vortex) modes to send information. We discuss the principle of generating and detecting spatial modes by tailoring the dynamic phase of the spatial mode of light using a spatial light modulator (SLM). We will also characterized the communication link by giving a detailed overview of optical turbulence and how we measure the optical turbulence parameter. We will also give a link budget calculation describing the performance of the communication system.

Acknowledgements

Firstly, I am grateful to God for the strength and well being throughout my MSc study. I would like to express my sincere gratitude to my advisor Dr. Angela Dudley for the continuous support, for her patience, motivation, and immense knowledge. Her guidance helped me immensely. I could not have imagined having a better advisor and mentor for my MSc study. I also would like to thank Prof Andrew Forbes for his insightful comments and encouragement, but also for the hard question which incented me to widen my research and knowledge from various perspectives. Last but not the least, I would like to thank my family: my mother, brothers and sister for supporting me and all the dinners they have cooked for me and to also Prettier Maleka for her loving support and motivations throughout the writing of this thesis and my life in general.

Contents

Declaration of Authorship iii

Abstract v

Acknowledgements vii

1 Introduction 1
- 1.1 Motivation . . . 2
- 1.2 The paraxial wave equation . . . 3
- 1.3 The angular momentum of light . . . 7
  - 1.3.1 Laguerre-Gaussian beams . . . 8
- 1.4 Propagating fields in free space . . . 12
- 1.5 Propagating fields in turbulence . . . 15
  - 1.5.1 Kolmgorov model of turbulence . . . 15
  - 1.5.2 Beam wander . . . 21
  - 1.5.3 Scintillation . . . 23
- 1.6 Optical turbulence modelling . . . 25
  - 1.6.1 PAMELA Model . . . 26
  - 1.6.2 Hufnagel-Valley model . . . 27
  - 1.6.3 Polynomial regression model . . . 29

2 Experimental techniques 33
- 2.1 Spatial light modulators . . . 33
- 2.2 Calibration of a mid-IR SLM . . . 35
- 2.3 Generation of spatial modes . . . 40
- 2.4 Detection of spatial modes . . . 45

3 Link Characterization 49
- 3.1 Effects of the atmosphere on the power of a laser beam . . . 49
  - 3.1.1 Absorption and Scattering losses . . . 50
  - 3.1.2 Rain losses . . . 52
  - 3.1.3 Optical turbulence losses . . . 53
  - 3.1.4 Geometric losses . . . 54

3.2 Link budget analysis 56
3.2.1 Optical setup attenuation 58
3.2.2 Link budget calculation 59
3.3 Turbulence analysis 60

4 Data transfer over distance with spatial modes **67**
4.1 Data transfer analysis 67

5 Conclusions and future work **75**

A Matlab codes **77**

Bibliography **81**

List of Figures

1.1 Graph showing the increase of optical fibre capacity between 1980 and 2010 [4]. . . 2
1.2 Propagation of an optical field in a vacuum. Due to diffraction the wavefront will spread out upon propagation. 5
1.3 Simulated intensity distribution of Laguerre-Gaussian beams and corresponding phase masks. 9
1.4 A plot of the beam radius $w(z)$ as a function of the propagation distance z for (A) $w_0 = 1$ mm and (B) $w_0 = 10$ mm. 10
1.5 A plot of the radius of curvature as a function of the propagation distance for (A) $w_0 = 1mm$, (B) $w_0 = 10mm$, (C) $w_0 = 8m$ and (D) $w_0 = 160m$ 11
1.6 The Gouy phase is plotted as a function of propagation distance over a distance of $z = 150m$ with three different beam sizes (A), (B), (C) and (D). 12
1.7 Free space propagation of optical fields 13
1.8 (A) Gaussian beam propagated through (B) an aperture of 1 mm diameter. (C) The observed result at the transmitter plane. (D) The apertured beam was propagated and the intensity profile is seen at the receiver plane. 14
1.9 We can also simulate focusing and defocusing of (A) a Gaussian beam with a (B) lens of ($f = 1000$ mm) described by Eq 1.57. (C) and (D) At the far field a tight spot is observed. 15
1.10 Types of fluid flow: Laminar flow and Turbulent flow 16
1.11 Visual representation of the stages involved in order to have a turbulent environment. 17
1.12 The free space propagation of optical fields through a turbulent medium. 19
1.13 A simulation of a propagating field through a multiple turbulence phase screen. . . . 20
1.14 A LG mode with $p = 2$ and $l = 1$ was propagated through turbulence phase screens of (A) SR=0.91 and C=0,9201, (B) SR=0.5854 and C=0.5854 and (C) SR=0.10 and C=0.4420. Where C is abbreviation for correlation between received and transmitted images. 21
1.15 The beam wander effect due to the presence of large turbulence cells in the atmosphere which changes the direction of the beam as it propagates in free space. 22
1.16 small eddies affecting the beam as it is propagated through the atmosphere. 24
1.17 Simulation of the Rytov variance over a propagation distance for strong and weak turbulent conditions. 25

1.18 Calculated optical turbulence parameter versus time of day based on meteorological data for 1 November 2017. 27
1.19 Predicted optical turbulence parameter versus time of the day based on meteorological data for 1 November 2017 using the HV model. 29
1.20 Calculated optical turbulence parameter versus time of the day based on meteorological data for 1 November 2017 using the PR model. 31

2.1 The use of SPPs for generating OAM carrying beams. 34
2.2 A HoloEye SLM displaying the green circuit board and the LCD both connected by a flex cable. 34
2.3 The LCD crystals respond to the electric field applied across them. 35
2.4 (A) A simulation of how the phase will shift in response to varying the grey value on one half of the SLM. (B) the experimental setup that was followed in calibrating the SLM. 36
2.5 Blank hologram (a) and its correspond profile (d). Hologram with different phase depth (b) and its correspond intensity profile (e). The intensity profiles of the aperture beam with two beams (c) and without aperture (f). 38
2.6 This picture shows interference fringes as we vary the grey value on one half of the SLM. (A) shows the movement of the local maximum in intensity as we change the grey value before calibration and (B) shows the movements after calibration. 38
2.7 Plot of the measured focal length after the plane of the SLM versus programmed focal length. 39
2.8 (A) The effect of applying a grating on a beam will diffract light into its nth orders and (B) by having different shades of grey we can control light and give it the phase modulation we require. 41
2.9 Programmed SLM holograms displaying (A) blazed and (B) sinusoidal gratings. . . . 42
2.10 Creation of spatial modes using digital holograms. 43
2.11 A simple lab setup that we use to generate structured light. A laser beam illuminates a SLM that is programmed with a hologram that has a transmission function given by Eq 2.14. The lenses (Lens-1 and Lens-2) image the mode that was filtered by the aperture onto the CCD camera. 44
2.12 Experimentally generated LG modes 44
2.13 In a lab setup we detect spatial modes of light at the Fourier plane. (A) shows a case were no detection is made in which a null is seen at the center of the cross-hairs. (B) illustrates that a detection is made as a bright spot is seen at the center of the cross hair. 46
2.14 Decomposition of LG modes by variying the topological charge l and keeping radial index p constant. 47
2.15 Modal decomposition setup for detecting spatial modes. 47

3.1 Losses experienced by the laser beam propagating in the atmosphere. 49
3.2 The atmospheric absorption spectrum by various molecules in the atmosphere [61]. . 51
3.3 MODTRAN simulation of the fraction of radiation transmitted in the atmosphere as a function of wavelength. 51
3.4 A numerical simulation of the attenuation due to rain as a function of the rain rate. . . 53
3.5 A plot of the losses due to optical turbulence as a function of distance for a 532 nm laser propagating under different turbulence conditions. 54
3.6 (A) A plot of the theoretical geometric losses incurred in a link as a function of distance for beams of different divergence. (B) A plot of the theoretical geometric losses incurred in a link as a function of distance for different receiving apertures. 55
3.7 (A) A isotropic transmitter and (B) a directive transmitter sending signals in space. . 56
3.8 A theoretical graph for a communication link with a good link budget and as well as the losses incurred according to Eq 3.15. The red line shows the detectors sensitivity and the green line shows the power at the receiver. 57
3.9 (A) A plot of transmittance as a function of wavelength for uncoated fused silica [66] and (B) a plot of reflectance as a function of wavelength [67]. 59
3.10 In order to measure the optical turbulence parameter we sent a plane wave that interacted with Fried cells or turbulent eddies and captured using a 200mm lens which focused the beam onto the camera for analysis. 61
3.11 A comparison plot between (A) temperature (B) wind speed, (C) pressure and (D) humidity over 23^{rd} of November and 24^{th} of November 2017. 62
3.12 Diurnal measurement of the optical turbulence parameter compared with calculated values using various models (A) 23 November 2017 and (B) 24 November 2017. . . 63
3.13 Calculated versus measured C_n^2 values for (A) PR model, (B) PAMELA model and (C) HV model. 63
3.14 Shows the optical turbulence parameter for 24 November 2017. A plot between optical turbulence and wind speed (A), humidity (B) and temperature (C) was made. Temperature and humidity have a strong correlation with optical turbulence whereas wind speed has no known influence. 64
3.15 A density plot of the C_n^2 values is shown plotted as functions of temperature, wind speed and humidity 65
3.16 A plot of the Fried parameter on 23 November 2017. The relative errors between theory and measurement are plotted on the secondary axis. 65

4.1 (A) An angled view of the link between the two buildings at the CSIR. A retroreflector was used to reflect back the laser beam in to the lab for detection. (B) a Google Earth image showing the top view of the CSIR buildings over which the link is located. The distance between the two buildings was 75 m totalling 150 m. 68

4.2 We followed the schematics outlined to establish the communication link. Where L-lens, M-mirrors, F-focal length, C-Camera, Tx-transmitter and Rx-receiver. 69
4.3 (A) The two inch transmitter in the lab setup and (B) the window from which the laser was transmitted outside. 70
4.4 Decomposition results over (A) $z = 0m$ and (B) $z = 10m$ for both vortex and LG modes 70
4.5 Decomposition of LG modes for various p and l 71
4.6 LG decomposition results over the 150m link. The cross talk during day time was more severe compared to night time. a single measurement was averaged over 50 measurements to get result. 72
4.7 Simulation of data transfer using the crosstalk matrix that was over (A) 50 measurements and also (B) data transfer over a single measurement. The correlation between sent and received image was 0.9956 as compared to a single measurement with 0.8849. 73

A.1 Simulation code for sending information using the cross talk matrix 77
A.2 Code used to measure the optical turbulence parameter based on the Rytov theory . . 78
A.3 Optical field propagation code 79

Chapter 1

Introduction

The properties of light such as it's phase, polarisation and wavelength have all been modulated in current communication systems to increase bandwidth. Only recently has light's spatial degree of freedom been applied to optical communication. A class of spatial modes of light has been shown to posses orbital angular momentum (OAM). These modes possessing OAM can be characterized by a topological charge or the azimuthal index l which span an infinite dimensional space. We employed the orthogonality of Laguerre-Gaussian (LG) and Azimuthal modes to demonstrate free space data transfer over extended distance. In this chapter, we propose the use of the spatial modes of light as a way of sending information by first discussing the current state of the art communication systems and their limitations. We will also discuss the wave equation and its solutions giving rise to spatial modes. We will also discuss the influence of propagating spatial modes of light in turbulence and use three models to describe the strength of optical turbulence from meteorological data acquired from the South African weather service.

1.1 Motivation

We live in a technology driven world, where continents are connected via optical fibre that stretch for thousands of kilometres across the sea. Fast and reliable internet connections are desirable to support high definition (HD) online video streaming and large file downloads, which is provided by the current fibre optical systems. The current state of the art communication networks make use of the phase, polarization, and wavelength to transfer information in fibre. Researchers have also identified multiplexing schemes to maximize data transfer whereby multiple signals are sent over distinguishable channels simultaneously. Wavelength division multiplexing (WDM- encoding information in discernible wavelengths) [1], polarisation division multiplexing (PDM- encoding information in different polarization states) [2] and time division multiplexing (TDM- encoding information by means of synchronized switching of independent signals) [3] are the recognised techniques to maximise data transfer. Despite the established application of multiplexing techniques in fibre, the demand for high speed connection is continuing to grow at an astonishing scale.

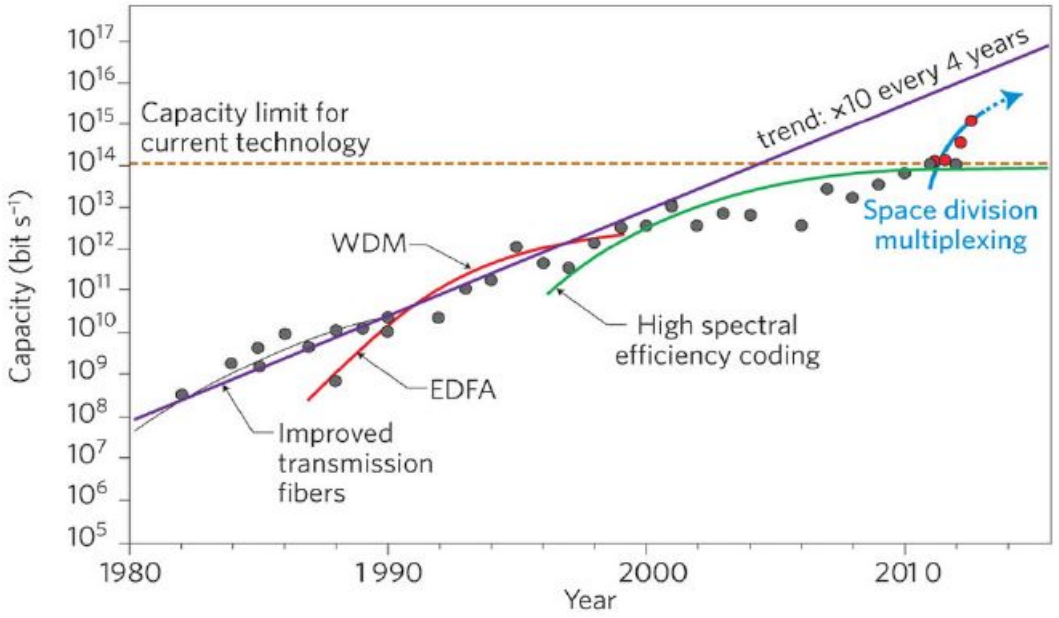


FIGURE 1.1: Graph showing the increase of optical fibre capacity between 1980 and 2010 [4].

Figure 1.1 shows the influence of technological developments in optical fibre ability to sustain the demand for high speed data transfer. The deployment of erbium doped fibre amplifiers (EDFA) which is able to amplify the signal upon propagation followed by WDM allowed the large data transfer supporting the high speed data connection. Optical fibres suffer from non-linear effects [4; 5], this has motivated researchers to introduce a novel techniques to operate above the limit (known as the Shannon limit [4]) called Space Division Multiplexing (SDM). In SDM, WDM and (MDM- mode division multiplexing- sending multiple of modes at the same time) are employed to send more information. Billions of internet users within the last mile (a term used to describe the "bottle neck"

limiting high speed connection between end users) is expected to grow. Free space communication (FSC) has emerged as a potential contender for point to point communication, bridging the connection between office and home users offering high speed connections. Despite making use of the properties of light to encode information, it is only recent that researchers have tapped into the previously unexplored degree of freedom found in the spatial modes of light. The spatial modes of light refers to the transverse profile of light's intensity distribution. About 25 years ago, Allen et al. discovered that LG modes will possess orbital angular momentum (OAM) [6]. LG modes are orthogonal as they propagate in free space. It is through this special property that we encode and send information in free space.

1.2 The paraxial wave equation

Maxwell's equations are used to describe the interaction of electromagnetic waves with matter. From these equations we derive the Helmholtz wave equation which governs the propagation of electromagnetic waves and apply the paraxial approximation to further simplify the Helmholtz equation [7]. Maxwell's equations are given by:

$$\nabla \cdot \vec{E} = \frac{\rho}{\epsilon}, \tag{1.1}$$

$$\nabla \cdot \vec{B} = 0, \tag{1.2}$$

$$\nabla \times \vec{E} = -\frac{\partial \vec{B}}{\partial t} \quad and \tag{1.3}$$

$$\nabla \times \vec{B} = \mu J + \varepsilon\mu \frac{\partial \vec{E}}{\partial t}. \tag{1.4}$$

In these equations $\vec{E}$ and $\vec{B}$ describe the electric field strength and the magnetic field displacement, respectively, of the electromagnetic wave as it propagates in free space. ϵ and μ represent the permittivity and the permeability constants. When considering the propagation of spatial modes in free space we assume a linear, homogeneous, isotropic, non-dispersive medium and in the absence of source currents.

$$\epsilon = \epsilon_0 \tag{1.5}$$

$$\mu = \mu_0 \tag{1.6}$$

$$\rho = 0 \tag{1.7}$$

$$\vec{J} = 0 \tag{1.8}$$

Maxwell's equations reduce to,

$$\nabla \cdot \vec{E} = 0, \tag{1.9}$$

$$\nabla \cdot \vec{B} = 0, \tag{1.10}$$

$$\nabla \times \vec{E} = -\frac{\partial \vec{B}}{\partial t}, \tag{1.11}$$

$$\nabla \times \vec{B} = +\varepsilon_0 \mu_0 \frac{\partial \vec{E}}{\partial t}. \tag{1.12}$$

The speed of light in a vacuum can be calculated directly from the two constants ε_0 and μ_0 shown by Maxwell from the following relationship [8]:

$$c = \frac{1}{\sqrt{\varepsilon_0 \mu_0}}. \tag{1.13}$$

By performing a cross product vector operation on Eq 1.11 and using the vector identity,

$$\nabla \times \left(\nabla \times \vec{E} \right) = \nabla \left(\nabla \cdot \vec{E} \right) - \nabla^2 \vec{E}, \tag{1.14}$$

$$\nabla \left(\nabla \cdot \vec{E} \right) - \nabla^2 \vec{E} = -\frac{\partial \left(\nabla \times \vec{B} \right)}{\partial t}. \tag{1.15}$$

Using Eq 1.9 and 1.12 and substituting them into Eq 1.15 we recover the well-known wave equation for waves propagating in free space,

$$\nabla^2 \vec{E} - \frac{1}{c^2} \frac{\partial^2 \vec{E}}{\partial t^2} = 0. \tag{1.16}$$

The electric field is time dependent and it is often desirable to separate it into its spatial and time components to reduce the rigorous complex mathematical analysis of the equation. We will employ the separation of variables technique which is also called the Fourier method that is often applied in solving ordinary partial differential equations to separate the electric field into its components. The idea behind this method is to express the arguments describing variables in our case, the electric field $\vec{E}(r,t)$, into its spatial $\vec{E}(r)$ and time $T(t)$ domains, where $r = (x, y, z)$ as

$$\vec{E}(r,t) = \vec{R}(r)\, T(t). \tag{1.17}$$

Substituting Eq 1.17 into Eq 1.16 and performing the necessary algebra will result in

$$\frac{\nabla^2 R(r)}{R(r)} = \frac{1}{c^2 T(t)} \frac{\partial^2 T(t)}{\partial t^2}. \tag{1.18}$$

This equation suggests that on both sides the two variables must be equal to the same value which is defined to be a constant given by $-k^2$. The constant k is related to the wavelength λ of the electromagnetic wave by $k = \frac{2\pi}{\lambda}$. Equating $-k^2$ to Eq 1.18 we obtain

$$\frac{1}{c^2 T(t)} \frac{\partial^2 T(t)}{\partial t^2} = k^2, \tag{1.19}$$

$$\frac{\nabla^2 R(r)}{R(r)} = -k^2, \tag{1.20}$$

and from Eq 1.20 we get,

$$\left(\nabla^2 + k^2\right) R(\vec{r}) = 0. \tag{1.21}$$

This equation is known as the time independent Helmholtz equation. It can be shown that it is equivalent to Schroedinger's equation for a quantum harmonic oscillator [9]. Considering an electromagnetic wave emanating from a laser, the propagation of the optical field or light can be visualized as shown in fig 1.2. The wave will propagate from a point z_0 to z along the z axis.

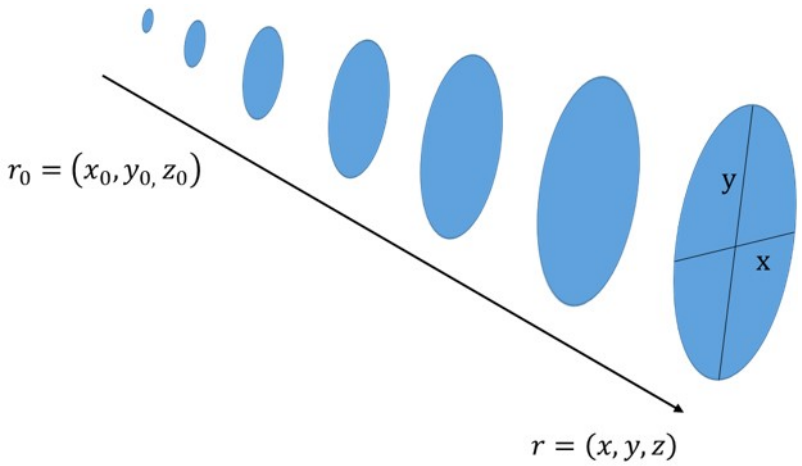


FIGURE 1.2: Propagation of an optical field in a vacuum. Due to diffraction the wavefront will spread out upon propagation.

The spatial position of the electric field assuming that it remains rotationally symmetric upon propagation, is given by $\vec{r} = (x - x_0, y - y_0, z - z_0)$ whose magnitude is,

$$r = \sqrt{(x - x_0)^2 + (y - y_0)^2 + (z - z_0)^2}. \tag{1.22}$$

The paraxial approximation dictates that the changes in the transverse plane (x, y) are very small when compared to the longitudinal (z) changes. Applying a power series expansion with respect to (z) from the point $(z_0 = 0)$ results in,

$$r \approx z + \left(\frac{x_0^2}{2z} + \frac{y_0^2}{2z}\right) + \left(\frac{x^2}{2z} + \frac{y^2}{2z}\right) + \left(\frac{xx_0}{z} + \frac{yy_0}{z}\right). \tag{1.23}$$

From Eq 1.23 we can assign a physical meaning to each term grouped in the brackets. The first term asserts the axial propagation of the electromagnetic wave from the point z_0 to z. The second term gives the curvature of the electric field at the transmitting end and the third term gives the curvature of the electric field at the receiving end. The fourth term is called the Fourier term. By assuming that the electric field can be described by a complex valued amplitude term U and a complex valued phase term given by $\exp(ikz)$,

$$E((x, y, z)) = U(x, y, z) \exp(ikz). \tag{1.24}$$

The Helmholtz equation reduces to,

$$\left(\frac{\partial^2}{\partial x^2} + \frac{\partial^2}{\partial y^2} + \frac{\partial^2}{\partial z^2}\right) U(x, y, z) + 2ik\frac{\partial U(x, y, z)}{\partial z} = 0. \tag{1.25}$$

The paraxial approximation further simplifies this equation by making the following assumption,

$$\left|\frac{\partial^2 U(x, y, z)}{\partial z^2}\right| \ll \left|2ik\frac{\partial U(x, y, z)}{\partial z}\right|, \tag{1.26}$$

and therefore further reduces the Helmholtz equation to the paraxial Helmholtz equation,

$$\left(\frac{\partial^2}{\partial x^2} + \frac{\partial^2}{\partial y^2}\right) U(x, y, z) + 2ik\frac{\partial U(x, y, z)}{\partial z} = 0. \tag{1.27}$$

This equation is the foundation of all fundamental light beams such as Gaussian beams and structured light beams (e.g. LG modes [6] and Bessel modes [10; 11]) which are recovered by solving Eq 1.27 in cylindrical co-ordinates. We will discuss the OAM of light and its origin, and the LG modes and Gaussian modes as solutions to the paraxial equation.

1.3 The angular momentum of light

The concept of angular momentum has long been known in physics [12]. Angular momentum can be categorized as either Spin Angular Momentum (SAM) which is intrinsic in nature or Orbital Angular Momentum (OAM) which can be either intrinsic or extrinsic [13; 14]. In this study we focus only on the OAM. All light fields with a phase term [6]

$$\varphi(\phi) = \exp(il\phi), \tag{1.28}$$

are known to carry OAM where ϕ is the angular angle and l is referred to as the topological charge or the azimuthal index. OAM refers to the twisting of the wavefront. The azimuthal index l can take on any positive and negative integer value i.e. $l = [...-1, 0, 1...]$. When the integer is given by e.g $l = -1$ the wavefront will twist in say the left direction and when it is given by $l = 1$ the wavefront will twist in the right direction. We will show that the OAM density is proportional to l. This will be achieved by calculating the Poynting vector of the beam described by,

$$\vec{S} = \frac{\vec{E} \times \vec{B}}{\mu_0}. \tag{1.29}$$

Considering only a linearly polarized beam along the $\hat{x}$ direction, the vector potential in the Lorenz gauge is given by

$$\vec{A}(x, y, z) = U(x, y, z) \exp(i(kz - \omega t))\,\hat{x}, \tag{1.30}$$

we can find the magnetic field and electric field are respectively given by,

$$\vec{B}(x, y, z) = \nabla \times \vec{A}(x, y, z) = ik \exp(i(kz - \omega t)) \left(U(x, y, z)\,\hat{y} + \frac{i}{k} \frac{\partial U(x, y, z)}{\partial y} \hat{z} \right), \tag{1.31}$$

$$\vec{E}(x, y, z) = \frac{ic^2}{\omega} \nabla \times \vec{B}(x, y, z) = i\omega \exp(i(kz - \omega t)) \left(U(x, y, z)\,\hat{x} + \frac{i}{k} \frac{\partial U(x, y, z)}{\partial y} \hat{z} \right), \tag{1.32}$$

The Ponyting vector given by Eq 1.29 can be calculated using the real components of Eqs 1.31 and 1.32 given by

$$\vec{E_{real}} = \frac{1}{2} \left(\vec{E} + \vec{E^*} \right) \tag{1.33}$$

and

$$\vec{B_{real}} = \frac{1}{2} \left(\vec{B} + \vec{B^*} \right). \tag{1.34}$$

Evaluating the Poynting vector we obtain,

$$\vec{S} = \epsilon_0 c^2 \left\langle \vec{E_{real}} \times \vec{B_{real}} \right\rangle = \frac{\epsilon_0 c^2}{4} \left(\vec{E} \times \vec{B^*} + \vec{E^*} \times \vec{B} \right) = \frac{\epsilon_0 \omega c^2}{4} \left(i(U \nabla U^* - U^* \nabla U) + 2k |U|^2 \hat{z} \right). \tag{1.35}$$

In cylindrical coordinates the field is given by $U(r,\theta,z) = U_0(r,z)\exp(il\theta)$. We find that the action of the Poynting vector along the azimuthal direction gives

$$S_r = 0, \tag{1.36}$$

$$S_\theta = \frac{l\omega\epsilon_0 U_0^2}{2r}, \tag{1.37}$$

$$S_z = k\epsilon_0\omega U_0^2. \tag{1.38}$$

The total angular momentum density is given by

$$L_z = \frac{1}{c^2}(r \times S)_z . \tag{1.39}$$

Substituting Eqs 1.36 ,1.37 and 1.38 we obtain the total OAM density which is given by

$$L_z = \frac{l\omega\epsilon_0 U_0^2}{2c^2}. \tag{1.40}$$

From Eq 1.40 we can see that the OAM density of the propagating field with an azimuthal dependence will have a well defined OAM that is proportional to the topological charge l.

1.3.1 Laguerre-Gaussian beams

LG modes are solutions to the paraxial equation with an azimuthal phase dependence. Mathematically LG modes are described by [6],

$$LG_{l,p,\psi}(r,z) = E_0 \exp\left(-\frac{r^2}{w^2(z)}\right)\exp\left(ikz + \frac{ikr^2}{2R(z)}(z)\right) L_p^{|l|}\left(\frac{2r^2}{\omega^2(z)}\right)\left(\frac{\sqrt{2}r}{\omega(z)}\right)^{|l|} \exp(il\theta)\exp(-i\Phi(l,p,z)), \tag{1.41}$$

where $\Phi(p,l,z)$ is known as the Gouy phase and is given by

$$\Phi(p,l,z) = (2p + |l| + 1)\arctan\left(\frac{z}{z_R}\right). \tag{1.42}$$

The radius of the curvature $R(z)$, beam size $w(z)$ are given by Eq 1.46 and 1.47 respectively and $k = \frac{2\pi}{\lambda}$ is the wave-number. The Laguerre polynomial term $L_p^{|l|}$ is embedded inside the LG mode function coupled with the Gaussian term, hence they are termed LG modes. The Laguerre polynomial term is responsible for the radial rings shown in fig 1.3. LG modes are characterised by the azimuthal index l and the radial index p. When the azimuthal index l is non-zero a null at the centre is observed in the intensity profile and the size of the null radius increases with l. The radial index introduces concentric rings around the null. If $p = 2$ the number of rings will be two around the

null. Figure 1.3 shows a simulation of LG modes with various l and p values with their corresponding

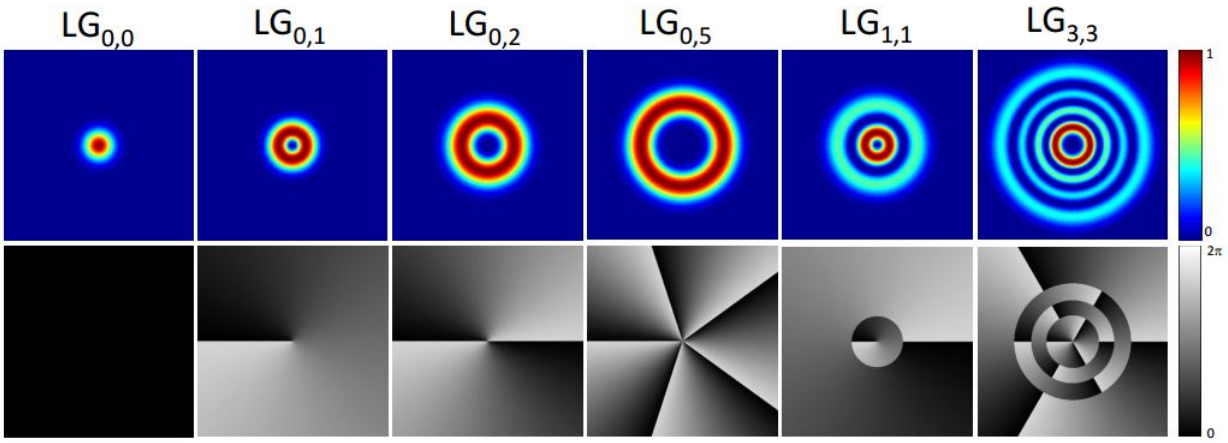


FIGURE 1.3: Simulated intensity distribution of Laguerre-Gaussian beams and corresponding phase masks.

phase profiles. When we set $p = l = 0$ we recover the Gaussian mode. The transverse plane of the mode can be modelled by the Gaussian distribution hence they are termed " Gaussian mode". It is important we know the size of the beam called the beam waist. This is the position where the width of the mode is at its minimum. At this position the intensity distribution at the centre of the beam is at its maximum value. As the beam propagates the intensity will start to decrease due to diffraction that all electromagnetic waves are prone to. The point where the intensity of the Gaussian is exactly half the value of the waist position, it is known as the Rayleigh range z_R where the waist is given by w_0 and the Rayleigh range is given by:

$$z_R = \frac{\pi w_0^2}{\lambda}. \tag{1.43}$$

In this project it was crucial to control the size of the beam at the receiver in order to collect the light. From Eq 1.43 it can be seen that the Rayleigh range is propotional to the square of the beam waist. Thus a larger beam waist will result in longer Rayleigh range compared to smaller beam waist. The electric field of a Gaussian mode at any position can be described mathematically by:

$$E(r,z) = \sqrt{I_0}\frac{w_0}{w(z)}\exp\left(-\frac{r^2}{w^2(z)}\right)\exp\left(ikz + \frac{ikr^2}{2R(z)} - i\psi(z)\right). \tag{1.44}$$

The electric field is used to express the intensity distribution of a mode which can be determined by calculating the modulus square of the electric field as given by:

$$|E(r,z)|^2 = I(r,z) = I_0\left(\frac{w_0}{w(z)}\right)^2\exp\left(-\frac{2r^2}{w^2(z)}\right), \tag{1.45}$$

where the radius of the beam as it propagates at a distance z is given by (assuming a waist at $z = 0$)

$$w(z) = w_0\left(1 + \left(\frac{z}{z_R^2}\right)^2\right)^{\frac{1}{2}}. \tag{1.46}$$

When $z = 0$, Eq 1.46 yields the beam waist w_0. Figure 1.4 is a plot of the beam radius as a function of the propagation distance. In Fig 1.4(A) a beam with a waist of $w_0 = 1$ mm is propagated over 150 m having a size of $w(150) = 25.42$ mm. When a beam is made ten times bigger i.e $w_{01} = 10w_0$ the beam size at $z = 150$cm is $w(150) = 10.32$ mm as seen in fig 1.4 (B). Therefore the effects of transmitting a beam with a large beam size increases the Rayleigh range. The radius of curvature is given by

$$R(z) = z\left(1 + \left(\frac{z_R}{z}\right)^2\right). \tag{1.47}$$

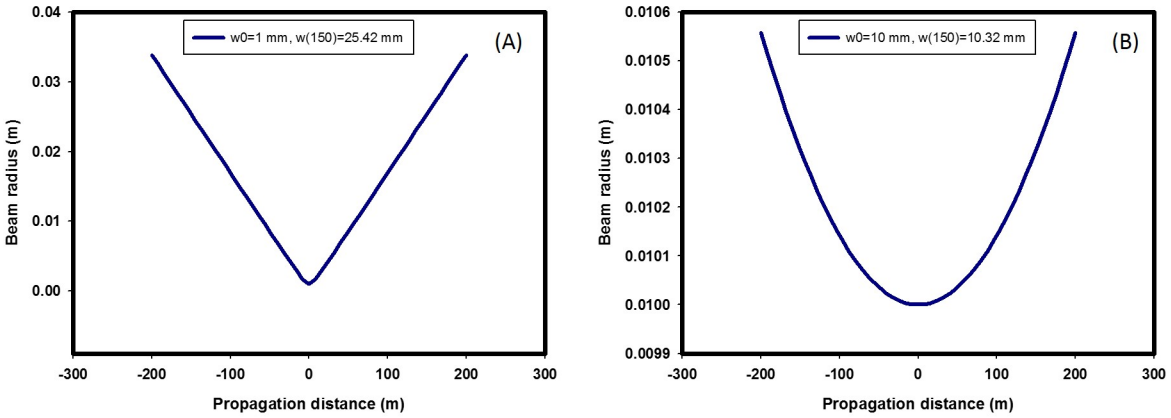


FIGURE 1.4: A plot of the beam radius $w(z)$ as a function of the propagation distance z for (A) $w_0 = 1$ mm and (B) $w_0 = 10$ mm.

If the radius of the curvature yields a value that is less than 0, it implies that the light rays will bend inwardly in the direction of propagation and when the value of the radius of curvature is greater than 1 the light rays will start to spread out in the direction of propagation. Ideally when we need a beam to travel a longer distance we need the beam to have approximately a flat wavefront meaning it is collimated. In Fig 1.5 (A) the radius of the curvature will remain approximatly flat over a distance of 5.91 m when the transmitted beam has a size of 1 mm. In Fig 1.5 (B) the radius of the curvature will remain approximately flat over a distance of 590.52 m when the transmitted beam has a size of 10 mm. In Fig 1.5 (C) the radius of the curvature will remain approximately flat over a distance of 377936 km when the transmitted beam has a size of 8 m, this means that the beam will be able to reach the moon with the size of the beam remaining the same. In Fig 1.5 (D) the radius of the curvature will remain approximately flat over a distance of 151.17 million km when the transmitted beam has a size of 160 m, this means that the beam will be able to reach the sun with the size of the beam remaining the same.

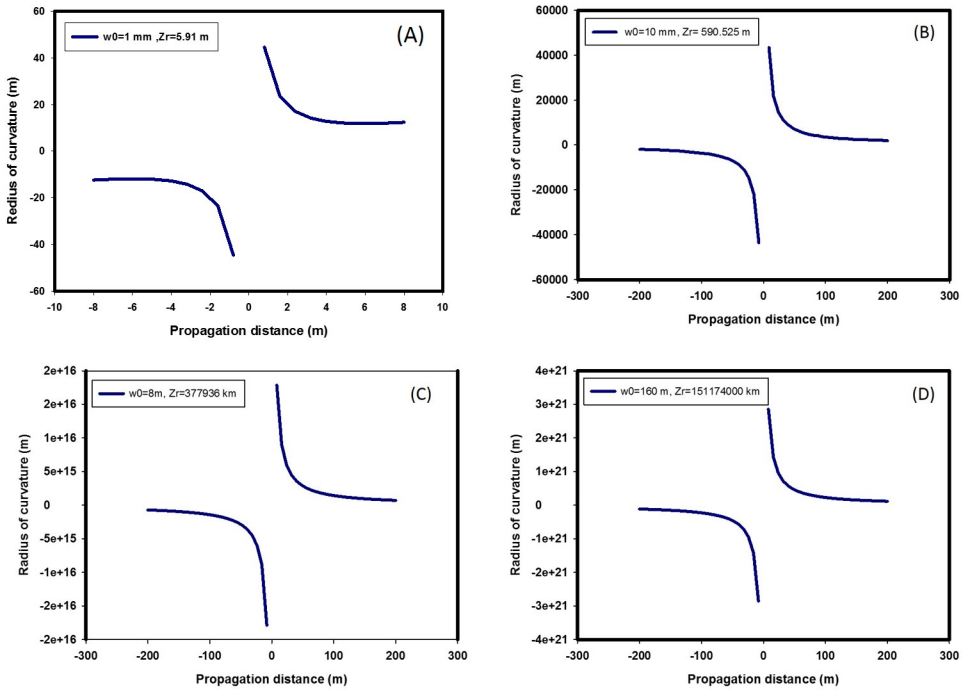


FIGURE 1.5: A plot of the radius of curvature as a function of the propagation distance for (A) $w_0 = 1mm$, (B) $w_0 = 10mm$, (C) $w_0 = 8m$ and (D) $w_0 = 160m$

Phase term ψ is known as the Gouy phase, and it is given by:

$$\psi(z) = \tan^{-1}\left(\frac{z}{z_R}\right). \tag{1.48}$$

In case of a Gaussian beam, a phase shift is acquired along the propagation axis z. This phase changes between $-\frac{\pi}{2}$ and $\frac{\pi}{2}$. Due to this the Gouy phase the wavefront will start to bend in the direction of propagation hence the beam will spread. Figure 1.6 (A) plots of the Gouy phase described by Eq 1.48 as a function of the propagation distance when $w_0 = 1$ mm. In fig 1.6 (A) the Gouy phase changes rapidly when the beam size is mean small. The Gouy phase will change slowly will the beam size is made large 1.6 (B),(C) and (D).

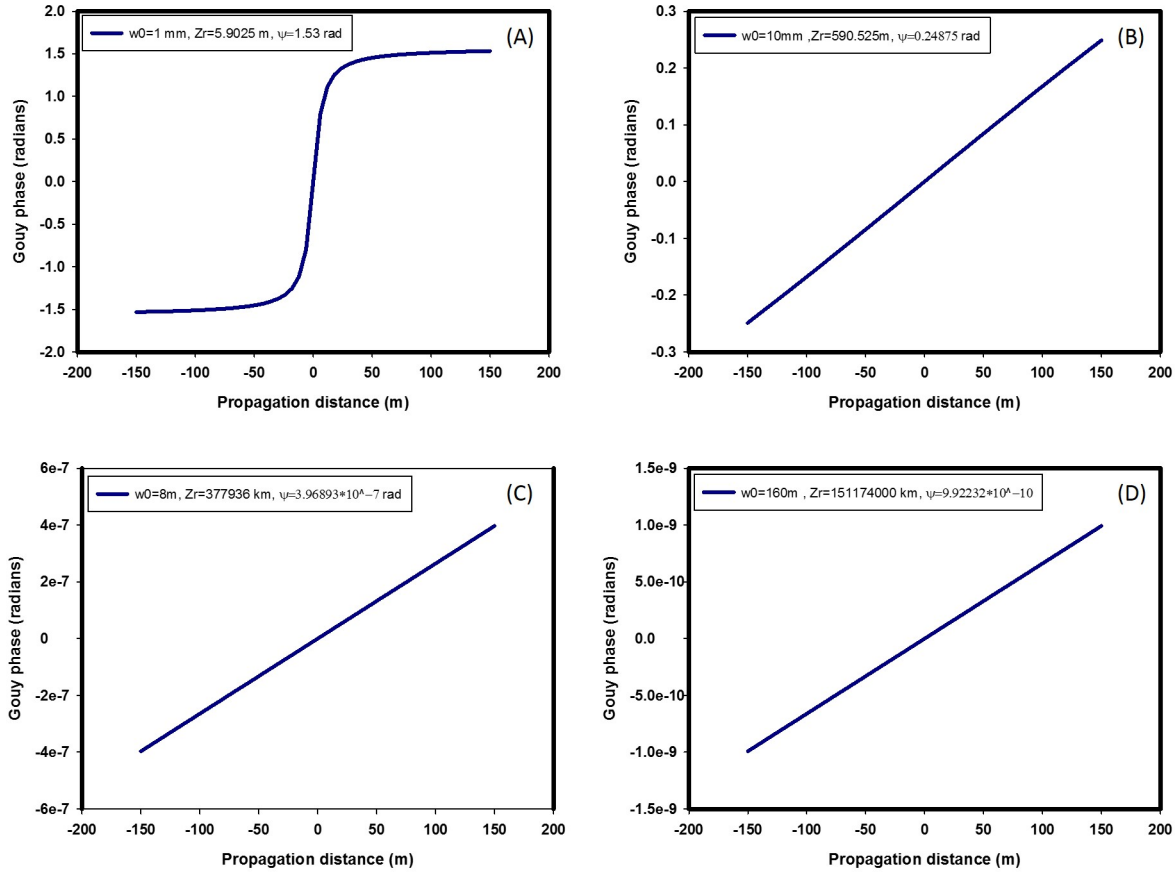


FIGURE 1.6: The Gouy phase is plotted as a function of propagation distance over a distance of $z = 150m$ with three different beam sizes (A), (B), (C) and (D).

1.4 Propagating fields in free space

It is important for us to know the behaviour of optical fields as they propagate in free space. This behaviour can be understood by the scalar diffraction theory. Considering free space propagation of optical fields in fig 1.7, the question we want to ask is: Given an optical field $U(x, y)$ at the transmitter plane, how will the field $U(u, v)$ look like at the receiver plane? Many approaches have been explored which make use of the Kirchoff-Sommerfeld theory [15] and other methods are based on the orthogonality of plane waves as they propagate in space [7]. However the idea is to calculate the field across the (x, y) plane which is parallel to the plane (u, v) at a distance z. The answer is given by the Huygens-Fresnel integral,

$$U(u, v) = \frac{z}{i\lambda} \int_{-\infty}^{\infty} \int_{-\infty}^{\infty} U(x, y) \frac{\exp(ikr)}{r^2} dxdy, \tag{1.49}$$

where r is the distance between the (x, y) plane and (u, v) plane given by:

$$r = \sqrt{z^2 + (x - u)^2 + (y - v)^2}. \tag{1.50}$$

Calculation of this integral does not yield an analytic solution and can only be solved using numerical techniques. To simplify Eq 1.49 we invoke the binomial expansion to Eq 1.50. For a given number $q << 1$ the expansion is given by:

$$\sqrt{1+q} = 1 + \frac{1}{2}q + \frac{1}{8}q^2 + \dots. \tag{1.51}$$

Eq 1.50 can be rewritten as:

$$r = z\sqrt{1 + \left(\frac{x-u}{z}\right)^2 + \left(\frac{y-v}{2}\right)^2}. \tag{1.52}$$

Applying the binomial approximation we obtain:

$$r \approx z\left[1 + \frac{1}{2}\left(\frac{x-u}{z}\right)^2 + \frac{1}{2}\left(\frac{y-v}{2}\right)^2\right]. \tag{1.53}$$

Substituting Eq 1.53 to Eq 1.49 we get the Fresnel integral given by:

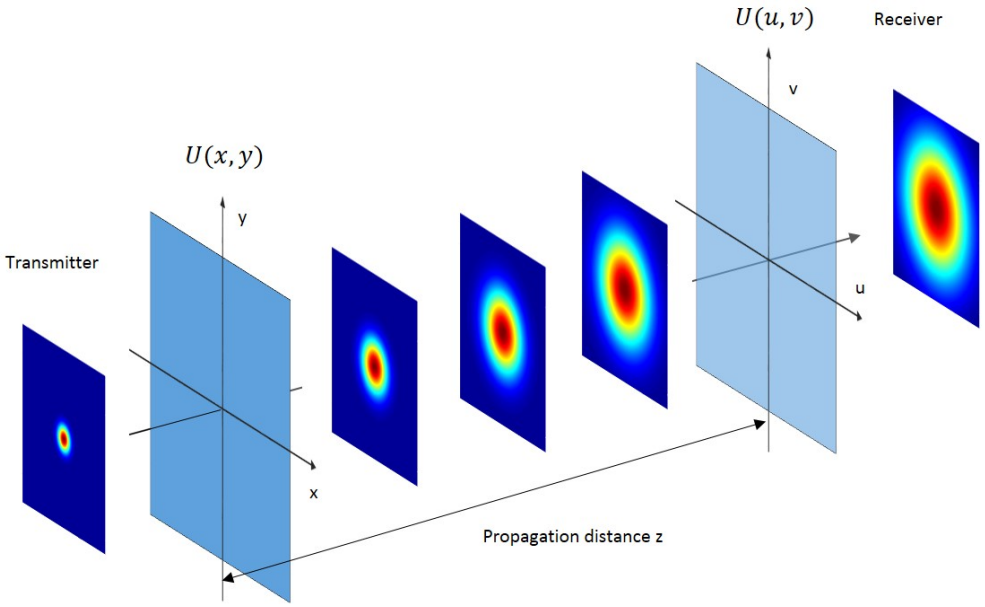


FIGURE 1.7: Free space propagation of optical fields

$$U(u,v) = \frac{\exp(ikz)}{i\lambda z}\int_{-\infty}^{\infty}\int_{-\infty}^{\infty} U(x,y)\exp\left(\frac{ik}{2z}\left[(x-u)^2 + (y-v)^2\right]\right)dxdy. \tag{1.54}$$

The Fresnel integral is useful in providing an approximation to the optical field at the receiver plane. It has found its uses in explaining how fields interact with different kinds of apertures. A Matlab script (found in Appendix A) was written to calculate the Fresnel integral to determine the optical field at the receiver plane after propagation from the transmitter plane. In fig 1.8 we have propagated

a Gaussian beam through a circular aperture of radius $w = 0.5$ mm. The aperture was defined to be

$$A(r) = circ\left(\frac{r}{w}\right), \tag{1.55}$$

where r is the radius coordinate at the transmitter plane. The mathematical expression used to define the apertured Gaussian beam is,

$$U(r, \theta, z) = LG_{0,0}(r, \theta, z) \times A(r), \tag{1.56}$$

and was substituted into the propagation integral Eq 1.54. In Fig 1.8 (A) the intensity profile of the Gaussian beam of waist $w_0 = 1$ mm is shown, where in fig 1.8 (C) the beam is aperture by an aperture of radius $w = 0.5$ mm shown in fig 1.8 (B). In Fig 1.8 (D) the propagation integral is used, where the beam is propagated over 150 m.

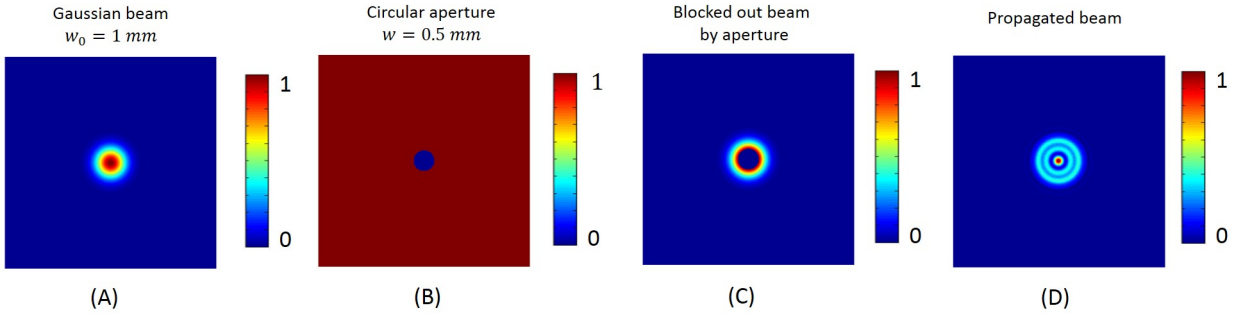


FIGURE 1.8: (A) Gaussian beam propagated through (B) an aperture of 1 mm diameter. (C) The observed result at the transmitter plane. (D) The apertured beam was propagated and the intensity profile is seen at the receiver plane.

We can also use the Fresnel diffraction integral to simulate the focusing of beams. The mathematical function used to describe a lens of focal length f is given by:

$$A(r) = \exp\left(\frac{ikr^2}{2f}\right) \tag{1.57}$$

The effect of the lens function focuses the beam (fig 1.9 (A))at focal length f (fig 1.9 (C) and (D)). The phase of a lens function is shown in fig 1.9 (B). The propagation integral can also be used to propagate optical fields through a turbulent medium. In the next section, we will discuss the origin of optical turbulence, its implication on an optical field and also use the propagation integral to simulate the free space propagation of a field in a turbulence medium.

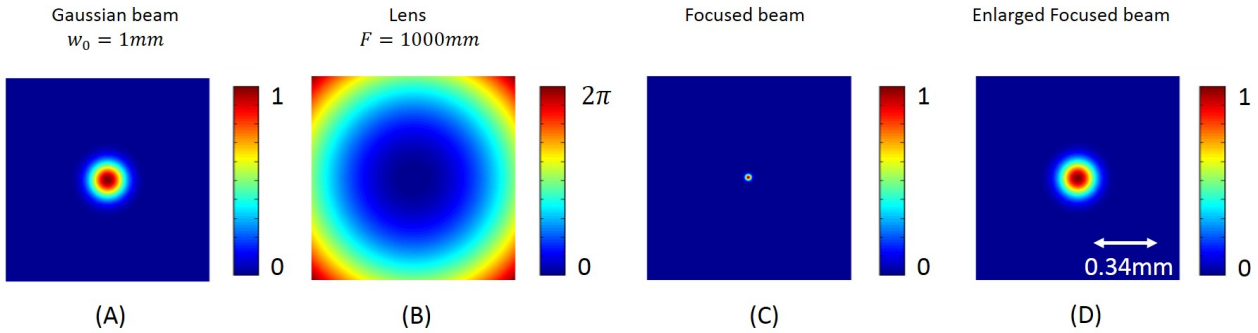


FIGURE 1.9: We can also simulate focusing and defocusing of (A) a Gaussian beam with a (B) lens of ($f = 1000$ mm) described by Eq 1.57. (C) and (D) At the far field a tight spot is observed.

1.5 Propagating fields in turbulence

All light waves having different wavelengths will experience turbulence differently due to the size of the atmospheric cells [16]. Literature suggests that for short wavelengths that are comparable to the size of particles found in the atmosphere they will experience some propagation effects that are due to scattering [17], absorption [18], fog [19] and refractive index fluctuation effects known as optical turbulence [20]. Light fields will always experience some form of turbulence as they propagates in free space and this is due to fluctuations in temperature, humidity, pressure and wind velocity. In order to model light fields propagating in free space under a random media the time independent Helmholtz equation can be written in the form,

$$\nabla^2 \vec{E} + k^2 n^2 \left(\vec{r}\right) \vec{E} = 0. \tag{1.58}$$

Where k is the wave number, $\vec{E}$ is the electric field of the propagating field and $n\left(\vec{r}\right)$ is known as the index of refraction of the medium and is a function of the displacement vector $\vec{r}$. There are a plethora of methods that can be employed to solve Eq 1.58 using approximation methods, however two favourable approaches have been used extensively. The first approach is the Born approximation, this method has also been employed in the scattering problem in quantum theory. Rytov extended the Born approximation to solve Eq 1.58 to best describe weak turbulence conditions [21; 22] and it was later extended to describe the strong condition by Andrews [21]. To best describe the strong turbulence conditions, the parabolic approximation method was used to solve Eq 1.58 but it was limited and failed to include the forth order statistics needed for calculating the scintillation index [21].

1.5.1 Kolmgorov model of turbulence

We can picture the atmosphere as a viscous fluid that has two particular states of motion, namely laminar and turbulent states. In the laminar flow, the velocity flow is uniform and is directional and

all changes in the flow are the same. In the turbulent flow, the velocity flow changes rapidly and the uniformity is lost due to dynamic mixing and turbulent eddies start forming as shown in fig 1.10. The change from laminar to turbulent motion can be described by the non-dimensional quantity known as the Reynolds number.

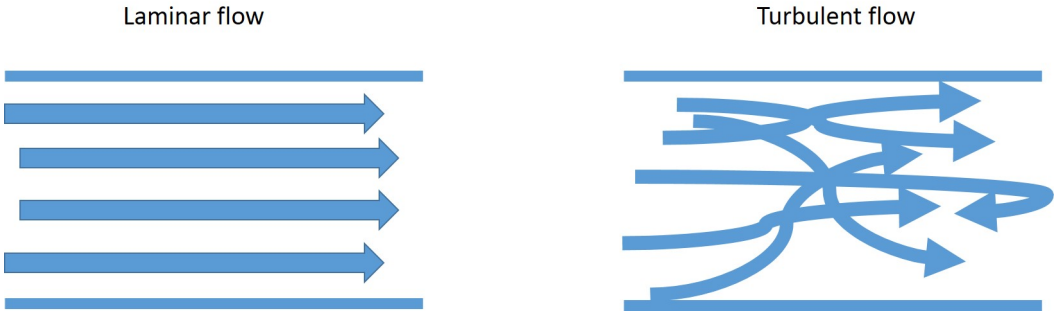


FIGURE 1.10: Types of fluid flow: Laminar flow and Turbulent flow

The Reynolds number is defined as

$$Re = \frac{V l_f}{v_k}, \tag{1.59}$$

where V is the characteristic velocity (m/s) of the fluid, l_f is the dimension of flow (m) of the fluid, and v_k is the kinematic viscosity (m^2/s). The Reynolds number (unitless) can be used to determine if a flow in a fluid is laminar or turbulent. When the $Re < 2300$ the flow is said to be laminar. When $Re > 4000$ the fluid is said to be turbulent. In the atmosphere we find that $Re > 4000$ which if we model air as a fluid we find it to be turbulent. Air masses will have different properties (temperature, pressure and humidity) that are independent of the original air mass or parent air mass. Under pressure or inertial forces the large scale eddies of length (L_0-size of the big air cells) will start to break apart into smaller scale eddies of length (l_0-size of small air cells). The large eddies and small eddies are also called the outer scale and inner scale respectively. Figure 1.11 shows a visual representation of the processes involved in a turbulent environment. The outer scales are of the order 10 to 100 m and increase as we move above ground. The inner scale l_0 is of the order 1 mm to 10 mm near the ground [21]. Scale sizes smaller than l_0 are said to be in the dissipation range. In the dissipation range the turbulent eddies get destroyed and the energy will be dissipated in the form of heat. In the Kolmogorov theory of turbulence [23; 24] the small scale l_0 is assumed to be 0 and the large scale $L_0 = \infty$. The energy cascade is shown in fig 1.11. Kolmogorov developed a mathematical model for turbulence and its effects on the optical beam propagating in space. He assumed that the random fluctuations in the atmosphere are a stationary random process having statistically homogeneous and isotropic characteristics. He discovered that in the inertial sub-range the structure function follows the two thirds power law $r^{\frac{2}{3}}$ where r is the spatial scale between two points given by,

$$r = |\vec{r_1} - \vec{r_2}|, \qquad l_0 \leq r \leq L_0 \tag{1.60}$$

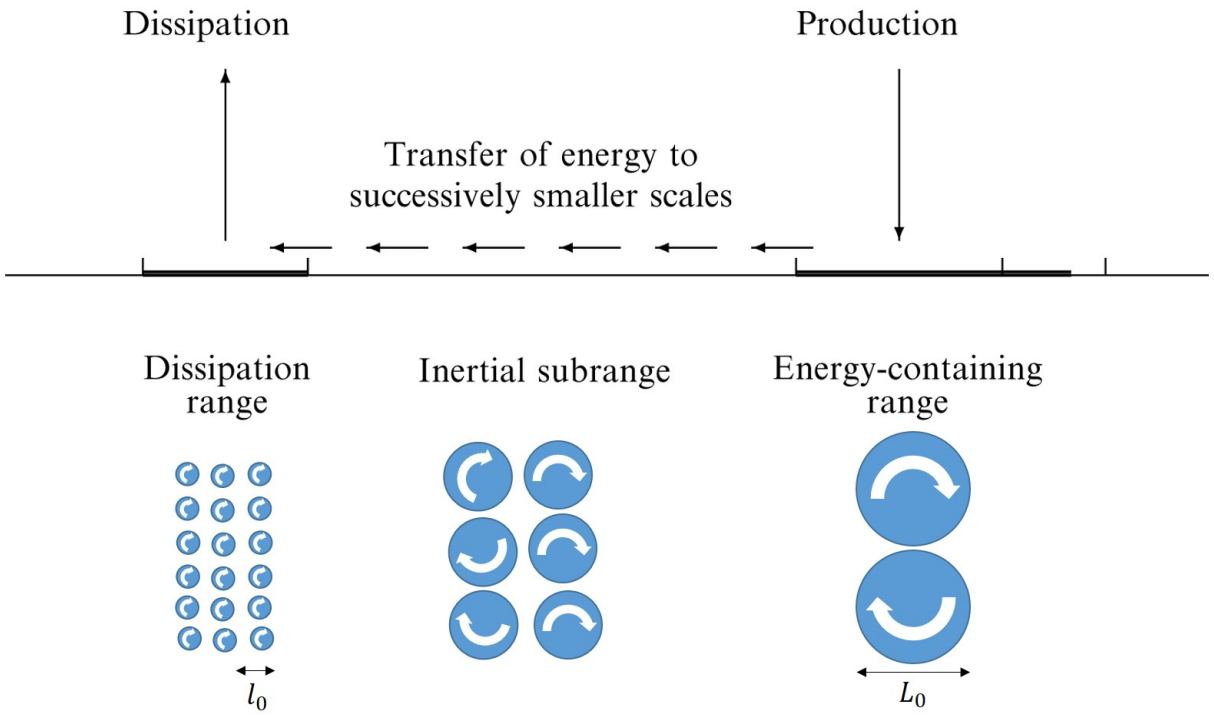


FIGURE 1.11: Visual representation of the stages involved in order to have a turbulent environment.

The structure function of any random variable $m(r)$ can be given as

$$D_m\left(r_{(m)}\right) = D_m\left(f\left(\vec{r_1}, \vec{r_2}\right)\right) = \left\langle \left| m\left(\vec{r_1}\right) - m\left(\vec{r_2}\right)\right|^2 \right\rangle . \tag{1.61}$$

The variable $m(r)$ can be assumed to have the first moment and overlayed or superimposed fluctuating components that are represented as

$$m(r) = \langle m\left(\vec{r}\right)\rangle + m^{'}\left(\vec{r}\right). \tag{1.62}$$

Combining Eq 1.61 and Eq 1.62 the structure function becomes

$$D_m\left(r_{(m)}\right) = \left\langle \left| m^{'}\left(\vec{r_1}\right) - m^{'}\left(\vec{r_2}\right)\right|^2 \right\rangle + \left\langle \left| m\left(\vec{r_1}\right) - m\left(\vec{r_2}\right)\right|^2 \right\rangle . \tag{1.63}$$

The most important result from Eq 1.63 is that the second term reduces to zero for a stationary random process which leads to having only the rate of change in the spatial scales of the random variable $m(r)$ which gives the structure function for wind velocity

$$D_v\left(r_v\right) = \left\langle \left(v_1 - v_2\right)^2 \right\rangle = C_v^2 r^{\frac{2}{3}} \qquad l_0 \leq r \leq L_0. \tag{1.64}$$

Where v_1 and v_2 are the velocities at two spatial points separated by a distance r and C_v^2 is the velocity structure constant which measures the amount of energy in the turbulent atmosphere. Following a

similar fashion it can be shown that the structure constant for temperature is given by

$$D_t\left(r_t\right) = \left\langle \left(t_1 - t_2\right)^2 \right\rangle = C_t^2 r^{\frac{2}{3}} \qquad l_0 \leq r \leq L_0. \tag{1.65}$$

Another important structure function is due to the refractive index n. Variations in pressure and temperature along the propagation distance in the atmosphere will induce air masses with different refractive indices. The refractive index at any point along the propagation distance can be given by:

$$n\left(r\right) = n_0 + n^{'}\left(r\right) \tag{1.66}$$

where $n_0 \approx 1$ is the first moment of the index of refraction. The relationship between pressure and temperature to the index of refraction in the atmosphere is given by

$$n\left(r\right) = 1 + 79 \times 10^{-6} \left(\frac{P^{'}\left(r\right)}{T^{'2}\left(r\right)}\right), \tag{1.67}$$

where the pressure $P^{'}$ is measured in $mbar$ and the temperature $T^{'}$ is measured in K. Scattering and absorption by the air particles and molecules are not taken into account in the expression. Again following a similar derivation one can show that the structure function for the index of refraction is given by

$$D_n\left(r_n\right) = \left\langle \left(n_1 - n_2\right)^2 \right\rangle = C_n^2 r^{\frac{2}{3}} \qquad l_0 \leq r \leq L_0. \tag{1.68}$$

Where C_n^2 is called the refractive index structure constant which measures the strength of optical turbulence. This constant is considered important when characterizing atmospheric turbulence although it is also dependant on the size of the transmitted beam and the size of the eddies.

In the Born approximation, an approximate solution can be given by writing the field $U\left(\vec{r}\right)$ as a superposition of individual fields that are perturbed by the medium (atmosphere) in which it propagates

$$U\left(\vec{r}\right) = U_0\left(\vec{r}\right) + U_1\left(\vec{r}\right) + U_2\left(\vec{r}\right) + ... \tag{1.69}$$

In this case the field $U_0\left(\vec{r}\right)$ represents the unperturbed field or a field travelling in a vacuum or free space. While $U_1\left(\vec{r}\right)$ and $U_2\left(\vec{r}\right)$ denote first-order, second-order, and so on, perturbations caused by inhomogeneities due to the random term $n\left(r\right)$. The Born approximation was historically applied to very weak turbulence theory, however the Rytov approximation proved to be an improved approximation theory in the weak turbulence regime. The mathematical foundation lead by Rytov is used extensively throughout this work especially in the measurement of the turbulence strength measurement C_n^2. The Rytov variance is given by [21]

$$\sigma_R^2 = 1.23 C_n^2 k^{\frac{7}{6}} L^{\frac{11}{6}}, \tag{1.70}$$

where L is the propagation distance of our free space link. The strength of optical turbulence along

the link is measured by the C_n^2 values. These values are typically of the order $> 10^{-13}$ for strong turbulence and of the order $< 10^{-15}$ for weak turbulence. On hot days C_n^2 is relatively high and peaks at noon and low on cold days and in the afternoon. It is desirable to simulate optical fields propagating in a turbulent environment. We will extend the theory in propagating optical fields in free space by multiplying the output beam at the transmitter with turbulence phase screens. The phase screen model is the most popular model to simulate beam propagation in a turbulent medium. This model only takes into account phase modulations as the beam travels in space. The idea behind this is depicted in fig 1.12. The input beam at the transmitter located at $z = 0$ is propagated to the reciever located at $z = L$. In this model the assumption is that there exist random phases screens, in different planes say L_1, L_2 until $L = L_1 + L_2 + L_3 + \ldots$ where the phase of the optical field will be modulated. The production of the turbulence phase screen is based on the Kolmogorov power-law spectrum. As the wave propagates in a medium with fluctuations in temperature, humidity and wind speed the refractive index will also change. The power spectral density for the refractive index is given by [25],

$$\Phi_n(\kappa) = 0.033 C_n^2 \kappa^{-\frac{11}{3}}, \qquad \frac{1}{L_0} << \kappa << \frac{1}{l_0} \tag{1.71}$$

where κ is the scalar wave number.

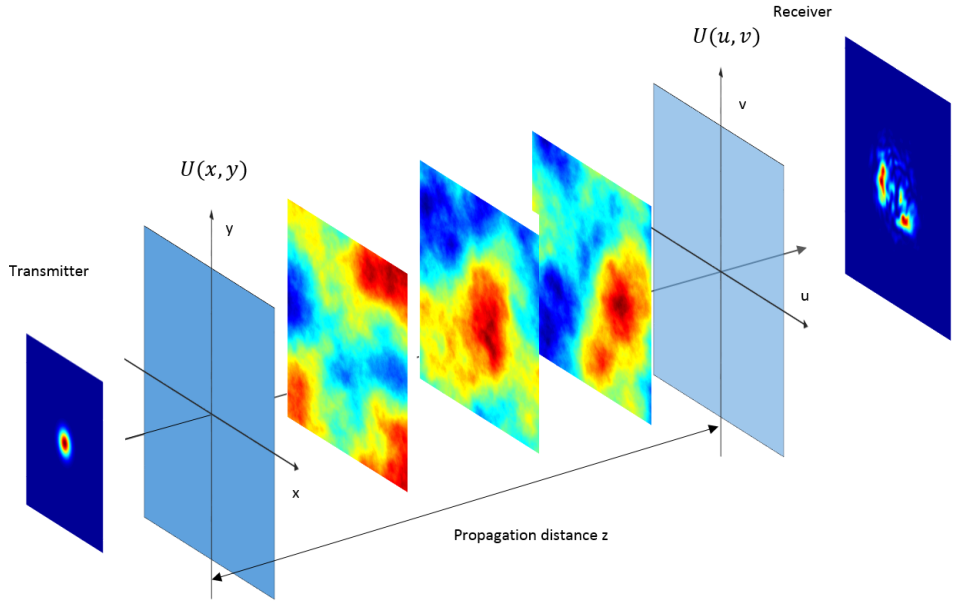


FIGURE 1.12: The free space propagation of optical fields through a turbulent medium.

By incorporating the Kolmogorov model together with the expression of the Strelh ratio (SR) Eq 1.72 in Matlab (found in Appendix A), we were able to generate phase screens as shown in fig 1.13. The SR is calculated from the optical turbulence parameter. The Strehl ratio is the measure of the

formation of image quality and it is given by,

$$SR = \frac{1}{1 + 6.88(\frac{W_0}{r_0})^{5/3}} \tag{1.72}$$

with W_0 given as the beam radius and r_0 is the Fried parameter defined as the extent to which the phase of the beam will not change. The Strelh ratio is normalised to 1 and takes on values between 0 and 1. By adjusting the SR we simulated strong (SR=0.10), moderate (SR=0.56) and weak (SR=0.91) turbulence conditions. The effects of propagating the LG_{12} spatial mode is shown in fig 1.13, where the phase of the mode is modulated resulting in a beam that is shorter than its initial starting mode. We calculated the correlation between the optical field at the receiver and the optical field at the transmitter to determine the mode purity of the modulated beam. A stronger correlation was seen

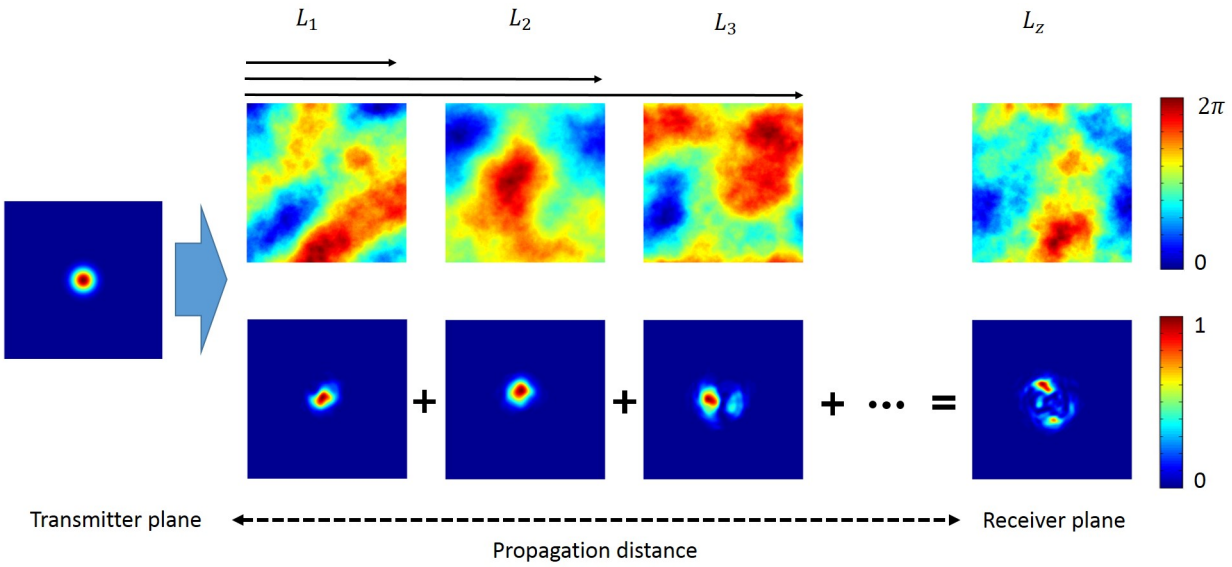


FIGURE 1.13: A simulation of a propagating field through a multiple turbulence phase screen.

when the SR was close to 1 (weak turbulence)and the correlation was low when the SR was close to 0 (strong turbulence). The propagation of the optical field through turbulence was simulated as shown in fig 1.14. The idea was to propagate the field according to Eq 1.54 through multiple phase screens. The resulting optical field is shown in fig 1.14. The effects of turbulence can be classified individually by perturbations from the small and large eddies found in the atmosphere. These effects are known as beam wander and scintillation.

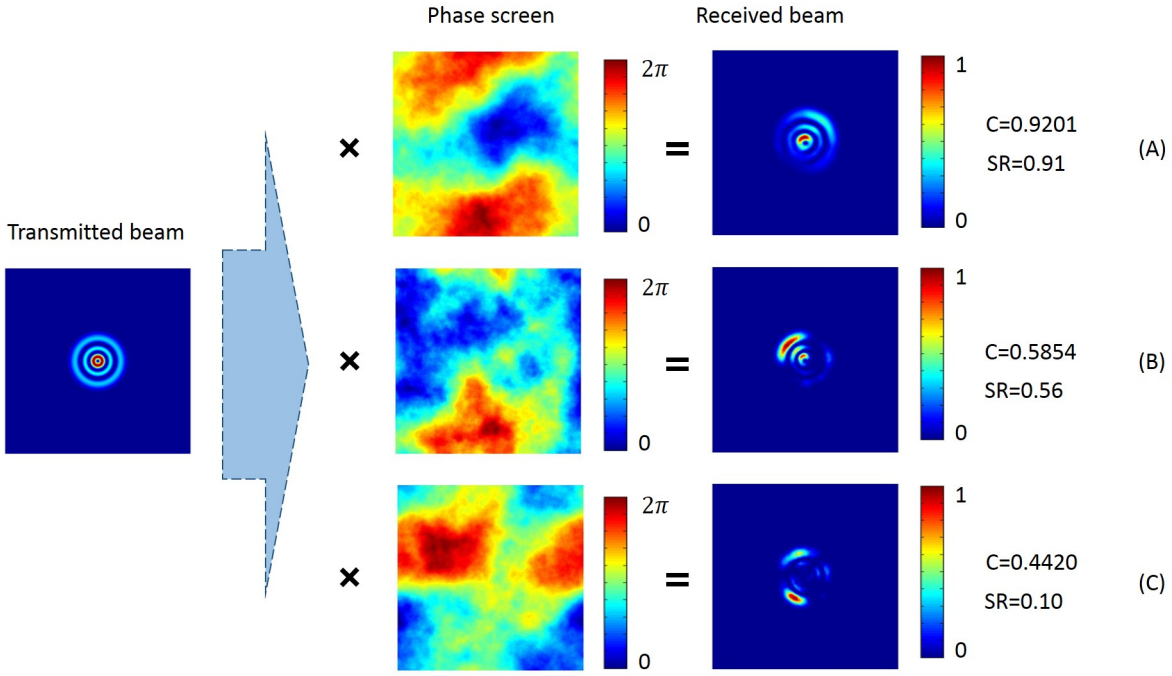


FIGURE 1.14: A LG mode with $p = 2$ and $l = 1$ was propagated through turbulence phase screens of (A) SR=0.91 and C=0,9201, (B) SR=0.5854 and C=0.5854 and (C) SR=0.10 and C=0.4420. Where C is abbreviation for correlation between received and transmitted images.

1.5.2 Beam wander

The beam wander can be described as the wandering of the point of maximum irradiance over the receiver plane, also known as the "hot spot". This phenomenon is caused by the large-scale eddies that are inhomogeneous due to their different refractive effects [21]. When a Gaussian beam propagates through a turbulent atmosphere the large scale eddies corrupt the instantaneous optical field [26; 27]. The movement of the hot spot about the center of the detector over a long period of time (averaged) will result in a beam that has a large area also known as the long term beam size. The long term beam size is a result of the beam wander effect, the natural free space diffraction spreading and also additional perturbations by atmospheric eddies that are much smaller than that of the transmitted beam size [28]. Figure 1.15 illustrates the manifestation of beam wander that is observed at the receiver as the beam propagates in large eddies. The effects caused by beam wander can be used to study the intensity profile along the propagation path. The beam wander variance can be mathematically described as [25],

$$\left\langle r_c^2 \right\rangle = W_{LT}^2(r) - W^2(r) - W^2(r)\, T_{ss}, \tag{1.73}$$

where

$$W_{ST}^2(z) = W^2(z) + W^2(z)\, T_{ss}, \tag{1.74}$$

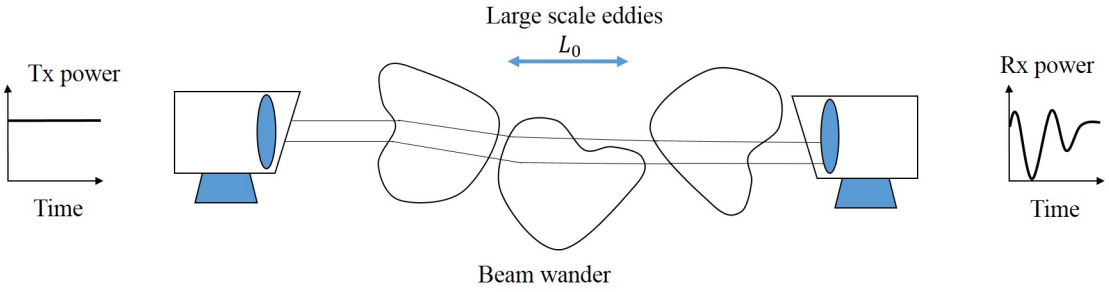


FIGURE 1.15: The beam wander effect due to the presence of large turbulence cells in the atmosphere which changes the direction of the beam as it propagates in free space.

and in short

$$\left\langle r_c^2 \right\rangle = W_{LT}^2(z) - W_{ST}^2(z). \tag{1.75}$$

Here $W^2(z)$ is the beam spot size after propagating a distance z and T_{ss} is known as the short-scale spread of the beam that is caused by small eddies that are shorter than the beam size. It was also shown that the general spectral power law value has a significant influence on the Gaussian beam [29]. Following the Rytov method for modelling turbulence we can calculate the long term beam radius as [25],

$$W_{LT}^2(z) = W^2(z)\left[1 + 1.33\sigma_R^2\Gamma^{\frac{5}{6}}\right], \quad \Gamma = \frac{2L}{kW^2(z)}, \tag{1.76}$$

where L is the link distance and σ_R^2 is the Rytov variance. The short term beam radius W_{ST} can be calculated as follows

$$W_{ST}^2(z) = W^2(r)\left[1 + 1.33\sigma_R^2\Gamma^{\frac{5}{6}}\left[1 - 0.66\left(\frac{\Gamma_0^2}{1+\Gamma_0^2}\right)^{\frac{1}{2}}\right]\right], \qquad \Gamma_0 = \frac{2L}{kW_0^2}. \tag{1.77}$$

For free space communication links that are from the ground to space the beam wander equation still holds. The beam wander variance for a collimated beam is given by [21]

$$\left\langle r_c^2 \right\rangle = 7.25(H - h_0)^2 sec^3(\theta) W_0^{-1/3} \int_{h_0}^{H} C_n^2(h)\left(1 - \frac{h - h_0}{H - h_0}\right)^2 dh, \tag{1.78}$$

where the refractive index structure parameter is given as $C_n^2(h)$ for a beam with size W_0 at the transmitter and H and h_0 are the height above ground for the receiver in space and the transmitter near the ground respectively at an angle θ. It was seen that the beam wander effects are small when the beam is transmitted from space to the receiver based on the ground [30]. This is due to the fact that the beam size as it reaches the earth is large when compared to large turbulent eddies. Equation 1.78 can be further reduced when we introduce h_0 (height above ground from the transmitter) and

$H = h_0 + Rcos\,(\theta)$ to [31]

$$\left\langle r_c^2 \right\rangle = 0.54(H - h_0)^2 sec^2\,(\theta) \left(\frac{\lambda}{2W_0}\right)^2 \left(\frac{2W_0}{r_0}\right)^{\frac{5}{3}} \tag{1.79}$$

where r_0 is known as the atmospheric coherence length or Fried parameter

$$r_0 = \left(1.46 C_n^2 k^2 L\right)^{-3/5}, \tag{1.80}$$

for a horizontal link

The Fried parameter is vital in the performance of the communication system. Physically it represents the spatial extent over which the phase of a propagating optical beam will remain the same. The Fried parameter decreases with strong turbulence and increases with weak turbulence and this is true since turbulence affects the phase of the beam. This suggests that turbulent eddies or Fried cells will affect the "Seeing" of the beam that is received. From Eq 1.80 we see that the Fried parameter r_0 is optical turbulence C_n^2 and wavelength λ dependent. The Fried parameter will increase at mid-IR wavelengths as compared to visible wavelengths according to

$$r_0 \propto \lambda^{-\frac{6}{5}}. \tag{1.81}$$

The Fried parameter will increase during night-time conditions and decrease during day-time conditions.

1.5.3 Scintillation

A laser beam propagating through the atmosphere will be altered by refractive-index inhomogeneities caused by small eddies in the atmosphere. At the receiver plane, random intensity distributions are received which are random both in space and time [32]. The irradiance fluctuations over the receiver lens resemble that of a distant star observed from outer space. The scintillation index used to characterize the strength of scintillation is given by,

$$\sigma_I^2 = \frac{\langle I^2 \rangle - \langle I \rangle^2}{\langle I \rangle^2}. \tag{1.82}$$

Where $\langle I \rangle$ and $\langle I^2 \rangle$ are the first and second moments respectively of an ensemble of intensities detected by the point detector after propagating a distance L. Two theories have be formulated in the past: weak fluctuation theory and strong fluctuation theory. One way of differentiating the theories is to use the Rytov variance. It is customary to discriminate both cases for a given propagation problem by determining the value of the Rytov variance. The weak turbulence case is when $\sigma_R^2 < 1$ and the strong turbulence case is when $\sigma_R^2 > 1$ [33; 34]. Scintillation effects cause a loss in the signal to

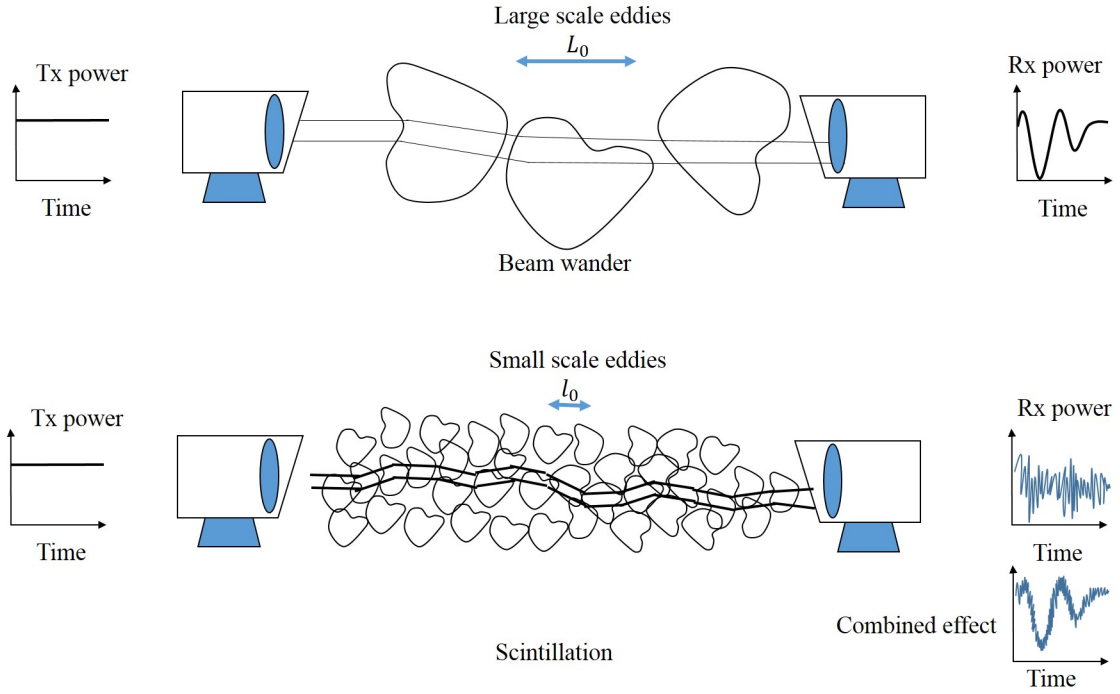


FIGURE 1.16: small eddies affecting the beam as it is propagated through the atmosphere.

noise ratio (SNR) (the measure of how much of the received information is useful) and also introduce signal fades [20; 35]. Figure 1.16 shows that the small eddies cause power fluctuations at the reciever plane together with perturbations introduced by beam wander. One of the objectives in this project is to calculate the value of the atmospheric strength and this is done by relating the Rytov variance to the scintillation index. The scintillation index in terms of the log-amplitude variance σ_x^2 is given by [30]

$$\sigma_I^2 \approx 4\sigma_x^2, \qquad \sigma_x^2 << 1 \tag{1.83}$$

The relationship between the Rytov variance and the scintillation index is given by

$$\sigma_I^2 = \exp\left[\sigma_R^2\right] - 1. \tag{1.84}$$

The turbulence in this study is assumed to be weak and this asserts that $\sigma_R^2 << 1$ and therefore Eq 1.84 will be reduced to

$$\sigma_I^2 \approx \sigma_R^2. \tag{1.85}$$

Therefore for plane waves (or waves with a flat wave-front) the scintillation index in weak turbulence is expressed as

$$\sigma_I^2 = \sigma_R^2 = 1.23 C_n^2 k^{\frac{7}{6}} L^{\frac{11}{6}}, \tag{1.86}$$

and for spherical waves (or waves with a curved wave-front) the scintillation index in weak turbulence is expressed as

$$\sigma_I^2 = 0.4\sigma_R^2 = 0.5C_n^2 k^{\frac{7}{6}} L^{\frac{11}{6}}. \tag{1.87}$$

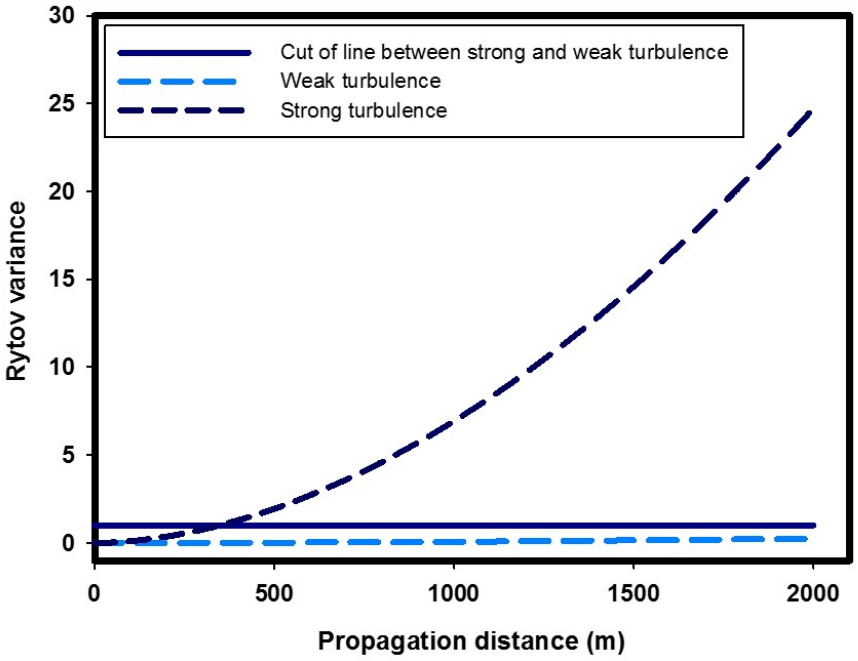


FIGURE 1.17: Simulation of the Rytov variance over a propagation distance for strong and weak turbulent conditions.

Figure 1.17 is a plot of the Rytov variance as a function of the propagation distance for strong and weak conditions. The solid line is the cut-off between strong ($\sigma_R^2 > 1$) and weak ($\sigma_R^2 < 1$) condition with the Rytov variance as our criterion. From this plot we see that Eqs 1.86 and 1.87 are only valid for propagation distances less than 400 m for strong turbulence conditions. For weak turbulent conditions both equations can be used to find the Rytov variance for distances up to 1 km. From Eq 1.86 and Eq 1.87 we see that the wavenumber k will only decrease if you have a laser with a longer wavelength. Hence the longer the wavelength, the smaller the Rytov variance. Therefore longer wavelengths are less affected by optical turbulence as compared to shorter wavelengths.

1.6 Optical turbulence modelling

Different models have been developed over the years to predict the optical turbulence parameter C_n^2. These models depend on meteorological data and they can predict with good accuracy the strength of optical turbulence for a laser beam that propagates over a turbulent atmosphere. When a laser beam is propagated in space the effects that can be experienced are phase front distortions, power losses

and temporal and spatial distortion at the detection plane but these are highly dependent on the local weather conditions [36; 37]. Many authors have tried to predict the behaviour of the refractive-index structure parameter, and various models have been proposed. However, it should be noted that most of these models are based on fitting experimental data conducted at specific locations, which makes it difficult to generalization. Three models where used to predict the optical turbulence parameter C_n^2. We used the weather data obtained from the South African Weather Services as inputs into these models. The PAMELA, Hufnagel-Valley and polynomial regression models will be discussed below.

1.6.1 PAMELA Model

The PAMELA model [38; 39] considers meteorological values, spatial positions (height), the number of days in a year (there are 365 days in a year, if the day of measurement is 10 February 2017 then the input will be 41) and the surface roughness length to model the optical turbulence parameter C_n^2. The PAMELA model gives an estimation of C_n^2 at ground level. Meteorological data and other parameters are substituted into the model to estimate C_n^2

$$C_n^2 = 5.15\varphi_h \left(\frac{1}{\varphi_m - \varsigma}\right)^2 \left(\frac{77.6 \times 10^{-6} P}{T^2}\right)^2 h^{-0.667} \left(\frac{-H}{C_\rho \rho U_\star}\right)^2. \tag{1.88}$$

Where φ_h is the temperature gradient, φ_m is the wind shear estimated from the wind speed Ws, ς is the eddy dissipation rate, H is the heat flux, C_ρ is the specific heat, ρ is the mass density, and $U_\star$ is the friction velocity. In the model itself there are many calculations that need to be performed in order to obtain inputs for the model. The type of terrain where your communication link is situated can adversely affect the value of the optical turbulence parameter. The link was located in an area that is made up of a mixture of natural and man-made features. We find trees, soil and high buildings which also radiate gases and heat which will influence the optical turbulence parameter. In the PAMELA model these factors are taken into account by what we call the roughness length z_r. From the roughness length we calculate the Obukhov bouyancy length scale L given by

$$L = \left[\left(0.004349P + 0.003724P^3\right) z_r^{-\left(05034 - 0.231|P| + 0.0325P^2\right)}\right]^{-1}, \tag{1.89}$$

with the Pasquill stability category P

$$P = \frac{-\left(4 - c_w + c_r\right)}{2}, \tag{1.90}$$

where $c_w = \min\left[Ws/2, 4\right]$ is the wind speed class and the radiation class $c_r = \frac{R}{300}$ is related to the solar irradiance R. The mass density for humid air ρ is given by

$$\rho = \frac{0.0347568 + 6.1078 \times 10^{\frac{7.5(T-273.15)}{(T-273.15)+237.3}}}{8.314\left(T - 273.15\right)}. \tag{1.91}$$

The friction velocity is related to the height above ground h, roughness length z_r and the wind speed Ws by

$$U_* = \frac{0.4Ws}{\log_e\left(\frac{h}{z_r}\right)}. \tag{1.92}$$

The temperature gradient along the propagation distance L $\varphi_h = (1 - 15\varsigma)^{-\frac{1}{4}}$ and the wind shear $\varphi_m = 0.74\,(1 - 9\varsigma)^{\frac{1}{2}}$ with the buoyancy parameter $\varsigma = \frac{z_r}{L}$. With all these parameter calculated we are able to predict the optical turbulence strength value, however the computation time is long.
The PAMELA model is the only model we have used that takes into account atmospheric pressure in order to understand the variations near the ground throughout the day in different weather conditions. The predicted atmospheric pressure over the location of the communication link was relatively constant, even throughout different weather conditions. It will be noted that pressure has a relatively small effect on the value of the optical turbulence parameter C_n^2. Literature has also shown that the contribution of pressure in the modelling of C_n^2 is very small $\approx 3.23 \times 10^{-9}\%$ [39; 40; 41; 42]. A plot of the optical turbulence parameter as a function of time was made based on meteorological data from the South African weather service.

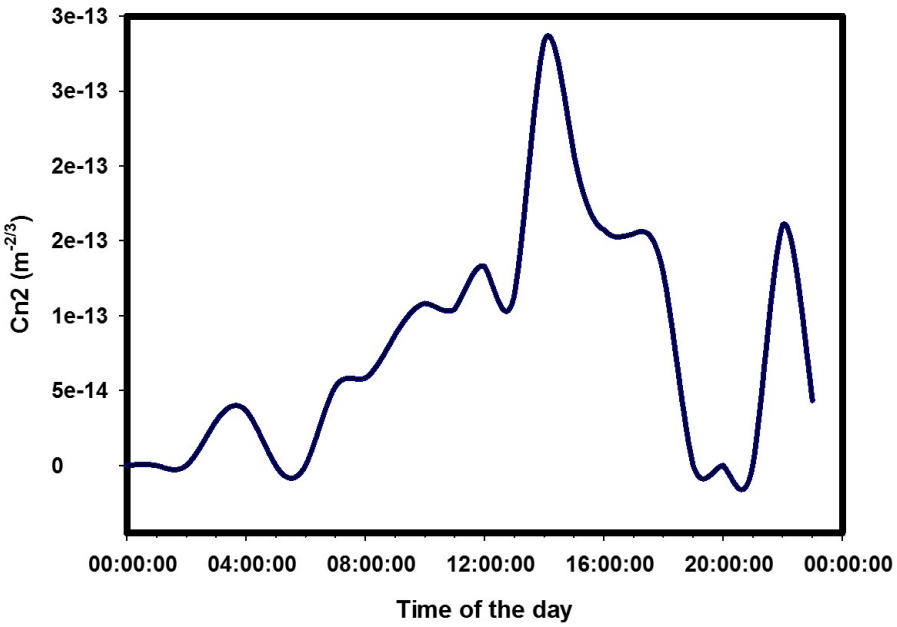


FIGURE 1.18: Calculated optical turbulence parameter versus time of day based on meteorological data for 1 November 2017.

1.6.2 Hufnagel-Valley model

The Hufnagel-Valley (HV) model is used mainly for non-horizontal communication purposes where it predicts the C_n^2 value for night-time and day-time conditions [43; 44]. The model allows variations

in the height above ground (h) and wind speed Ws.

The **Daytime HV model** is given by

$$C_n^2(h) = A\exp\left(\frac{-h}{100}\right) + 5.94\times10^{-53}\left(\frac{Ws}{27}\right)^2 h^{10}\exp\left(\frac{-h}{1000}\right) + 2.7\times10^{-16}\exp\left(\frac{-h}{1500}\right), \quad (1.93)$$

where A is the optical turbulence strength value C_n^2 at ground level (i.e $A = C_n^2$).

The **Night time HV model** is given by

$$C_n^2(h) = 1.9\times10^{-15}\exp\left(\frac{-h}{100}\right) + 8.16\times10^{-54}h^{10}\exp\left(\frac{-h}{1000}\right) + 3.02\times10^{-17}\exp\left(\frac{-h}{1500}\right). \quad (1.94)$$

The predicted C_n^2 strongly depends on the height above ground, h, and is less dependent on wind speed Ws for day-time conditions. During night time conditions it only depends on the heigh h. Therefore, this model predicts a constant value for C_n^2 at a given height. Even though this model only predicts a constant value of C_n^2 for horizontal communication links, for the purpose of this study the constant value at the height of the communication link provides a reference for the optical turbulence parameter. A plot of the predicted C_n^2 values as a function of time of the day was made based on meteorological data.

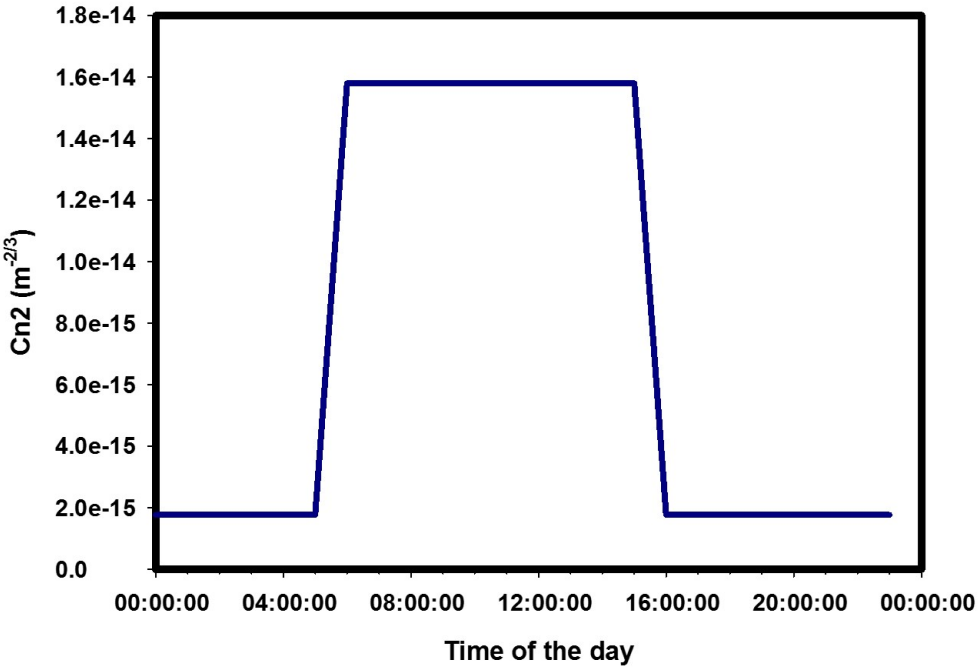


FIGURE 1.19: Predicted optical turbulence parameter versus time of the day based on meteorological data for 1 November 2017 using the HV model.

1.6.3 Polynomial regression model

The Polynomial Regression (PR) model was developed to predict the best estimation of C_n^2 according to the macroscale meteorological data. The PR model is given by

$$C_n^2 = 3.8 \times 10^{-14} W_{th} + 2 \times 10^{-15} T - 2.8 \times 10^{-15} RH + 2.9 \times 10^{-17} RH^2 \\ - 1.1 \times 10^{-19} RH^3 - 2.5 \times 10^{-15} Ws + 1.2 \times 10^{-15} Ws^2 - 8.5 \times 10^{-17} Ws^3 - 5.5 \times 10^{-13}, \tag{1.95}$$

where W_{th} denotes the temporal hour weighting given in the table below, T is the temperature measured in K, RH is the relative humidity measured as percentages and Ws is the wind speed measured in m/s. Temporal hour is $1/12$ of the time between sunset and sunrise. This way of telling the time of the day is like a sunclock. It is a way to provide a normalization between winter and summer times since in summer the time is longer than in winter. Half a day after sunrise would be 6 temporal hours both in winter and summer. In any day of the year sunrise is chosen to be $th = 00:00$, noon $th = 06:00$ and at sunset $th = 12:00$. This model only takes into account temperature, humidity and wind speed and ignores the effects of solar radiation and aerosol loading in the atmosphere. In this work we have chosen to ignore the influence of aerosols and solar radiation to simplify the predictions. If we took into account the effect of aerosols and solar radiation the improved PR model

temporal hour interval	W_{th}	Temporal hour interval	W_{th}
until -4	0.11	5 to 6	1.00
-4 to -3	0.11	6 to 7	0.90
-3 to -2	0.07	7 to 8	0.80
-2 to -1	0.08	8 to 9	0.59
-1 to 0	0.06	9 to 10	0.32
Sunrise 0 to 1	0.05	10 to 11	0.22
1 to 2	0.10	Sunset 11 to 12	0.10
2 to 3	0.51	12 to 13	0.08
3 to 4	0.75	over 13	0.13
4 to 5	0.95		

TABLE 1.1: Table showing the temporal interval with its corresponding hour weighting

given by Sadot and Kopeika [45] would be

$$C_n^2 = 5.9 \times 10^{-15} + 1.6 \times 10^{-15}T - 3.7 \times 10^{-15}RH + 6.7 \times 10^{-17}RH^2 - 3.9 \times 10^{-19}RH^3 - 3.7 \times 10^{-15}W + 2.3 \times 10^{-15}Ws^2 - 8.2 \times 10^{-17}Ws^3 + 2.8 \times 10^{-14}SF - 1.8 \times 10^{-14}TCSA + 1.4 \times 10^{-14}TCSA^2 - 3.9 \times 10^{-13}. \quad (1.96)$$

Where SF is the solar flux and $TCSA$ is the total cross-section area of the aerosol particles given by Yitzhaky in 1997 [46]

$$TCSA = 9.96 \times 10^{-4}RH - 2.75 \times 10^{-5}RH^2 + 4.86 \times 10^{-17}RH^3 - 4.48 \times 10^{-9}RH^4 + 1.66 \times 10^{-11}RH^5 - 6.26 \times 10^{-3}\log_e RH - 1.37 \times 10^{-5}SF^4 + 7.30 \times 10^{-3}. \quad (1.97)$$

A simulated plot of the optical turbulence parameter as a function of time of the day is given in fig 1.20 in Other variants of the PR model have been proposed and these take into the account the coupling and interaction between wind speed, humidity and temperature. The dynamic range for input parameters into the model is 9 to 35°C for temperature, 14.5% to 92% for humidity and 0 to 10 m/s for wind speed. Out of these presented models, the PR model is by far the best model for predicting optical turbulence in the atmosphere based on the meteorological parameter that can be readily accessed from a local weather station.

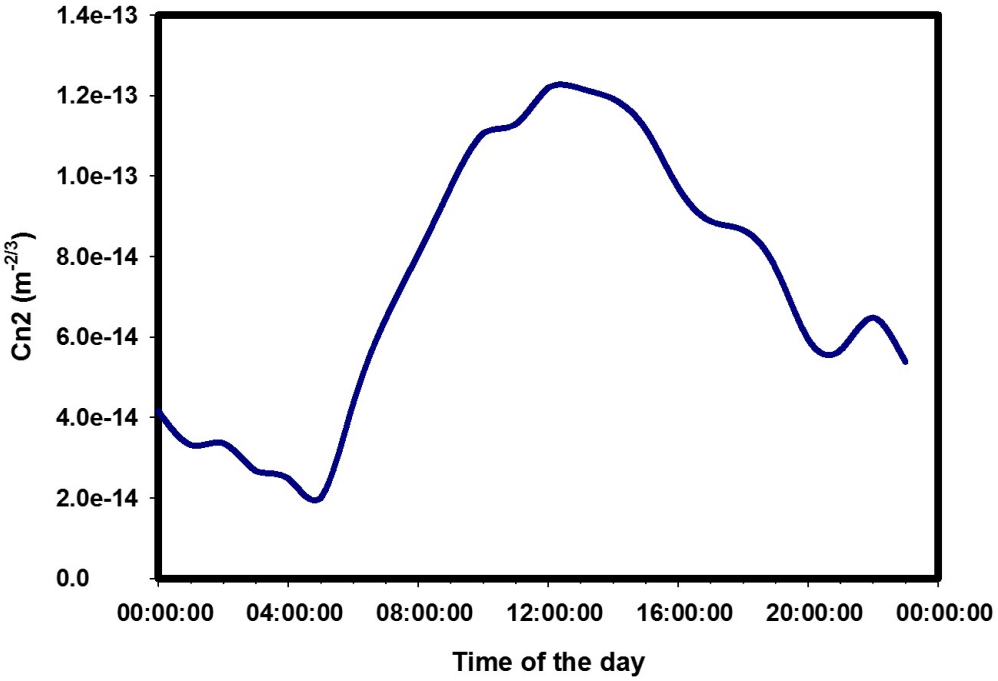


FIGURE 1.20: Calculated optical turbulence parameter versus time of the day based on meteorological data for 1 November 2017 using the PR model.

Chapter 2

Experimental techniques

In the past years the discovery of OAM carrying beams sparked interest in the research community. The use of Spiral Phase Plates (SPP) in generating OAM modes was the most popular until spatial light modulators (SLM) were introduced. The use of SLMs in generating OAM modes is now the preferred method and has the added advantage of generating multiple modes dynamically. In this section we will discuss how SLMs operates, how to calibrate an SLM and how to use SLMs to generate and detect spatial modes.

2.1 Spatial light modulators

Prior to the work of Allen et al [6], in 1990 Soskin et al [47] proposed that a diffraction grating with a fork dislocation can convert a Gaussian mode into a mode possessing a helical wavefront. This was a great stepping stone into creating modes with a twisted wavefront. There are many techniques in generating OAM carrying beams which fall under two categories: passive methods and active methods. One way of generating these beams is to use a SPP as a passive method [48; 49; 50]. This is achieved by passing a Gaussian beam through a SPP which manipulates the dynamic phase of the beam. Mathematically this shift in the phase as it passes through the SPP is given by

$$\delta_d = \frac{2\pi}{\lambda} \left(n_{SPP} - n_0\right) d\left(x, y\right). \tag{2.1}$$

In Eq 2.1, λ is the wavelength of the light propagated through the SPP material of index of refraction n_{SPP} and n_0 is the index of refraction in a vacuum and d is the thickness of the SPP. The use of SPPs has been and is still a successful technique in generating helically phased beams. For these plates to generate a beam with OAM l we require that

$$\delta_d = l\phi, \tag{2.2}$$

where ϕ is the azimuthal angle of the resulting beam. With this assertion and also setting $n_0 = 1$ we obtain the expression for the thickness of the SPP to be given by

$$d(x,y) = \frac{l\lambda}{2\pi\left(n_{SPP}(x,y) - 1\right)}. \tag{2.3}$$

However the challenge with this method is that the thickness is dependant on the wavelength. This has made production of these plates expensive due to the accuracy needed to make the plate a comparable thickness to the wavelength [50].

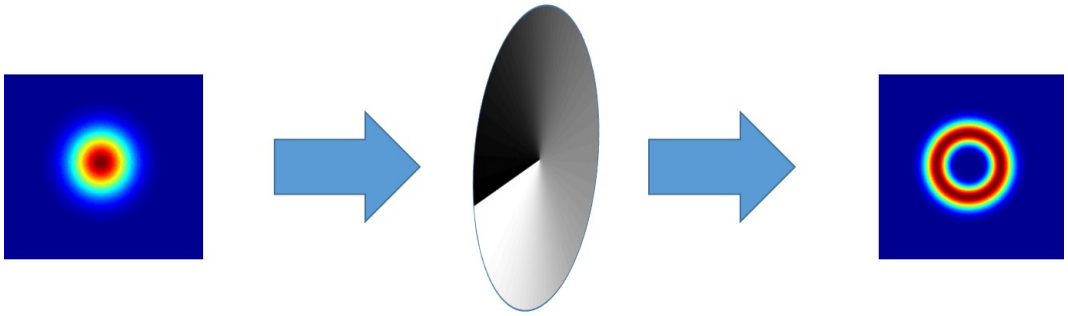


FIGURE 2.1: The use of SPPs for generating OAM carrying beams.

One can use SPPs to generate a beam possessing OAM in a lab setup according to fig 2.1. A beam passes a SPP resulting in a helical wavefront creating a beam possessing OAM. By passing a mode with OAM with a topological charge $l = 1$ into a SPP of charge $l = 1$ the resulting beam will be an OAM mode with charge $l = 2$. When the OAM mode has charge $l = -1$ and the SPP has a charge of $l = -1$ the resulting mode will have charge of $l = 0$. This idea was then extended to active methods in generating OAM carrying beams digitally using holographic principles. The main advantage of digital holograms is that they can be dynamically addressed removing the need to individually manufacture elements. Digital holograms can be implemented with a device called a SLM. Figure 2.2 shows a

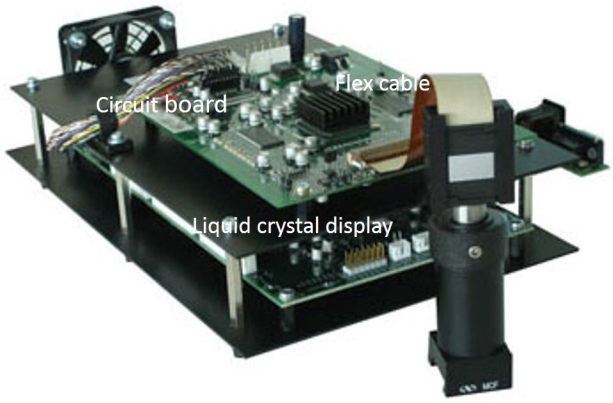


FIGURE 2.2: A HoloEye SLM displaying the green circuit board and the LCD both connected by a flex cable.

HoloEye Pluto phase-only SLM which is made up of two parts: the liquid crystal display (LCD) and the circuit board. The SLM operates like an external screen that is connected to the computer by a HDMI cable. This device modulates the phase of an incident optical field and in some cases the amplitude as well. This device is made up of a phase only LCD with 1920×1080 pixel resolution where each pixel has a pitch of $8\mu m$.

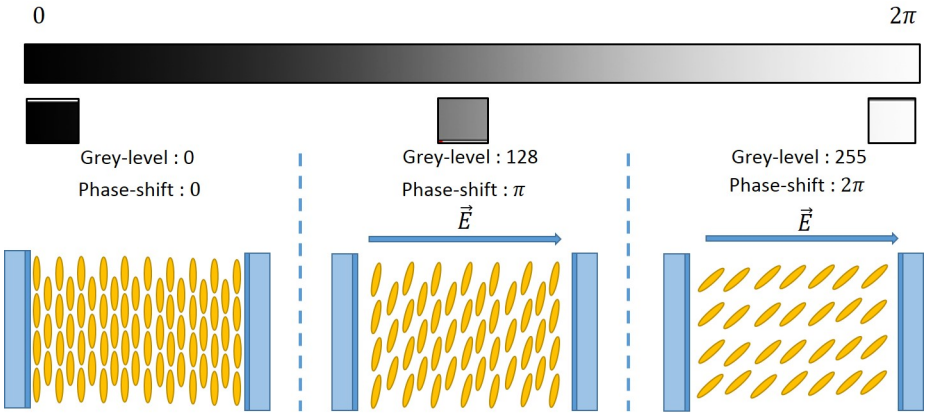


FIGURE 2.3: The LCD crystals respond to the electric field applied across them.

In fig 2.3, the orientation of the liquid crystals (LC) in the LCD of the SLM respond to a change in the applied voltage. When there is no voltage applied to the pixels they do not respond and they remain vertical, resulting in no phase shift induced on the incident beam. When a current is allowed to flow and an electric field is induced, the LCs change orientation in the direction of the applied electric field which results in the changing of the refractive index. A change in the refractive index will result in a phase shift being imparted onto the incident beam. In the LCD of the SLM each LC responds independently to the applied voltage and this means that we can control the orientation of the molecules and therefore it is possible to create any hologram we desire offering endless possibilities in beam shaping.

2.2 Calibration of a mid-IR SLM

Just as SPPs are wavelength dependent, so calibration of the SLM is needed in order for optimal operation of the device at specific wavelengths. It is desired that the SLM has a phase shift of 0 to 2π when modulating light. Modulation is performed by displaying computer generated holograms (CGH) of greyscale images, ranging in grey value of 0 (0 phase shift) to 255 (2π phase shift). A SLM calibrated for a phase shift of 0 to 2π across all 8-bit pixel values for a 2090 nm wavelength will give a different phase shift for a 2403 nm wavelength of which a total phase shift could be either under or higher than 2π. The accuracy of modulating an optical field is important in free space communication as detecting the correct phase pattern will affect the robustness of the system. Meaning if the phase is not correctly modulated the detected modes would be incorrect. The calibration method is based on the double slit interference experiment. Two identical beams (same beam width, amplitude, phase and

polarization) are overlapped with one another creating an interference pattern shown in fig 2.4 (A). The experimental schematic in fig 2.4 (B) was followed in the phase calibration of the SLM. A 2103

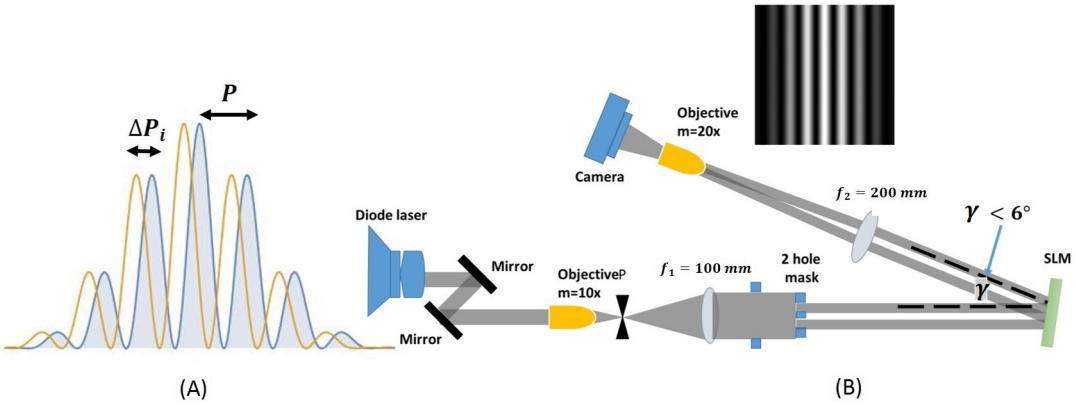


FIGURE 2.4: (A) A simulation of how the phase will shift in response to varying the grey value on one half of the SLM. (B) the experimental setup that was followed in calibrating the SLM.

nm fabry-perot single mode continuous-wave laser diode was used as our light source. The diode was C-mounted and air-cooled by two 5 volts fans mounted at the back of the diode casing to maintain a steady temperature of 20°C. The laser was aligned using two 45° angle mirrors to maintain the same working height for all the optics in the experimental setup. The beam was then expanded 10 times by the microscope objective and collimated by the first lens, $L_1\,(f_1 = 100 \quad mm)$ to produce a flat wave-front illuminating the SLM. A pinhole was used as a spatial filter and placed at the focal length of the objective. An aluminium mask with two circular holes of the same size was used to aperture the beam and allow two identical beams to illuminate the LCD of the SLM. The reflected beams from the SLM where collected by a Fourier lens ($f_2 = 200 \quad mm$) that was placed 200 mm away from the SLM. The angle γ in fig 2.4 (B) is the optimal angle is which the SLM needs to have for maximum efficiency. At the Fourier plane of the Fourier lens a microscopic objective was used to image the Fourier plane on the camera for analysis. Any light field can be expressed in terms of the phase angle (θ) (The phase angle θ is not to be confused with the angle shown in 2.4 (B)), amplitude (A) and its wavelength (λ) while propagating along a path x as

$$U\,(x) = A\cos\left(\frac{2\pi}{\lambda}x - \theta\right). \tag{2.4}$$

The phase angle tells us how far away from the reference point $x = 0$ the peak has shifted. It is this fact that we use to quantify how much the phase shifts when varying the phase of one beam, while keeping the other beam's phase constant. By calculating the relative phase shift given by

$$\delta = \frac{\Delta P}{P}. \tag{2.5}$$

Where ΔP is the shift in the position of the maximum intensity and P is the period we can use these measurements to perform the calibration. In fig 2.4 (A), a simulation was performed in Mathematica were two beams where interfered and a cross section was plotted, showing the phase shift when the phase on one of the beam was changed. The phase of the one beam was held constant while the other was varied, a shift in the interference pattern will be seen and by calculating the shift we can find the total phase shift. HoloEye provided calibration software called Phase-Cam. Phase-Cam is an automated programme that can simultaneously vary the grey scale hologram displayed on the SLM and monitor the location of the maximum of the interference pattern as it shifts across the camera. Phase-Cam is efficient and saves time when measuring the maximum phase shift of the SLM when using a compatible camera but the camera we used to detect mid-IR light was not compatible. Hence we were required to manually vary the grey scale hologram and track the maximum profile in the interference pattern. Measurements of the phase shift were manually calculated according to Eq 2.5. The steps are summarised below:

- Step one: Construct the setup according to Fig 2.4(B).
- Step two: Run/ open the HoloEye application software and display a horizontally divided hologram with grey values.
- Step three: Use a camera (Pyro Cam III) to take images while grey scale is varied on one half of the SLM.
- Step four: Use Matlab to locate and trace the movement of the maximum when the grey value is varied and to extract the period between the fringes (by measuring the pixel distance between two maximum).
- Step five: Use the HoloEye calibration Microsoft Excel file to calculate the new gamma file.

A gamma file is a file which is loaded into a SLM and instruct the SLM to modulate the phase optimally. The HoloEye calibration excel file generates the gamma file from phase shift measurements obtained according to Eq 2.5, by varying the grey values from 0 to 2π. In Fig 2.5(B),(D) the SLM was over filled with an expanded beam as shown. This ensures that the whole surface of the SLM screen was utilized. The SLM screen was divided into two halfs by displaying a hologram of different phase depths as show in fig 2.5(B) and the corresponding profile shown in fig 2.5 (E). Centralizing the two beams onto the SLM screen was important and this is shown in fig 2.5 (C) and (D). A gamma curve for a 2090 nm wavelegth was loaded as a starting modulation curve. Then one half of the SLM was varied from 0 to 255 grey scales in steps of 20 and by using the PyroCam the intensity profiles were recorded.

Each image was saved as an ascii file from the PyroCam viewing software and loaded into Matlab. The image was then converted into an RGB image. Cross sections of all recorded profiles were then taken and we recovered the movement of the maximum of the interference pattern when the grey scale

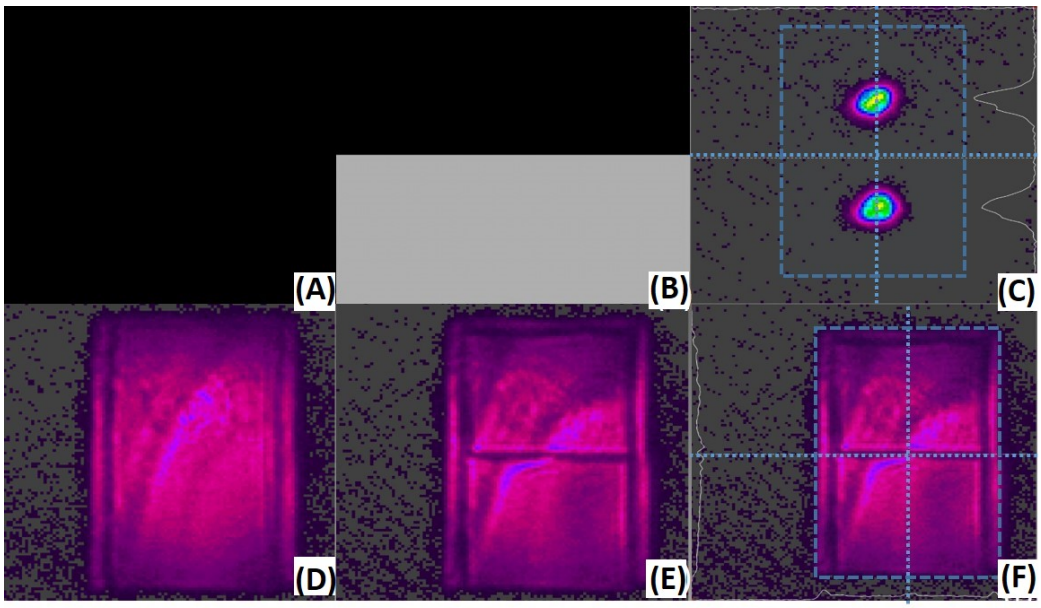


FIGURE 2.5: Blank hologram (a) and its correspond profile (d). Hologram with different phase depth (b) and its correspond intensity profile (e). The intensity profiles of the aperture beam with two beams (c) and without aperture (f).

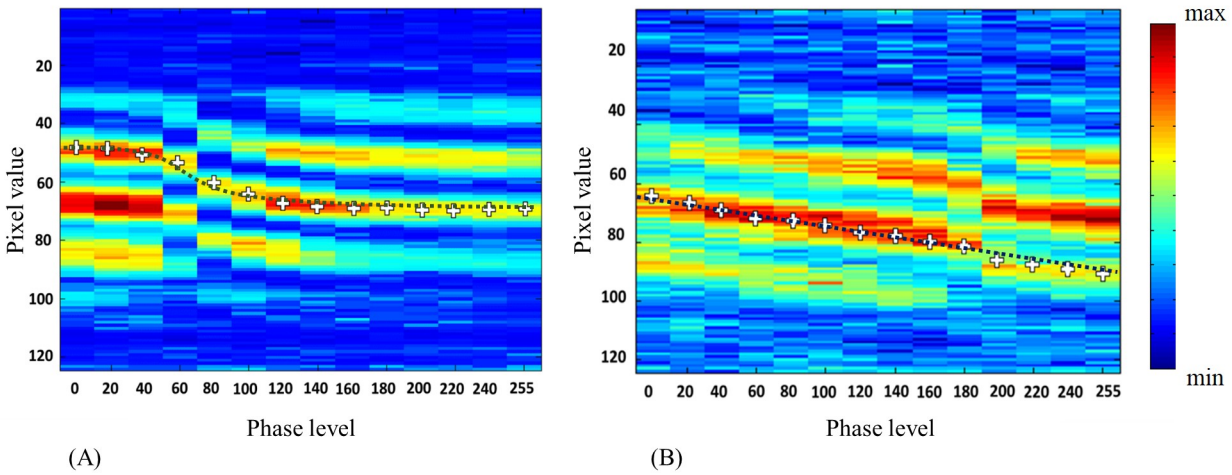


FIGURE 2.6: This picture shows interference fringes as we vary the grey value on one half of the SLM. (A) shows the movement of the local maximum in intensity as we change the grey value before calibration and (B) shows the movements after calibration.

was varied. The location of the maximum in the interference pattern phase shift was then traced out in Matlab as shown in fig 2.6 by the white crosshairs. The phase level can be varied in smaller steps to have more accurate results. However, one can also take measurements in steps of 20 and interpolate and predict the pixel number of the maxima for a given phase value. We employed the Hermite interpolating technique which approximates a polynomial that best fits a data set with its derivative providing the best fit to the data. Once this was done, a new gamma file with a corrected 2π phase map for the 2 micrometer laser was created and tested.

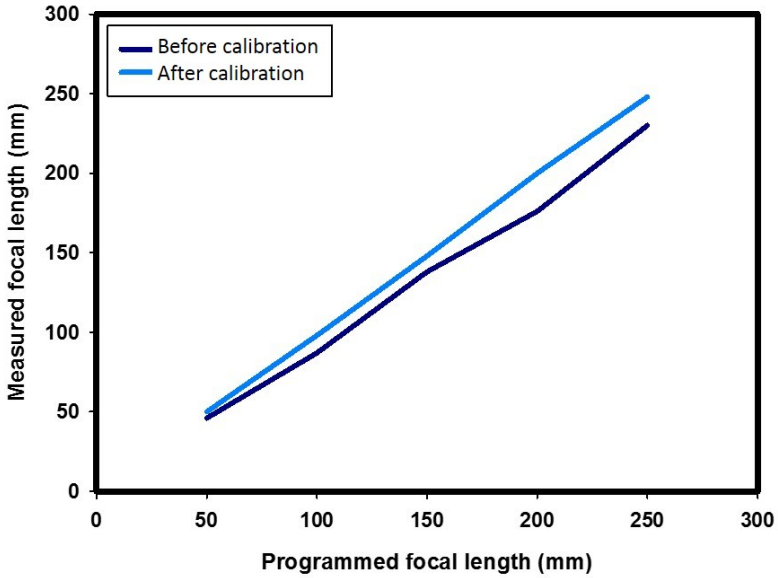


FIGURE 2.7: Plot of the measured focal length after the plane of the SLM versus programmed focal length.

With the calibration now performed, we displayed a lens hologram which mimics the properties of a real lens. The effect of the hologram will focus the beam at the programmed focal length. For a correctly calibrated SLM the beam gshould focus at the encoded focal length. Figure 2.7 shows a plot of measured focal length versus the programmed focal length. A good correlation was observed between theoretical and experimental results after calibration and slight disagreements with theory before calibration. We calculated the correlation between expected values and measured values. We found that a 0.9978 correlation after calibration and a 0.6645 correlation before calibration which indicated that the SLM was correctly calibrated.

2.3 Generation of spatial modes

We wish to begin with an optical field U_0 that has an amplitude A_0 and a phase ϕ_0 and transform it into a new mode say U_1. This optical field U_0 is given by:

$$U_0 = A_0 \exp(i\phi_0), \tag{2.6}$$

and the transformation of U_0 to U_0

$$U_1 = A_1 \exp(i\phi_1), \tag{2.7}$$

can be mathematically represented by

$$U_1 = T \times U_0. \tag{2.8}$$

Where T is called the transmission function which transforms U_0 into U_1 given by

$$T = \frac{A_1}{A_0} \exp[i(\phi_1 - \phi_0)]. \tag{2.9}$$

From this we see that in order to create spatial modes we need to have phase and amplitude modulation. We only have a phase-only SLM so our required transmission function should be a function of the phase. This function is given by

$$T = \exp(i\Phi_{slm}) \tag{2.10}$$

In order to create a spatial mode of light we can employ a hologram with a transmission function T of amplitude 1 given by Eq 2.10 employed to take more light towards the zeroth order or to take more light toward the higher order [51] and by so doing we can create spatial modes having amplitude and phase information. The holograms displayed on the SLM with varying phase depths act as a diffraction tool which creates multiple orders as shown in fig 2.8 (A). From Fourier optics, the transmission function can be mathematically describes as

$$T(x,y) = \sum T_m \exp(im(G \cdot r)), \tag{2.11}$$

where

$$G = \frac{2\pi}{\sigma}(\cos(\theta)\hat{x} + \sin(\theta)\hat{y}) \tag{2.12}$$

gives the grating wavevector which is periodic along the direction θ with a period given by σ. T_m represents the amplitude of the beam that is diffracted into the order m. $\hat{x}$ and $\hat{y}$ are unit vectors along the x and y direction and r and θ are points in cylindrical co-ordinates. We programme these coordinates on the SLM. This amplitude is given by:

$$T_m = \frac{1}{A}\int\int_{\sigma} T(x,y) \exp(-im(G \cdot r))\, dr, \tag{2.13}$$

where $A = \int \int_{\sigma} dr$ is the area over a single period in a grating. By introducing modulation in this periodic pattern, it is possible to have phase and amplitude control in the diffracted order as shown in fig 2.8 (B).

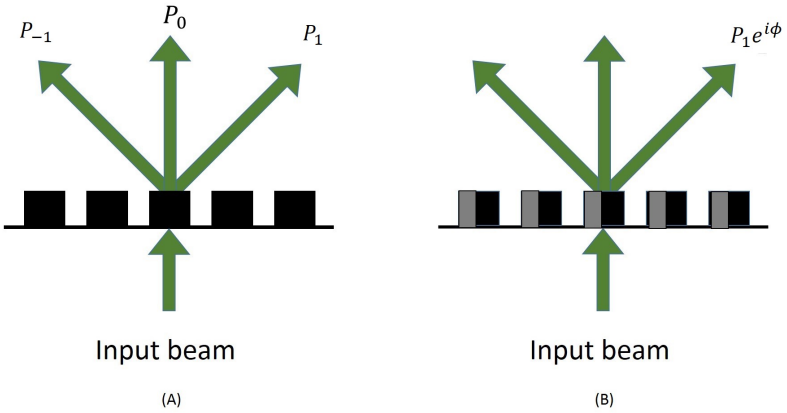


FIGURE 2.8: (A) The effect of applying a grating on a beam will diffract light into its nth orders and (B) by having different shades of grey we can control light and give it the phase modulation we require.

In this project we worked with phase only SLMs and the holograms displayed onto the SLM LCD have a transmission function of the form

$$T(x,y) = \exp(i\Psi(x,y)) \tag{2.14}$$

where Ψ is the phase at position (x,y). However we need to create a beam that has

$$U(x,y) = A(x,y)\exp(i\phi(x,y)), \tag{2.15}$$

where A and ϕ are the usual amplitude and phase of the desired mode. Arrizon [52] proposed the assumption of a periodic function $\Phi(\phi)$ which gives information about the desired mode, where the modulation function $f(A)$ gives information about the amplitude. He suggested that for a phase-only SLM :

$$\Psi = \Phi(\phi) f(A). \tag{2.16}$$

There are many types of periodic function $\Phi(\phi)$ which one can assume but in short we will discuss the blazed grating and the sinusoidal grating. The Blazed grating is used to create the vortex modes (modes that have only an azimuthal dependence) and the sinusoidal grating is used to create the LG modes (These modes have an azimuthal and radial dependence).

The **blazed grating** is defined to have the function

$$\Phi = (G \cdot r + \phi) \, mod 2\pi - \pi \tag{2.17}$$

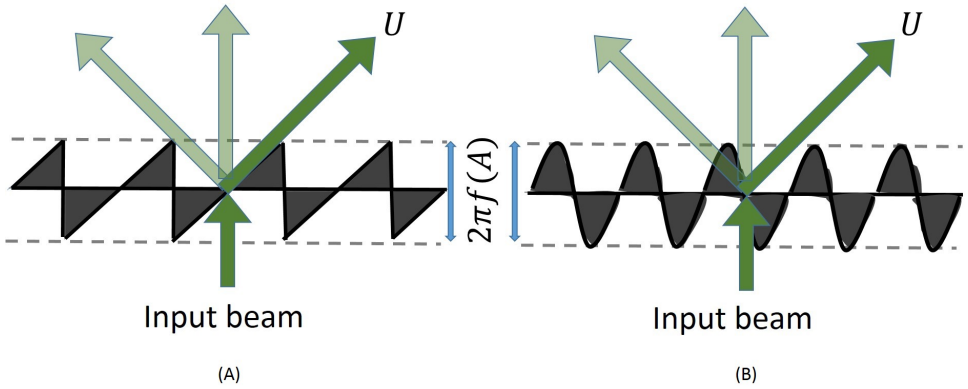


FIGURE 2.9: Programmed SLM holograms displaying (A) blazed and (B) sinusoidal gratings.

with $\Phi \in [-\pi, \pi]$ chosen to be symmetric about zero to remove additional phase modulation [53]. In order to find the mth order transmission function we use Eq 2.13 which results in

$$T_m = \frac{1}{A}\int\int_{\sigma} T(x,y)\exp\left(-im\left(G\cdot r\right)\right)dr = \int_{-pi}^{pi}\exp\left(if\left(A\right)\Phi\right)\exp\left(-im\Phi\right)d\Phi = \sin c\left(m - f\left(A\right)\right) \tag{2.18}$$

To find $f(A)$ we determine the inverse of T_1

$$T_1\left(A\right) = \sin\left(1 - f\left(A\right)\right) = A \tag{2.19}$$

In fig 2.9(A) the effect of displaying a blazed grating hologram is shown, which is known to give maximum diffraction efficiency.

The **Sinusoidal grating** is defined to have the function

$$\Phi = \sin\left(G\cdot r + \phi\right). \tag{2.20}$$

Following the same procedure in finding the transmission function for the blazed grating we get

$$T_m\left(A\right) = J_m\left(f\left(A\right)\right). \tag{2.21}$$

Similarly to find $f(A)$ we can simply find the inverse of T_1

$$T_1\left(A\right) = J_1\left(f\left(A\right)\right) = A. \tag{2.22}$$

Where J_m is the mth Bessel function. The maximum value of A for the sinusoidal case which allows $J_1^{-1}(A)$ (which is the inverse Bessel function) to be a single value is $A = 0.58$, corresponding to the first maximum of $J_1(f(A))$ at $f(A) = 1.8$. Therefore $A = [0, 0.58]$ and $f(A) = [0, 1.8]$, which gives a phase range of $\Psi[-1.8, 1.8]$. This is in contrast to the blazed grating that gives a phase range

of $\Phi \in (-\pi, \pi)$ and a maximum amplitude of $A_{max} = 1$. The effect of displaying a sinusoidal grating is shown in fig 2.9 (B). It was observed that the effects of the different grating on a beam affect the power transmitted into the first order. A blazed grating will diffract more power onto the first order as opposed to the sinusoidal grating. In fig 2.11 was a schematic used to create spatial modes. A SLM is displaying a hologram which will shape the illuminated beam. The input beam will be modulated and the diffraction orders will be observed as shown in fig 2.10. We use lens (lens-1) to separate the diffraction orders at the Fourier plane and then we make use of an aperture to block out unwanted orders and only select the first order which contains the desired mode we want. Then lens (lens-2) images the mode from the plane of the SLM into the camera were the intensity profiles are recorded. Figure 2.12 shows experimentally generated LG modes of various p and l. These modes are used to

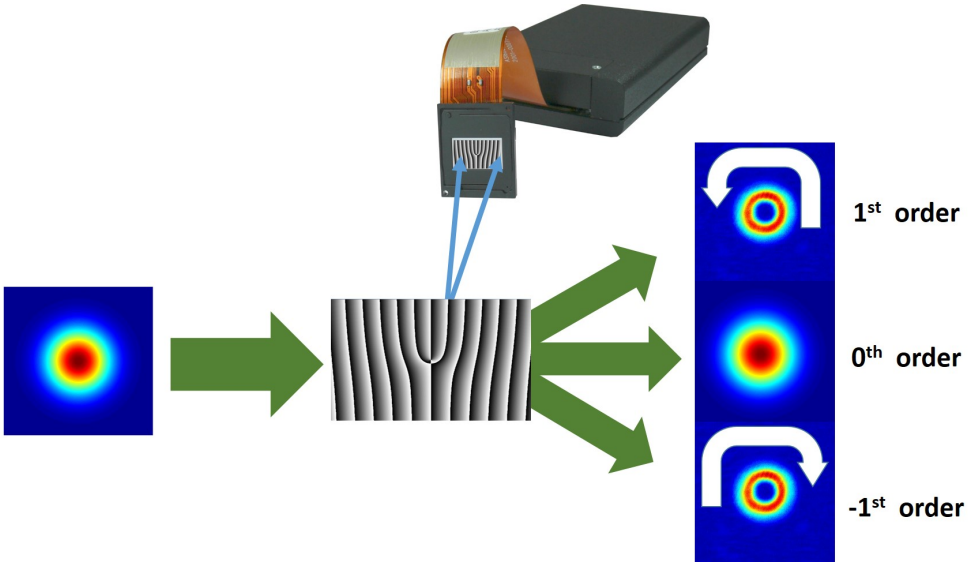


FIGURE 2.10: Creation of spatial modes using digital holograms.

encode information.

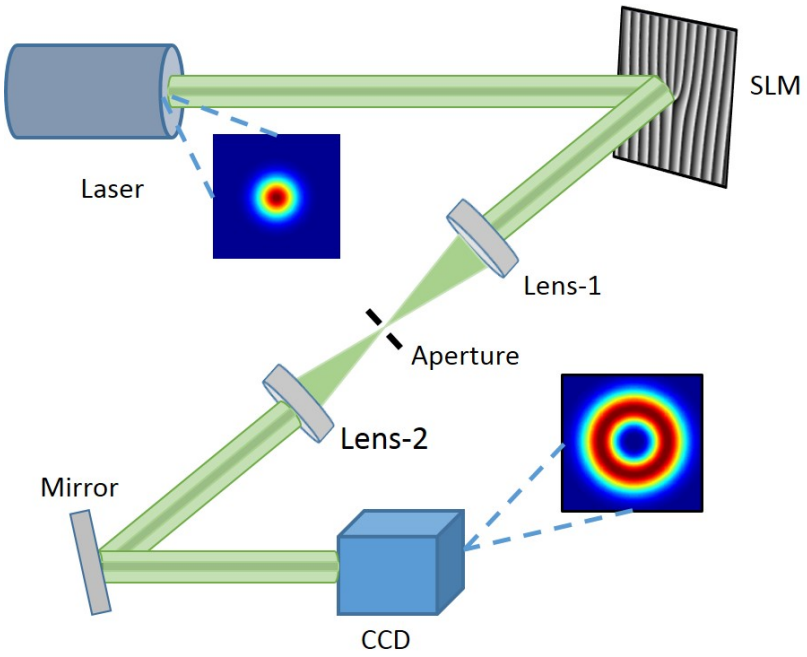


FIGURE 2.11: A simple lab setup that we use to generate structured light. A laser beam illuminates a SLM that is programmed with a hologram that has a transmission function given by Eq 2.14. The lenses (Lens-1 and Lens-2) image the mode that was filtered by the aperture onto the CCD camera.

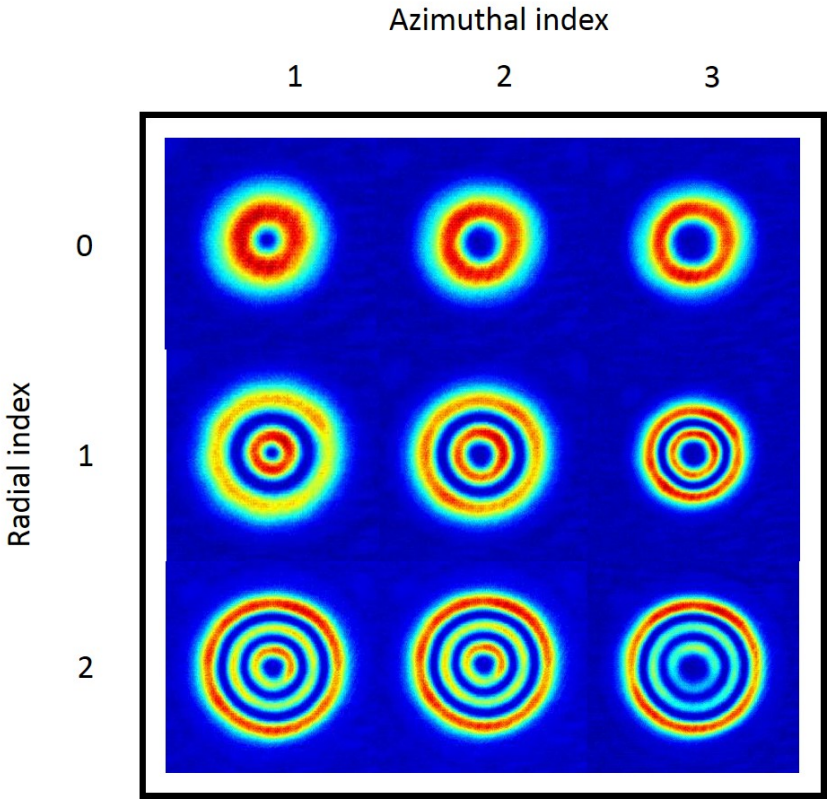


FIGURE 2.12: Experimentally generated LG modes

2.4 Detection of spatial modes

The detection of arbitrary spatial modes of light is achieved by a technique called modal decomposition and it has been known for quite some time. With this technique we can determine the modal content (relative phase and amplitude) of the mode. When the modal content of a specific mode being analysed is known then all the physical properties (phase, beam quality, OAM density, intensity and wavefront) about the optical field can be inferred [54; 55; 56; 57; 58; 59].
The main idea behind this technique depends solely on the fact that spatial modes of light are orthogonal and they span the infinite dimensional Hilbert space. Therefore any complex light field can be decomposed as a superposition of basis functions (e.g either LG or azimuthal modes) [60] each with a weighting that is complex. Mathematically the entire optical field is written as

$$U(x,y) = \sum_{n=1}^{nmax} c_n \psi_n(x,y), \tag{2.23}$$

where n represents the number of modes used to decompose the optical field which can be expanded to infinity since they span the Hilbert space. ψ_n represent a spatial mode which satisfies the orthonormal property according to

$$\langle \psi_n | \psi_m \rangle = \int\int dA \psi_n^* \psi_m = \delta_{nm}. \tag{2.24}$$

with the modal weight or the expansion coefficient is given by given by

$$c_n = \rho_n \exp(i\Delta\phi_n) = \langle \psi_n | U \rangle. \tag{2.25}$$

Where the amplitude of the nth mode is given by ρ_n and the intermodal phase difference is given by $\Delta\phi_n$. The mode amplitude and phase difference $\Delta\phi_n$ are both found experimentally. Determination of the expansion coefficient c_n is the main task of the modal decomposition technique. The intensity and phase distribution of the entire optical field is determined by finding

$$I(x,y) = |U(x,y)|^2, \tag{2.26}$$

and

$$\Phi(x,y) = \arg(U(x,y)). \tag{2.27}$$

In a lab setup as shown in fig 2.15, we perform a modal decomposition on an optical field in question, say $U(x,y)$ by illuminating it onto a SLM where a detecting hologram with transmission function $T(x,y) = \psi_n^*(x,y)$ is displayed, with $*$ denoting the complex conjugate. The first diffraction order after the SLM is given by

$$U_1(x,y) = \psi_1(x,y)\, U(x,y). \tag{2.28}$$

Where ψ_1 represents the hologram of a spatial mode displayed on the SLM.

When a lens is placed one focal length away from the SLM after illumination, the Fourier transform of the field given by Eq 2.28 is obtained,

$$F\left(k_x, k_y\right) = \int\int dA T_m\left(x, y\right) U\left(x, y\right) \exp\left(ik_x + ik_y\right). \tag{2.29}$$

If we set $k_x = k_y = 0$ then we are detecting the on-axis position. In a lab setup (shown in fig 2.15) the detection plane at the Fourier plane (recorded by the CCD camera as shown in fig 2.15) illustrates how one can determine if the mode being investigated is detected or not detected. Here we chose one single pixel corresponding to $k_x = k_y = 0$ as our detection signal. This mathematically corresponds

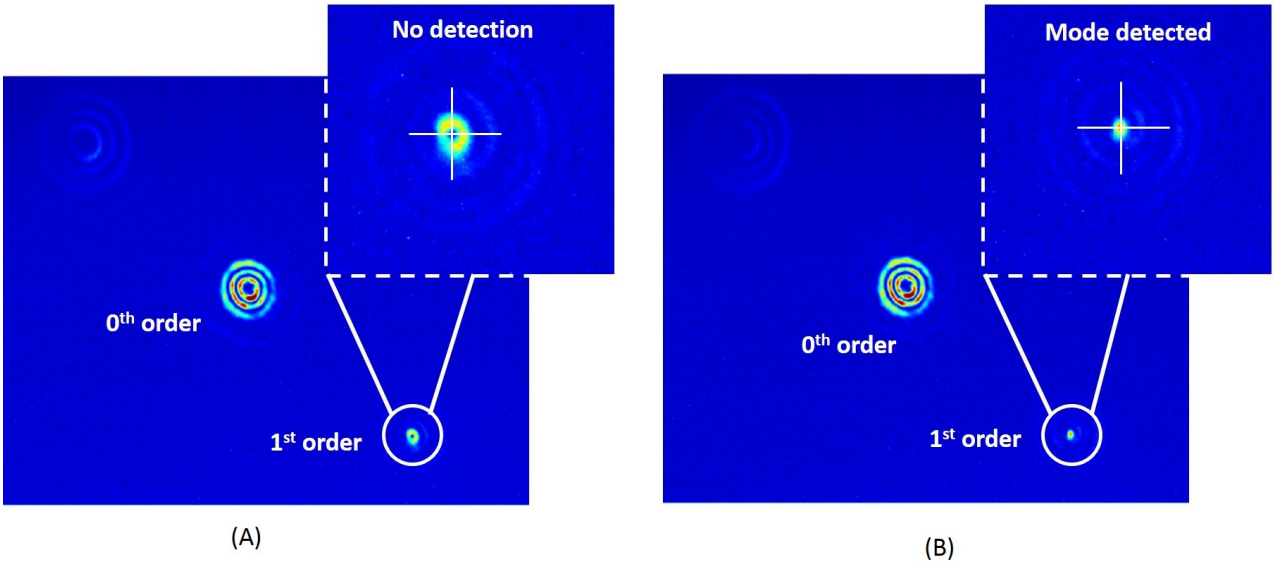


FIGURE 2.13: In a lab setup we detect spatial modes of light at the Fourier plane. (A) shows a case were no detection is made in which a null is seen at the center of the cross-hairs. (B) illustrates that a detection is made as a bright spot is seen at the center of the cross hair.

to the modal weighting,

$$\left|c_n\right|^2 = \left|F\left(0,0\right)\right|^2 = \left|\int\int dA \psi_n\left(x, y\right) U\left(x, y\right)\right|^2 = \left|\langle\psi_n|U\rangle\right|^2. \tag{2.30}$$

Therefore with this technique we can determine the modal content of any optical field that is being received, allowing us to assign information to any mode.

The lab setup we follow to detect spatial modes is shown in fig 2.15. The plane of the first SLM (SLM-1) is imaged into the plane of the second SLM (SLM-2). On the second SLM we display match filters to decompose the incident spatial mode. We use a Fourier lens (Lens-3) to separate the diffraction orders as shown in fig 2.13. When the match filter is the complex conjugate of a mode present in the field of interest an on axis intensity is detected and when the match filter does not "match" a mode in the incident field a null is formed. Figure 2.14 shows the result of decomposing

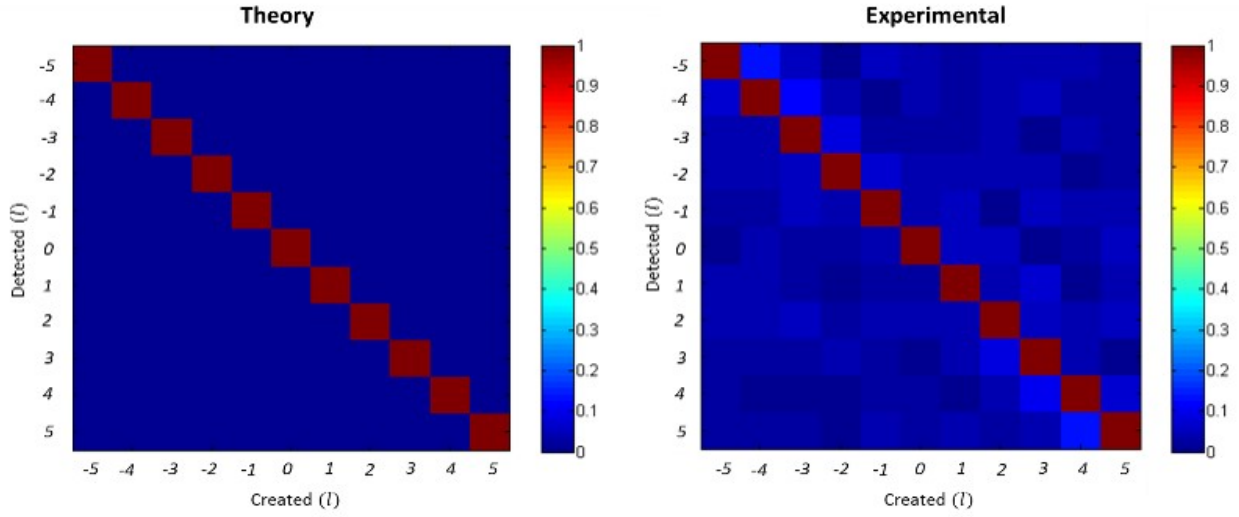


FIGURE 2.14: Decomposition of LG modes by variying the topological charge l and keeping radial index p constant.

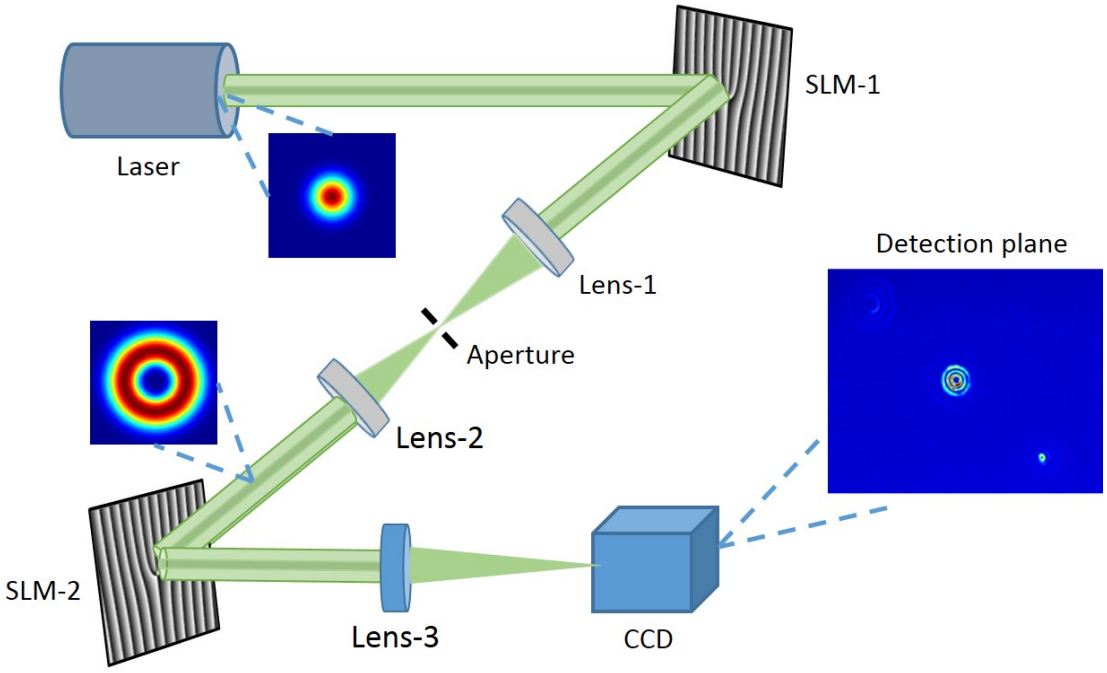


FIGURE 2.15: Modal decomposition setup for detecting spatial modes.

spatial modes with varying l with error of 2 %. The red squares (high intensity) in fig 2.14 is an indication of a detection being made and we see good agreement with theory.

Chapter 3

Link Characterization

In any communication link, a link budget analysis will have to be performed, as this characterizes the link under operating conditions. We will characterise the link by calculating the losses within the system and losses incurred during transmission in the atmosphere. When we send information in free space and by taking into account the losses during transmission, the power must be above the sensitivity of the detector. In this chapter, we will discuss all the attenuation that our optical field is going to experience during propagation in order to quantify the losses to perform a link budget.

3.1 Effects of the atmosphere on the power of a laser beam

Very often, over long distances, a laser beam will suffer power loses as it propagates in the atmosphere. These losses are due to the atmospheric absorption, weather related loses (rain), turbulence (due to beam wander and scintillation) and free space losses (geometric losses). When we calculate a link budget we take into account all the losses experienced by the laser beam from the transmitter to the receiver. Figure 3.1 summarises all the losses that can be incured during propagation of a beam in the atmosphere.

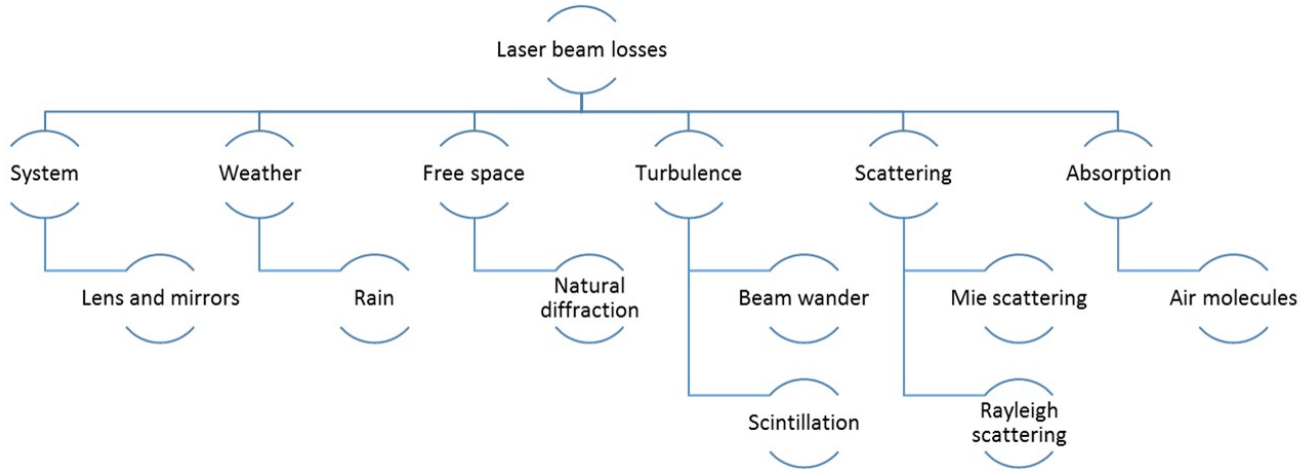


FIGURE 3.1: Losses experienced by the laser beam propagating in the atmosphere.

3.1.1 Absorption and Scattering losses

An optical field propagating in the atmosphere will experience power (energy) losses and will be converted to other forms of energy. Absoption is a wavelength dependent phenomenon. Depending on the type of laser beam propagating in the atmosphere, some or all of the energy contained in the beam will be converted into heat energy. In the atmosphere we find many types of air molecules that contribute to the laser beam's attenuations, these molecules are nitrogen-N_2 (78%), oxygen-O_2 (20%), carbon dioxide-CO_2 (0.04%) plus traces of argon(Ar), methane (CH_4) water vapor (H_2O), nitrous oxide (N_2O) and carbon monoxide (CO). In fig 3.2 the absorption spectrum for various gases found in the atmosphere are plotted as a function of the wavelength of the optical field. Absorption is a measure of the ability of a molecule to absorb the optical fields energy.Transmittance is defined as the ratio between the transmitted optical field in a random medium relative to the field radiating the medium. The transmission T of a optical field is mathematically described

$$T = \exp\left(-\alpha\left(\lambda\right) z\right). \tag{3.1}$$

Where $\alpha\left(\lambda\right)$ is known as the extinction coefficient and z is the propagation distance. In the ultra-violet region the region where the wavelength is below (0.1 to 0.3 μm) the optical field is heavily attenuated by O_2 and O_3 and also small attenuations in the visible region (0.4 to 0.7 μm) are seen. In the IR region most of the light is absorbed by H_2O and CO_2 molecules. We also see that there are transmission windows seen in the mid-IR region around 2.1μm. A MODTRAN (MODerate resolution atmospheric TRANsmission) simulation of the transmittance over a 1 km horizontal path with wavelengths ranging from 0.3μm to 3μm was plotted as shown in 3.3. The MODTRAN is a model developed by the U.S. Air force research lab to simulate how much of the optical field is transmitted over a specified distance assuming clear weather conditions with 23 km visibility. In fig 3.3 we see multiple transmission windows in the IR region.

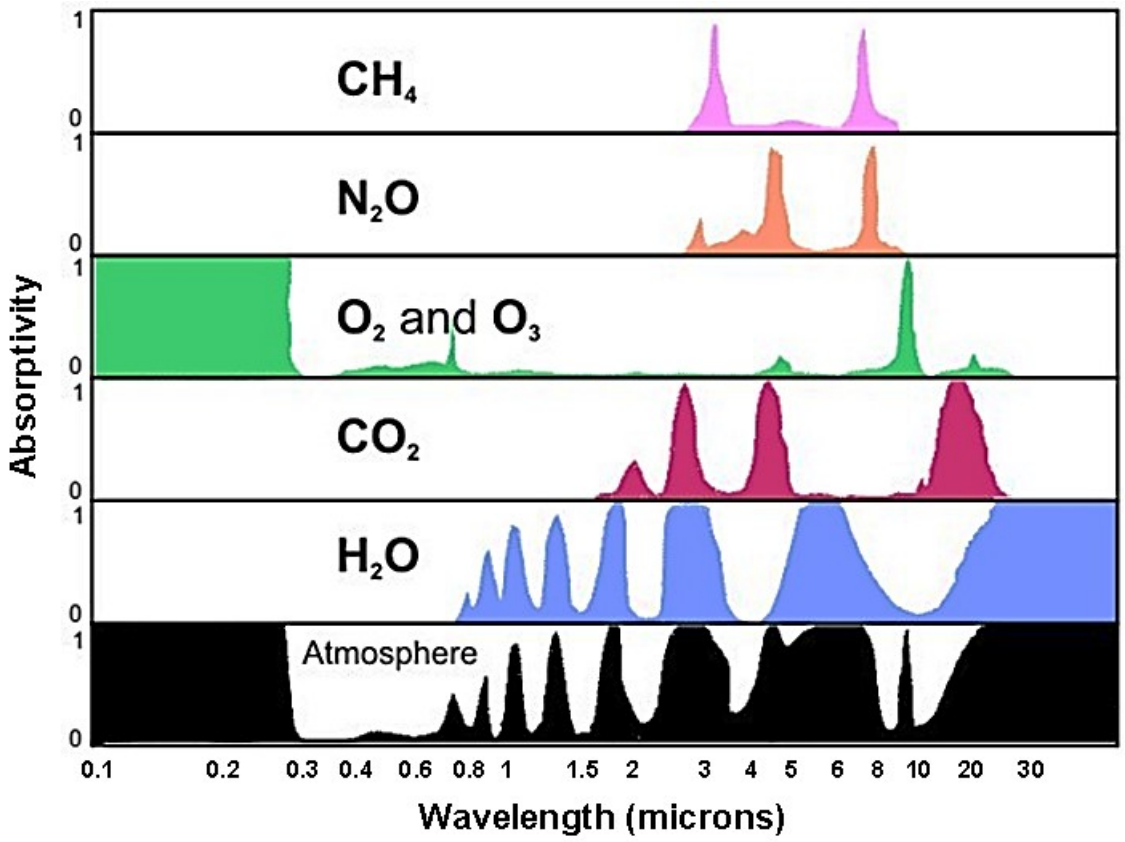


FIGURE 3.2: The atmospheric absorption spectrum by various molecules in the atmosphere [61].

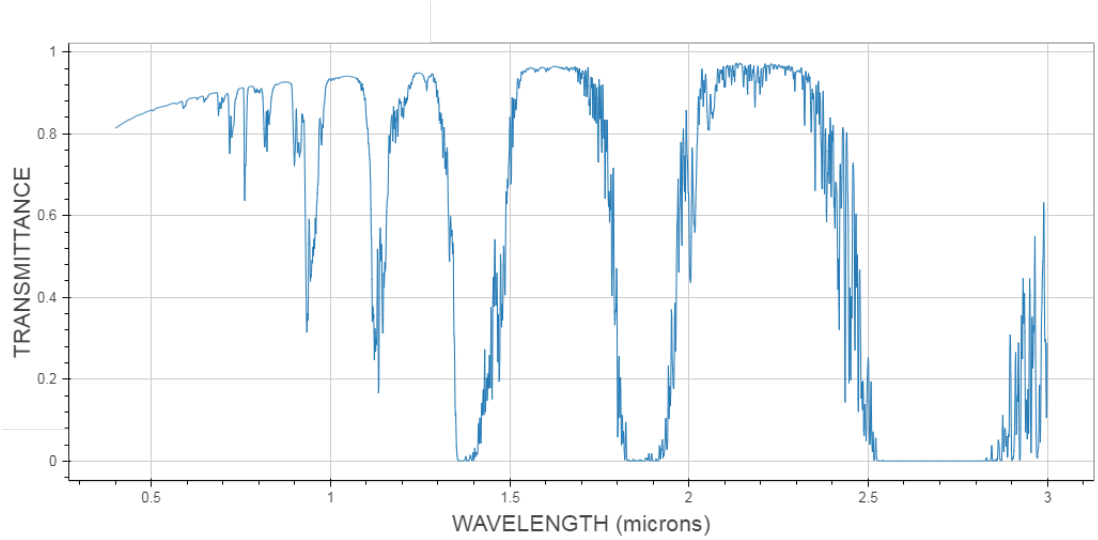


FIGURE 3.3: MODTRAN simulation of the fraction of radiation transmitted in the atmosphere as a function of wavelength.

Optical fields will also experience scattering or reflections or a combination of the two as it propagates in space by small particles. There are two types of scattering processes: Rayleigh scattering

and Mie-scattering. Rayleigh scattering is caused by particles that are small compared to the transmitted wavelength. The Rayleigh scattering follows the spectral dependence of λ^{-4}. This dependence means that for optical fields with longer wavelengths they will experience less scattering as compared to shorter wavelengths. Mie scattering on the other hand is due to particles that are relatively large as compared to the transmitted wavelength. This process has a spectral dependence of λ^{-1}. When calculating the losses due to absorption and scattering the Kruse model can be used. This model takes into account the meteorological visibility parameter V (defined only in km) only to give a rough estimate to the losses. The Kruse model [62] is given by

$$L_{atm}[dB/km] = \frac{17}{V}\left(\frac{0.55}{\lambda}\right)^{q}, \tag{3.2}$$

where q is given by

$$q = \begin{cases} 1.6 & V > 50km \\ 1.3 & 6 < V < 50 \\ 0.585V^{\frac{1}{3}} & V < 6 \end{cases}$$

and λ is the wavelength in nm.

3.1.2 Rain losses

Typical size of rain droplets is around 0.5 mm to 4 mm in diameter which is about 100 to a 100000 times larger than wavelengths used in free space communication links. It was found that losses due to rain is independent of wavelength that is used for communication [63]. The modelling of rain attenuation is mainly done using empirical methods. The model is given by

$$L_{rain}[dB/km] = k_1 R^{k_2}, \tag{3.3}$$

where R is the rain fall rate measured in mm/hr and k_1 and k_2 are constants that depend on the size of the rain drop and the rain temperature. The best constants used in the model are given by

$$L_{rain}[dB/km] = 1.076R^{0.67}. \tag{3.4}$$

The meteorological values obtained from the South African Weather Service also have rain values measured for the location of the communication link. We will use these values to characterise the losses due to rain in our communication link. It is to be noted that the South African weather service define rain rate from 0 to 2.5 mm/h as light rain, 2.5 mm/h to 5 mm/h as moderate rain and anything above 5 mm/h is considered as heavy rain. In order to mitigate the rain losses incurred in a communication link high powered lasers need to be used in order to compensate for the losses. A

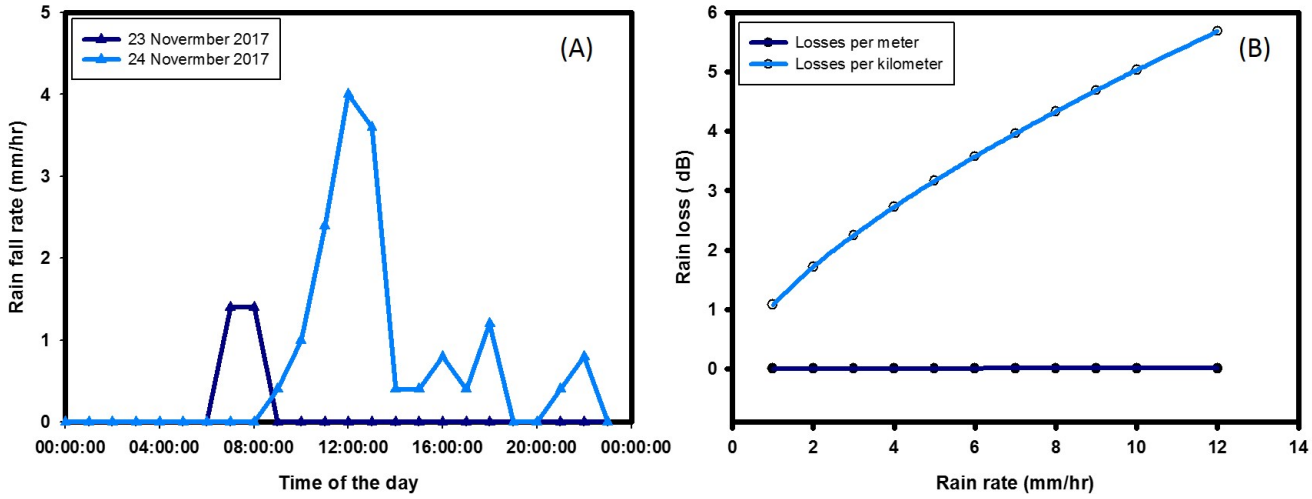


FIGURE 3.4: A numerical simulation of the attenuation due to rain as a function of the rain rate.

simulation of the attenuation versus rain rate over a 1 km link is shown in fig 3.4. This graph shows that for heavy rain days the performance of the communication system will be affected.

3.1.3 Optical turbulence losses

The effects of optical turbulence on a propagating laser beam are beam wander and scintillation effects. From the Rytov's analysis we were able to find a relationship between the Rytov variance and the optical turbulence parameter by Eq 1.70 [25]. In most published articles the optical turbulence at the received signal is attributed to the optical turbulence parameter by merely stating the conditions as weak, moderate or strong without quantifying the signal losses. It has been shown in [64] that the attenuation due to optical turbulence is given by,

$$L_{tur}[dB] = 2\sqrt{23.17 C_n^2 k^{7/6} L^{11/6}}. \tag{3.5}$$

Optical turbulence also introduces losses in the spatial coherence of the transmitted beam. The degree of coherence for a plane wave is given by

$$\gamma = \exp\left[-\left(\frac{|\rho_a - \rho_b|}{\rho_0}\right)^{\frac{5}{3}}\right]. \tag{3.6}$$

Where ρ_0 is the phase coherence radius of the transmitted beam and ρ_a and ρ_b are position vectors between at points a and b . When $|\rho_a - \rho_b| > \rho_0$ the wavefront will lose its spatial coherence. From the measured and calculated optical turbulence parameters C_n^2 the amount of attenuation can be calculated using Eq 3.5. In fig 3.5 a plot of the losses due to optical turbulence as a function of distance for a 532 nm laser propagating under different turbulence conditions is shown. We see from

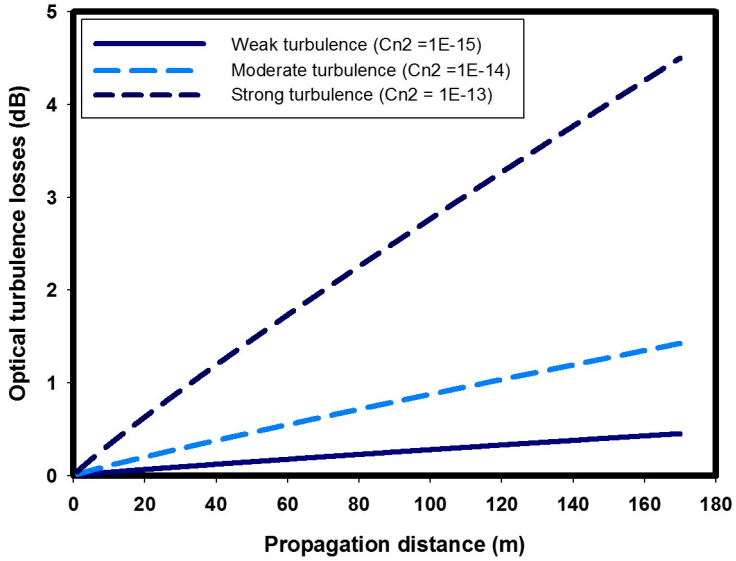


FIGURE 3.5: A plot of the losses due to optical turbulence as a function of distance for a 532 nm laser propagating under different turbulence conditions.

the plot that under strong turbulent conditions losses are very large, this is to be expected since the influence of turbulence alters the phase and size of the beam. In weak conditions the losses are not significant. This means that during night conditions when the optical turbulence is at its minimum the communication system is likely to perform better as opposed to operating during the day.

3.1.4 Geometric losses

Laser beams spread upon propagation. The spreading and thus relative size of the beam on the receiving optics causes geometric attenuation. In all free space communication systems geometric losses contribute more to the losses on the system even in clear weather conditions. Geometric losses can be calculated by [65]:

$$L_{Geo}[dB] = -10\log\left(\frac{D_{Rx}}{D_{Tx}+\theta L}\right)^2. \tag{3.7}$$

Where D_{Rx} is the diameter of the receiver, D_{Tx} is the diameter of the transmitter and θ measured in $mrad$ is the divergence of the transmitted beam. Eq 3.7 relates the geometric losses as a function of the propagation distance, the recieve and transmitter lens diameter and the divergence of the beam. In fig 3.6 (A) we plotted the geometric losses as a function of the link distance for different divergence angles θ. We see from the plot that when we propagate a beam in free space with a large divergence the received power will be small since the losses are significantly large. Therefore when building a communication link the beam divergence should be taken into account. In this project we made sure that our transmitted beam was large enough such that the returning beam is of the same size as the transmitted beam. In fig 3.6 (B) we plotted the geometric losses as a function of the link distance for different receiving apertures. We see from the plot that the bigger the receiving aperture the lower the

geometric losses. In this project we made use of a lens with a diameter of 150 mm which was more than adequate to collect the received beam.

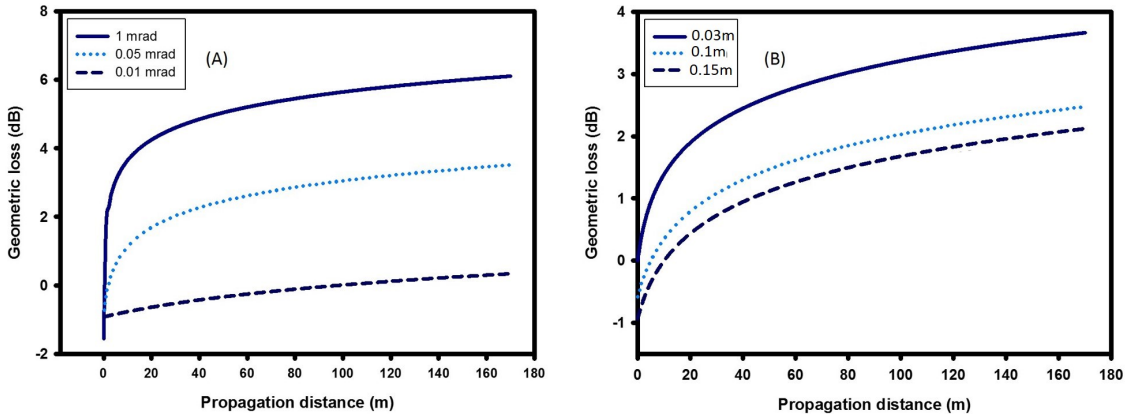


FIGURE 3.6: (A) A plot of the theoretical geometric losses incurred in a link as a function of distance for beams of different divergence. (B) A plot of the theoretical geometric losses incurred in a link as a function of distance for different receiving apertures.

3.2 Link budget analysis

In a communication system we have two types of antenna, a isotropic transmitter which is able to send signals in all directions and a directive transmitter. In a isotropic transmitter shown in fig 3.7(A)

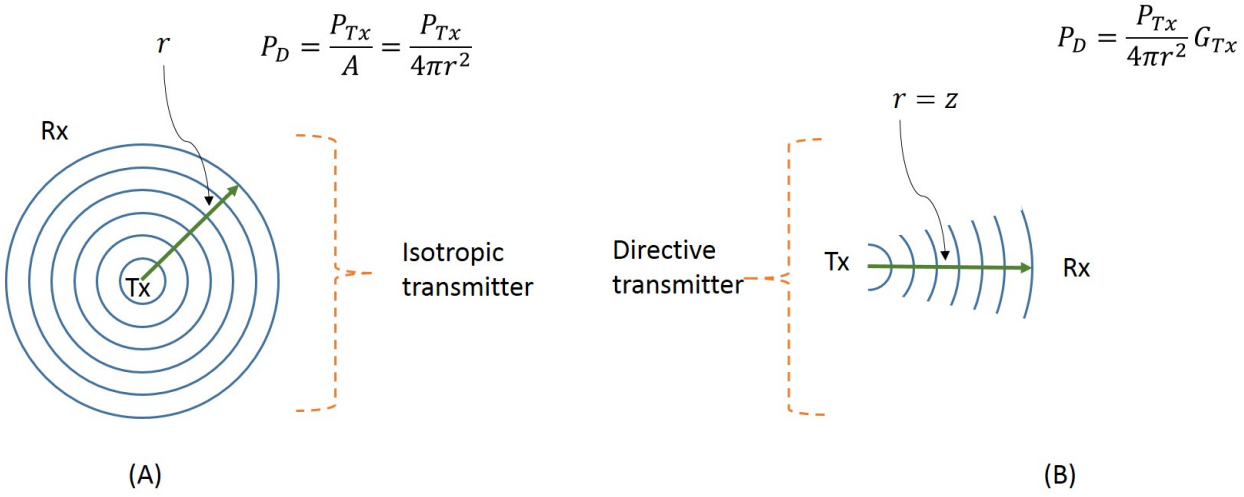


FIGURE 3.7: (A) A isotropic transmitter and (B) a directive transmitter sending signals in space.

the signal radiates in all directions and the power density is given by

$$P_D = \frac{P_{Tx}}{A} = \frac{P_{Tx}}{4\pi r^2}. \tag{3.8}$$

In a directive transmitter shown in fig 3.7(B) the signal radiates outwardly in a particular direction. The power density is given by

$$P_D = \frac{P_{Tx}}{A} G_{Tx} = \frac{P_{Tx}}{4\pi r^2} G_{Tx}. \tag{3.9}$$

For a receiver located at a distance z, the received power is given by

$$P_{Rx} = P_D A_{Rx}, \tag{3.10}$$

where A_{Rx} is the surface area of the receiver given by

$$A_{Rx} = \frac{G_{Rx}\lambda^2}{4\pi}, \tag{3.11}$$

G_{Rx} and G_{Rx} are the antennae gains (signals) at the transmitter and receiver respectively. Substituting Eqs 3.11, 3.9 into Eq 3.10 we obtain

$$P_{Rx} = P_{Tx} G_{Tx} G_{Rx} \left(\frac{\lambda}{4\pi z} \right)^2. \tag{3.12}$$

Equation 3.12 is known as the Friis transmission equation. Equation 3.12 approximates the power in (Watts) at the receiver located at distance z. The derived Eq 3.12 excludes the effects of attenuations due to the atmosphere, optics and geometric loses. A beam propagating in a random media will be attenuated and the power at the receiver is inversely proportional to the losses attained. Equation 3.12 can be modified to be

$$P_{Rx}[W] = \frac{P_{Tx}G_{Tx}G_{Rx}\left(\frac{\lambda}{4\pi z}\right)^2}{L_{sys}L_{turb}L_{atm}L_{rain}L_{geo}}. \tag{3.13}$$

The equations for calculating the optical field attenuations in the atmosphere Eq 3.2, rain Eq 3.4, turbulence Eq 3.5 and geometric losses Eq 3.7 are all in decibel units (dB). In order to convert from watts to dB we use the relation

$$P_{dB} = 10\log_{10}\left(\frac{P_W}{1W}\right). \tag{3.14}$$

Applying Eq 3.14 to 3.13 we obtain the total power P_T received at the detector of any free space communication system is given by the link budget equation

$$P_{Rx} = P_{Tx} - L_{sys} - L_{geo} - L_{atm} - L_{Rain} - L_{turb}. \tag{3.15}$$

Figure 3.8 shows a theoretical plot of all the losses incurred according to the inputs in Eq 3.15. The vertical axis represents the power losses and the horizontal axis represents the losses incurred in the free space link. The plot depicts that most of the losses in the communication link are associated with geometric losses, atmospheric loses and system losses. The red line represents detector sensitivity, the green line is the calculated link budget for a good communication link and the yellow is for bad link budget. For a free space communication link to perform optimally the calculated power at the receiver should be higher than the threshold power of the detector.

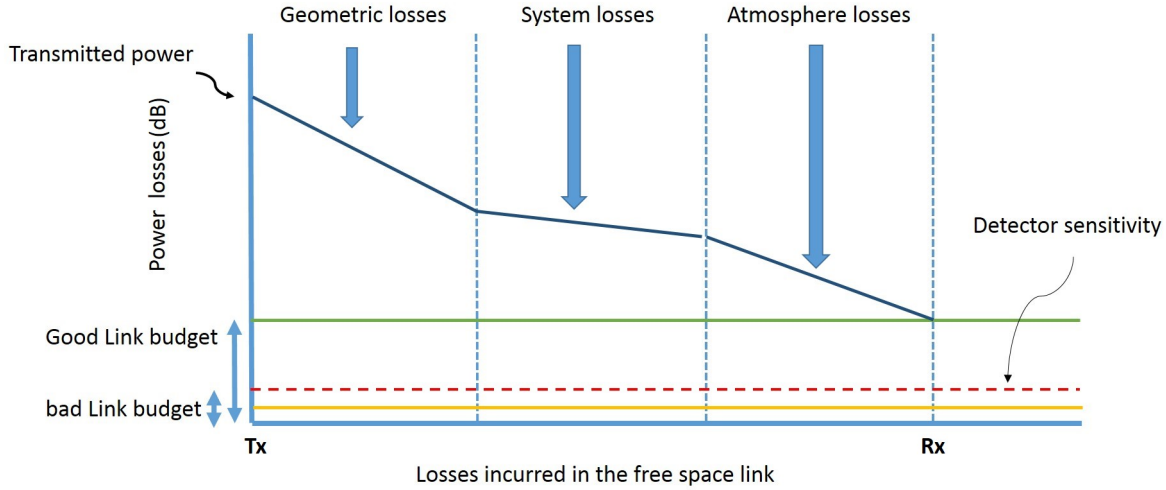


FIGURE 3.8: A theoretical graph for a communication link with a good link budget and as well as the losses incurred according to Eq 3.15. The red line shows the detectors sensitivity and the green line shows the power at the receiver.

3.2.1 Optical setup attenuation

In any optical setup in the lab, the optics used to build a communication link all have losses. This could be due to lens misalignment, transmitter and receiver losses, reflection losses from mirrors and absorption losses from the SLM. These components all have tolerances and optical performances in terms of how much light will be reflected off the optics surface. The type of mirrors used are Thorlabs protected silver mirrors with a reflectivity of 97.5% for all wavelengths. When we want to know the theoretical losses from the optics for a transmitted power P_{Tx}, we should know all the theoretical percentage losses or absorption. The SLM used diffracts 80% of the light into the first order, where α_{SLM} is the reflectivity of the SLM. The power P_1 in the first order is given by

$$P_1 = P_{Tx}\alpha_{SLM}. \tag{3.16}$$

If we call R_{mirror} the reflectivity of the mirror, then the transmitted power using n number of mirrors is given by:

$$P_2 = P_1 R_{mirror}^n. \tag{3.17}$$

Then if we call T_{Lens}^m the transmission for m number of lenses used, then the transmitted power is given by:

$$P_3 = P_2 T_{Lens}^m. \tag{3.18}$$

Therefore the total power transmitted through all the optics is given by:

$$P_{tran} = P_{Tx}\alpha_{SLM} R_{mirror}^n T_{Lens}^m. \tag{3.19}$$

From this we can calculate the losses due to the optics as

$$L_{sys} = P_{Tx} - P_{tran} \tag{3.20}$$

and therefore

$$L_{sys} = P_{Tx}\left(1 - \alpha_{SLM} R_{mirror}^n T_{Lens}^m\right). \tag{3.21}$$

Equation 3.21 can be modified to include any other losses of components used in the optical setup provided we know how much of the light is absorbed or transmitted. Fig 3.9(A) shows a plot of transmission as a function of wavelength for uncounted fused silica lenses. Fig 3.9(B) shows a plot of reflectance as a function of wavelength for the silver coated mirrors. From these figures we can extract the R_{mirror} and T_{Lens} values for a specific wavelength and use Eq 3.21 to calculate the system losses.

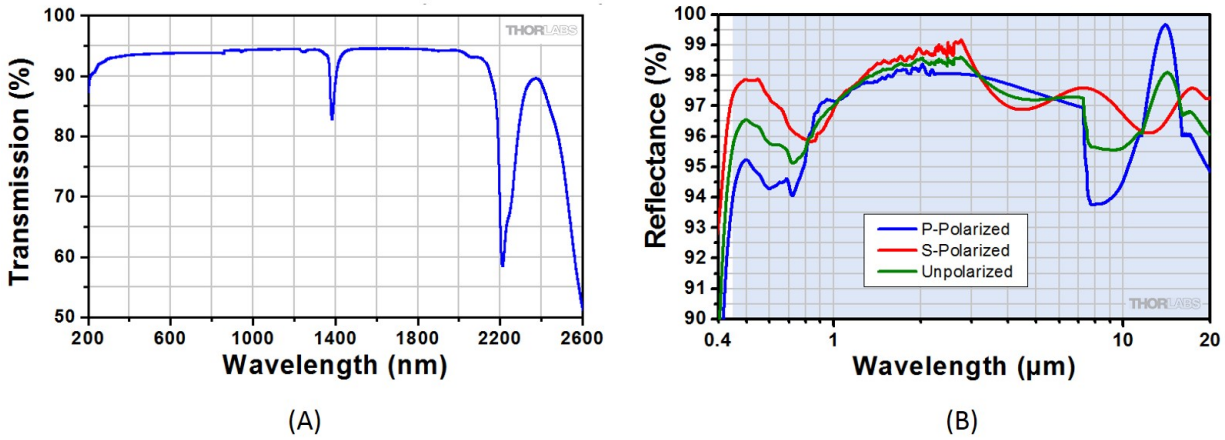


FIGURE 3.9: (A) A plot of transmittance as a function of wavelength for uncoated fused silica [66] and (B) a plot of reflectance as a function of wavelength [67].

3.2.2 Link budget calculation

Link budget analysis was performed by making use of all the formulas stated in this chapter and together with the measured values. The communication link was established using the 532 nm source. A power meter that is able to measure a maximum of 10 mW was used to measure the power within the system. A comparison between predicted values and experimental values are outlined in Table 3.1.

In the table above we show a summary of all the parameters and losses in the communication link. In most communication links geometric losses contribute more. However, to compensate for these losses we chose to use a bigger receiving lens that will collect all the light. Atmospheric losses are more prominent in this case and these included scattering and losses due to weather conditions. The measured power after the receiving lens and all other optics is 12.45 dBm which is above the cameras sensitivity of -40 dB. In most weather conditions the link will perform optimally, this is due to the fact that on rainy or sunny days the power received at the detector is not less than the detectors sensitivity.

Link parameters		
Transmitter aperture diameter	50.8 mm	
Receiver aperture diameter	152.4 mm	
Wavelength	532 nm	
Link range	150 m	
Height above ground	9 m	
Laser power	16.98 dBm (50 mW)	
Number of lens before transmitter	8	
Number of Mirrors before transmitter	11	
Camera sensitivity	-40 dBm	
Beam divergence	collimated	
Receiver focal length	1500 mm	
Transmitter power	13.584 dBm	
	Predicted value	Measured value
Rx power	18.82 dBm	12.45 dBm
System loses	-15 dB	-24 dB

TABLE 3.1: A comparison between predicted and experimental values of the link budget.

3.3 Turbulence analysis

Plane wave theory on turbulence was applied to measure optical turbulence by Andrew et al [21]. Many studies and experiments have been performed in measuring optical turbulence in real time using a similar optical setup to that in this project [68; 69; 70; 71; 72; 73]. The experimental setup in fig 3.10 was built. This setup monitored the effects of beam wander and measured the intensity variance at the focal plane. The magnitude of the short-term beam wander depends on the refractive index structure parameter and the communication link distance. In order to make a correct measurement we needed to have a detecting system that is able to capture all the movements of the beam. We needed to know the frequency of the beam when it reaches the detector and this is given by the Greenwood frequency [21]. The Greenwood frequency is given by

$$f_G = 2.31\lambda^{-6/5}\left[\int_L C_n^2(z)\, Ws^{5/3}(z)\, dz\right]^{3/5} \tag{3.22}$$

where λ is the wavelength of a laser, L is the distance between the receiver and transmitter, WS is the wind speed and C_n^2 is the optical turbulence parameter over the propagation distance z. The Greenwood frequency was found to be around 100 Hz. We used a Point grey camera that is able to operate at 150 MHz which was sufficient to record the beam wander. In a lab, very weak turbulence conditions will be present, this is due to lab climate conditions and building sway [74]. To have a very accurate measurement, background measurements were taken into account and subtracted

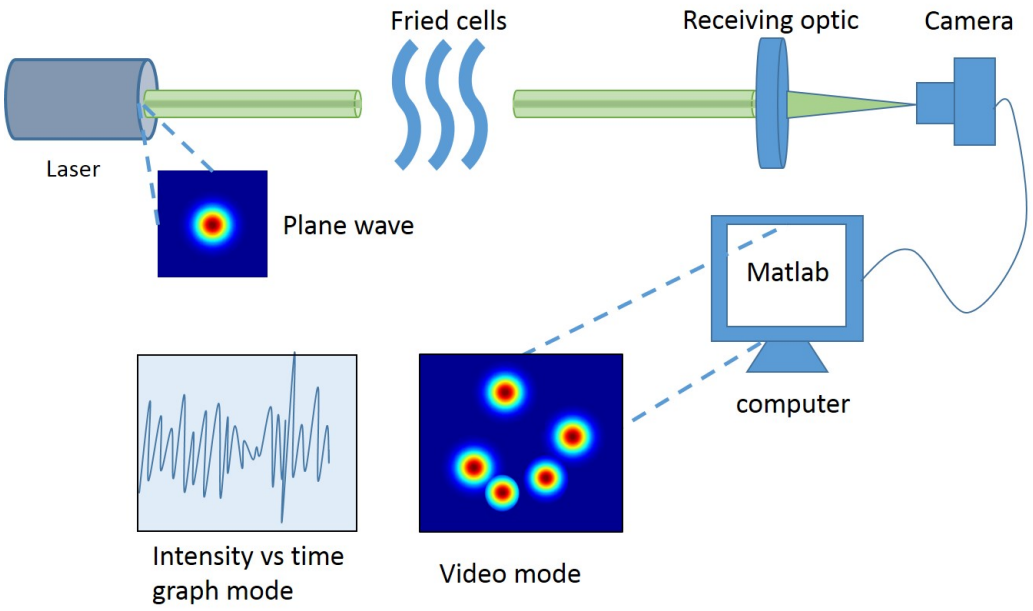


FIGURE 3.10: In order to measure the optical turbulence parameter we sent a plane wave that interacted with Fried cells or turbulent eddies and captured using a 200mm lens which focused the beam onto the camera for analysis.

from the measured values. When the beam was propagated in the atmosphere, optical turbulence present altered the intensity's centroid position causing beam wander. It is from this observation that we measure the variance in intensity and use the Rytov weak turbulence theory to measure optical turbulence.

The measured value of the optical turbulence parameter C_n^2 was compared to the predicted optical turbulence parameter that was obtained from the models discussed in Chapter 1. The received data from the South African Weather Service were measured from 1 km above ground, meaning that the predicted values for the optical turbulence parameter would correspond to a height of 1 km above the ground. The communication link was established at 9 m above the ground, meaning that for meteorological values obtained at 1 km would give a slightly different optical turbulence parameter than those obtained at 9 m. Fortunately the Tatarskii model can be used to re-scale values obtained for elevations of 1 km above the ground to 9 m above the ground according to

$$C_n^2(h) = C_n^2(0)\, h^{-4/3}. \tag{3.23}$$

Where $C_n^2(0)$ is the optical turbulence parameter at the surface of the ground. The accuracy of the models used in calculating the optical turbulence parameter C_n^2 is performed by finding the relative errors between measured and calculated values. The affects of the meteorological values (temperature, wind speed, humidity and pressure) into the models will be assessed as well. The models were implemented into an Excel spreadsheet where data fitting was performed. On 23 November 2017, the temperature parameter varied between 13 °C to 31 °C with a standard deviation of 4.6 °C, the wind

speed was between 0.1 m/s to 2.5 m/s and with a standard deviation of 0.8 m/s, the pressure was between 86.41 kPa to 86.77 kPa with a standard deviation of 0.9 kPa and the humidity was between 13% to 61% with a standard deviation of 12%. The graphs showing the comparison between temperature fig 3.11 (A), Wind speed 3.11 (B), pressure 3.11 (C) and humidity 3.11 (D) over 23 and 24 of November are shown. Pressure has a relatively small influence in the value of optical turbulence which could also imply that wind speed does not have much influence. However wind speed plays an important part in the distribution of energy in the atmosphere and movement of air cells [75]. From

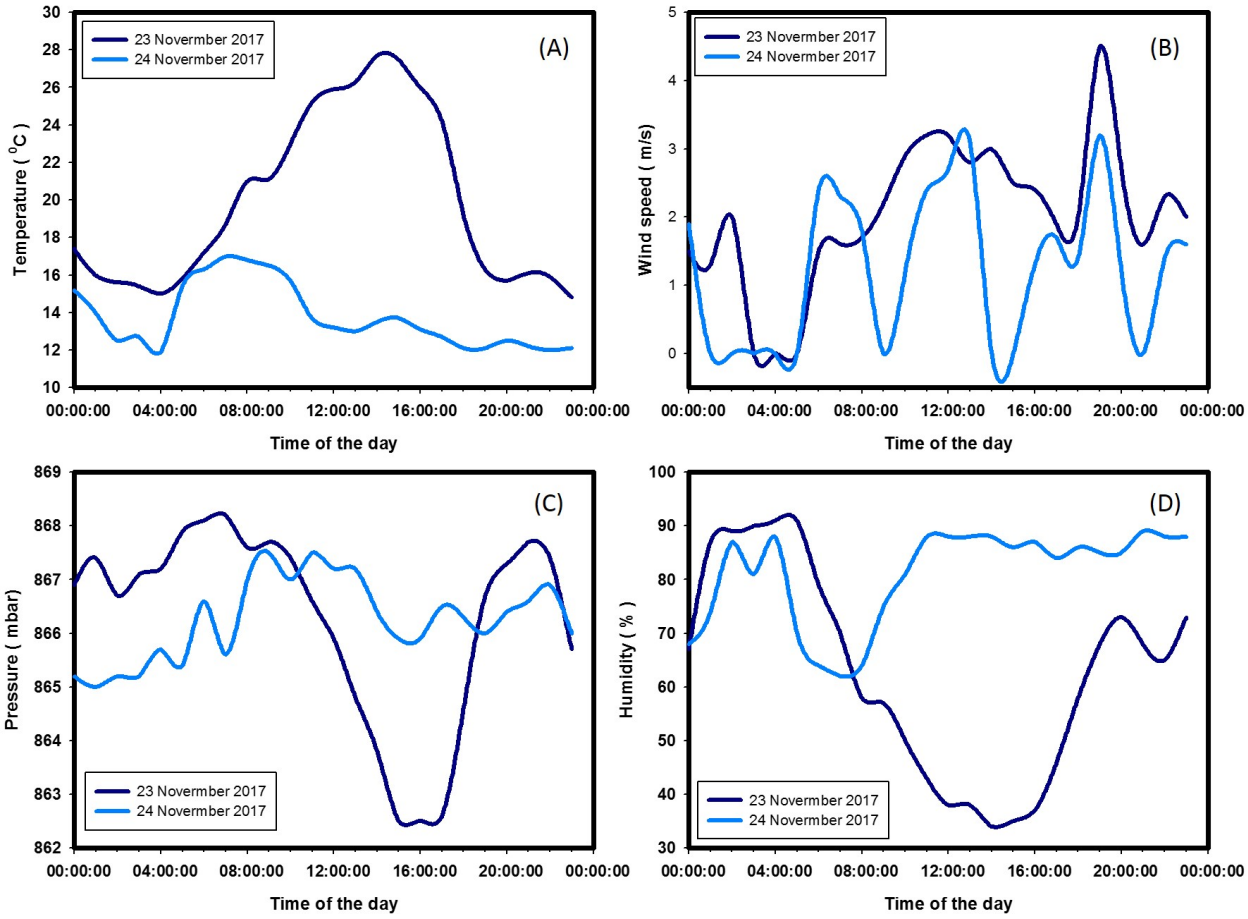


FIGURE 3.11: A comparison plot between (A) temperature (B) wind speed, (C) pressure and (D) humidity over 23^{rd} of November and 24^{th} of November 2017.

fig 3.13 and 3.12 we see that the only model that is able to match with the measured C_n^2 values is the PR model (A) whereas PAMELA (B) and HV model (C) give a big discrepancy.

On the 23 of November the minimum measured value for the optical turbulence parameter was $3.21 \times 10^{-14} m^{-\frac{2}{3}}$ where the humidity was at its peak at 50% and the temperature was 16.1°C and the wind speed was 1.2 m/s at 5 am. The maximum value for the optical turbulence parameter was $1.35 \times 10^{-13} m^{-\frac{2}{3}}$ with 22% humidity, 27.3°C and a wind speed of 2.3m/s at 11 AM. The standard deviation for the optical turbulence parameter for day 23 November 2017 was $9.46 \times 10^{-14} m^{-\frac{2}{3}}$ which is close to $1 \times 10^{-13} m^{-\frac{2}{3}}$ and this accounts for a strong turbulence condition according to the

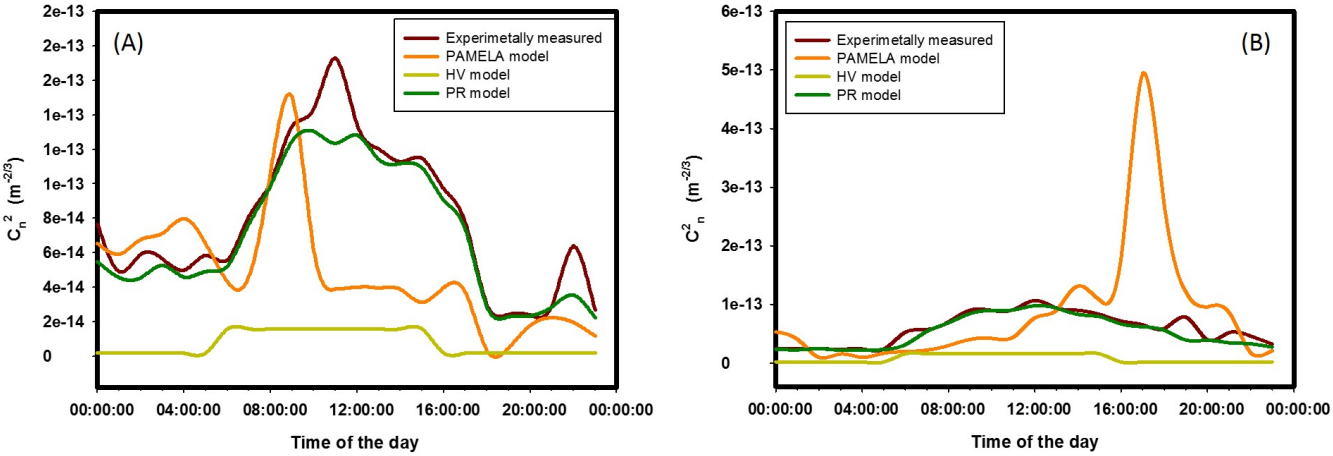


FIGURE 3.12: Diurnal measurement of the optical turbulence parameter compared with calculated values using various models (A) 23 November 2017 and (B) 24 November 2017.

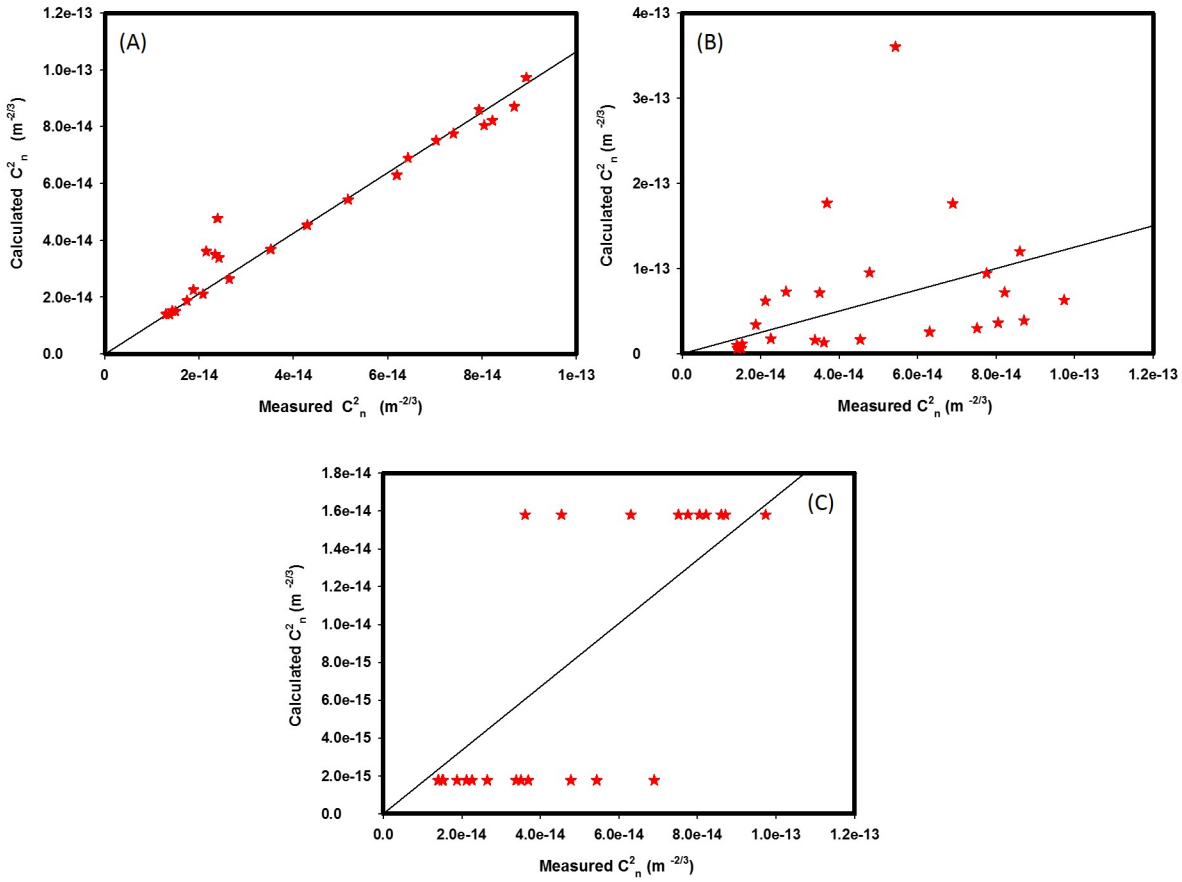


FIGURE 3.13: Calculated versus measured C_n^2 values for (A) PR model, (B) PAMELA model and (C) HV model.

Kolmgorov theory of turbulence [21]. On the 24 of November, the weather conditions were different as there was rain which varied between 1.4 to 4 mm/h. This had an influence in the performance of

the link in which the received modes where stable (beam wander was minimal compared to other days) but the intensity of the modes was lower. In fig 3.12 the maximum value of the optical turbulence parameter peaked at $1.23 \times 10^{-13} m^{-\frac{2}{3}}$ which was a 9% drop from the previous day. This was to be expected since the temperature was now cooler and more humid as compared to weather conditions on the 23^{rd} of November. The effects of the drop in optical turbulence can be seen from fig 4.6. The detected modes had less crosstalk on the 24^{th} of November compared to 23^{rd} of November. From

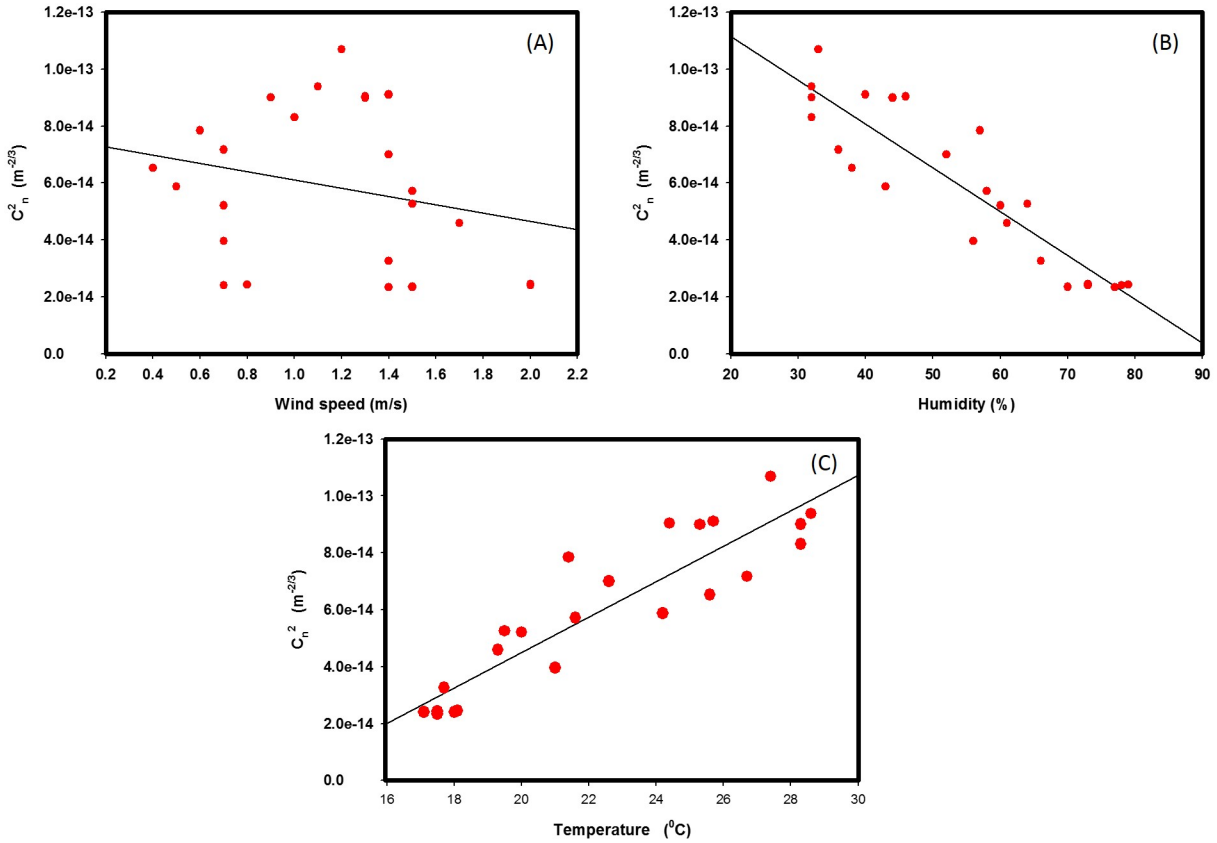


FIGURE 3.14: Shows the optical turbulence parameter for 24 November 2017. A plot between optical turbulence and wind speed (A), humidity (B) and temperature (C) was made. Temperature and humidity have a strong correlation with optical turbulence whereas wind speed has no known influence.

fig 3.14 we see that temperature and humidity have a strong correlation with the optical turbulence parameter, whereas wind speed does not correlate. The fact that the wind speed does not correlate with optical turbulence does not suggest that there is no dependency. In fig 3.15 a density plot of the C_n^2 values is shown plotted as functions of temperature, wind speed and humidity. This graph shows the dependency of the C_n^2 values on the meteorological values. On a hot and windy day the C_n^2 values will increase fig 3.15 (B). On a windy and less humid day the C_n^2 values will increase fig 3.15 (C). On a hot and less humid day the C_n^2 values will increase fig 3.15 (A). From these plot we see that wind speed does have an influence on the optical turbulence parameter.

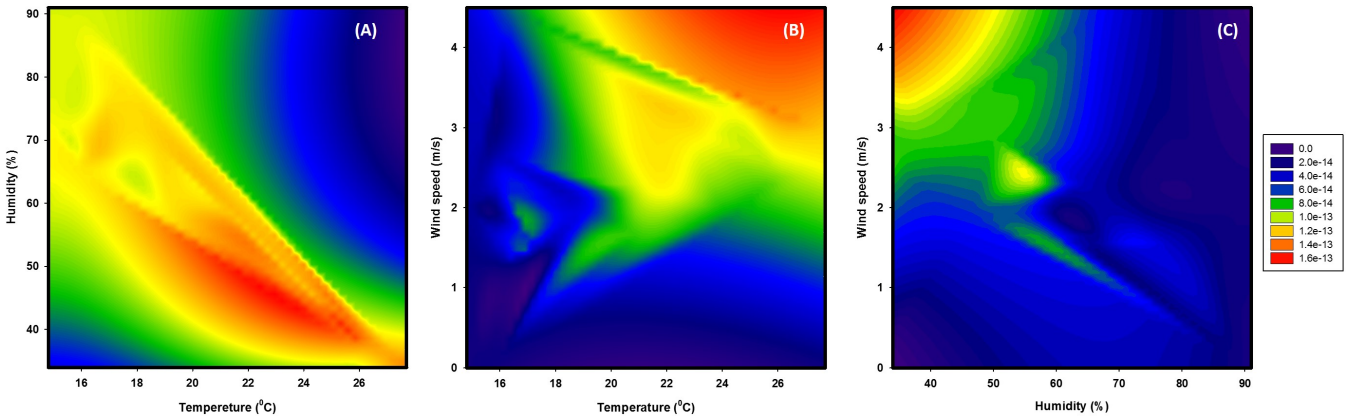


FIGURE 3.15: A density plot of the C_n^2 values is shown plotted as functions of temperature, wind speed and humidity

We also calculated the Fried parameter from measured optical turbulence parameter values based on Eq 1.80. The Fried parameter physically represents the spatial extent over which the phase of a propagating optical beam will remain the same. In fig 3.16 (A) the Fried parameters throughout 23 November were relatively small compared to Fried parameters in 24 November. The effects of the Fried parameter on the image formation at the receiver is charactered by the Strehl ratio. We see that the quality of the modes received at the detector in fig 3.16 peaked at 90% at 5 am on the 24 of November, only 80% of the image quality was formed at the same time on the 23 of November.

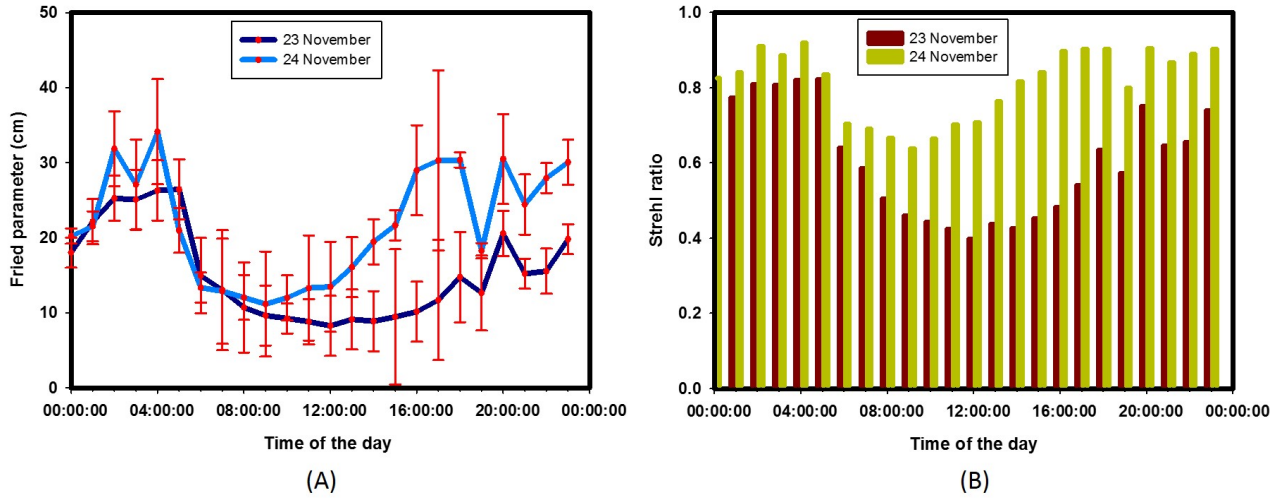


FIGURE 3.16: A plot of the Fried parameter on 23 November 2017. The relative errors between theory and measurement are plotted on the secondary axis.

Chapter 4

Data transfer over distance with spatial modes

Communication using the spatial modes of light requires the sent modes to be distinguishable from one another. In theory an infinite amount of information can be sent since each mode is characterized by the topological charge l and radial index p. In this study we employed vortex modes and LG modes to send information in free space. We chose to work with these modes as they carry OAM throughout their propagation, maintaining their orthogonality. These modes have been used extensively to send information both in the classical [76; 77; 78; 79] and quantum regime [80; 81; 82]. However, due to the effects of optical turbulence and the beam attenuation by the atmosphere, detection of the modal content of the received spatial modes has proved to be difficult. Here we present long distance data transfer using spatial modes between two buildings at the South African Council for Scientific and Industrial Research (CSIR) in Pretoria.

4.1 Data transfer analysis

Link design and planning before constructing the communication link was of paramount importance. Using quality optics from reliable manufacturers was also important. During this investigation we increased the link distance from $z = 0$ to 10 and 150 meters. We first demonstrated communication between the receiver and the transmitter with no propagation distance as a proof-of-concept. The generated modes (sender) were imaged from one plane of the SLM to the other (i.e receiver). The techniques employed for encoding information was complex amplitude modulation and phase-only modulation techniques discussed in Chapter 2 to create structured light fields (i.e LG mode and vortex modes respectively). The detection method employed was the modal decomposition method where the on-axis intensity was monitored for either a peak or a null. The long distance communication link spanned a distance of 150 m. On one side of the building a retro-reflector was mounted and its function was to reflect the laser beam back inside the lab which was located 75 m away. To protect the retro-reflector against rain we designed a cover. The design of the covering is shown in fig 4.1. We proceeded to build the communication link according to fig 4.2. The schematic was meant to be incorporated with the mid-IR diode but due to damage, we proceeded with the 532 nm laser diode.

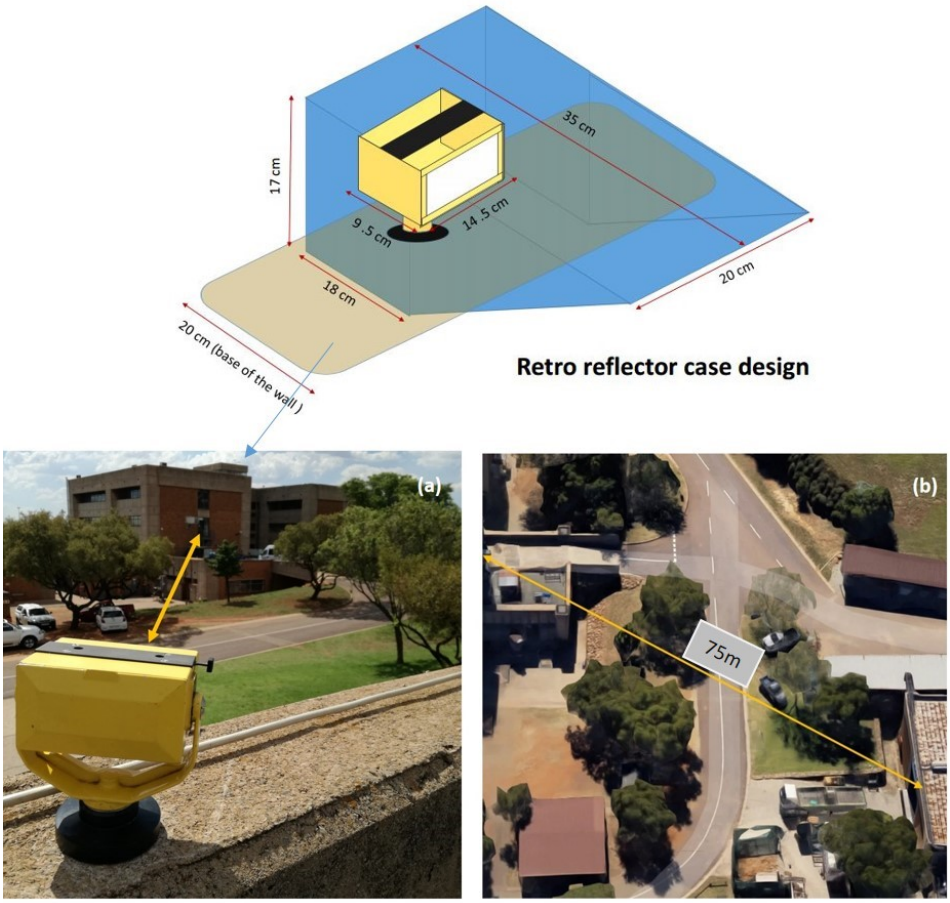


FIGURE 4.1: (A) An angled view of the link between the two buildings at the CSIR. A retro-reflector was used to reflect back the laser beam in to the lab for detection. (B) a Google Earth image showing the top view of the CSIR buildings over which the link is located. The distance between the two buildings was 75 m totalling 150 m.

The first SLM was used as an encoder or transmitter of our spatial modes (vortex and LG modes) that were propagated over the communication link. The output beam from the transmitter was then analysed by modal decomposition using a second SLM.

Azimuthal decomposition (vortex mode) and LG decomposition (LG modes) was performed at three distances. The size of the detected modes were between 1.42 mm to 2.45 mm in radius for modes $l = [-5, 5]$ at $z = 0\ m$. The size of the modes were between 14.2 mm to 24.5 mm in radius for modes $l = [-5, 5]$ at $z = 10\ m$ and $150\ m$. A telescope was used to magnify the beam to ensure that we worked within twice the Rayleigh range of the 150 m communication link. This was to reduce the rate at which the beam spreads so that it can fit within the receiving optic. Optical turbulence also had an effect on the final beam size. The beam size of the LG modes scales linearly with the topological charge l and radial index p according to [83]

$$w_{LG} = w_0\sqrt{2p + |l| + 1}. \tag{4.1}$$

The magnitude of the intensity of our modes scales linearly with the topological charge l for both

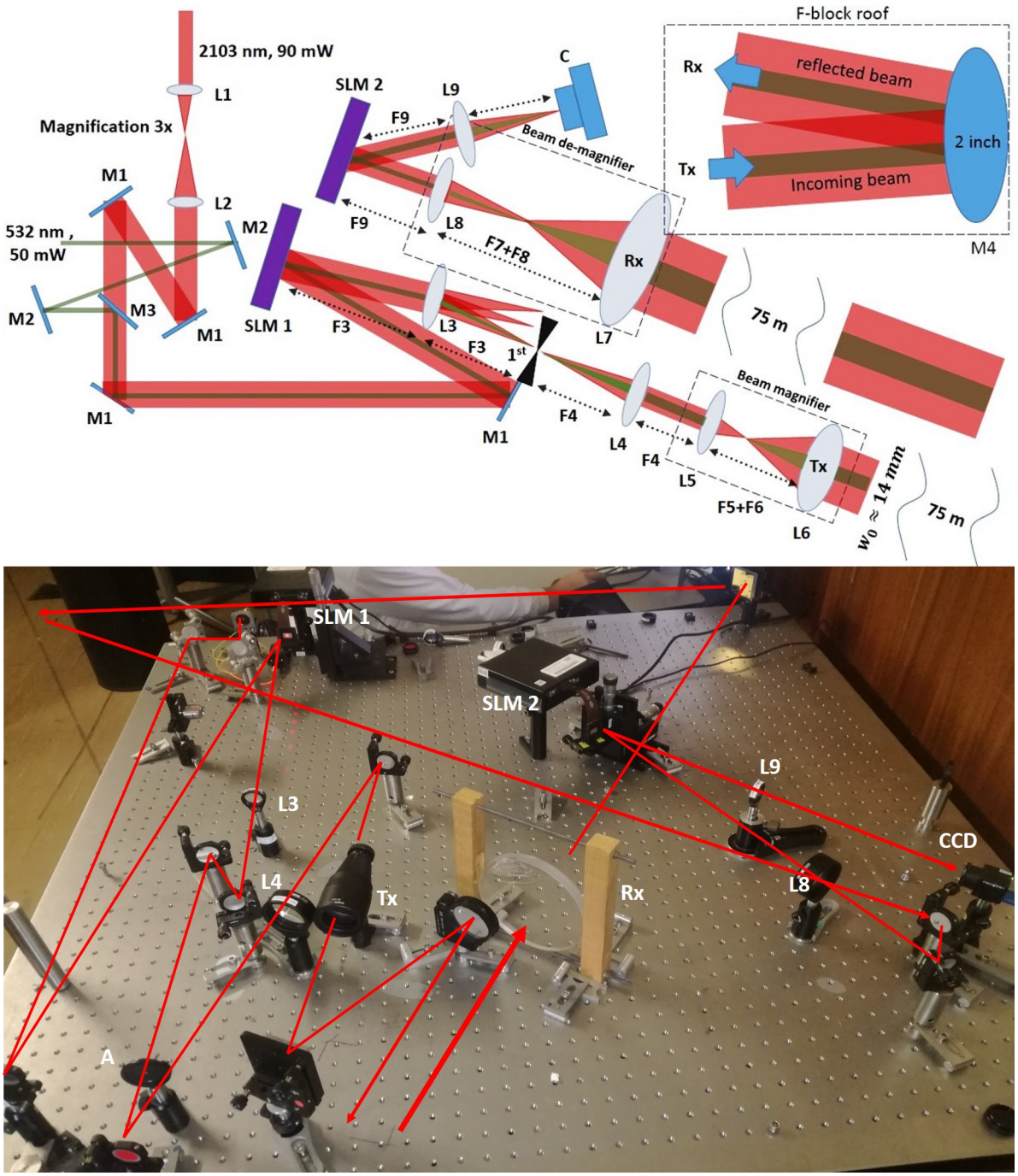


FIGURE 4.2: We followed the schematics outlined to establish the communication link. Where L-lens, M-mirrors, F-focal length, C-Camera, Tx-transmitter and Rx-receiver.

vortex and LG modes as it is expected for holographic generation without intensity shaping [83]. The entire experimental setup was checked for alignment. We verified this by reflecting the beam emerging from the transmitter directly backwards to the optics to see whether it travels in the same direction it came. The results in fig 4.4 show a crosstalk matrix over $z = 0$ m and $z = 10$ m for both azimuthal decomposition and LG decomposition. We also performed a modal decomposition of LG modes for various p and l over a distance $z = 0$ m as shown in fig 4.5. The cross talk is the

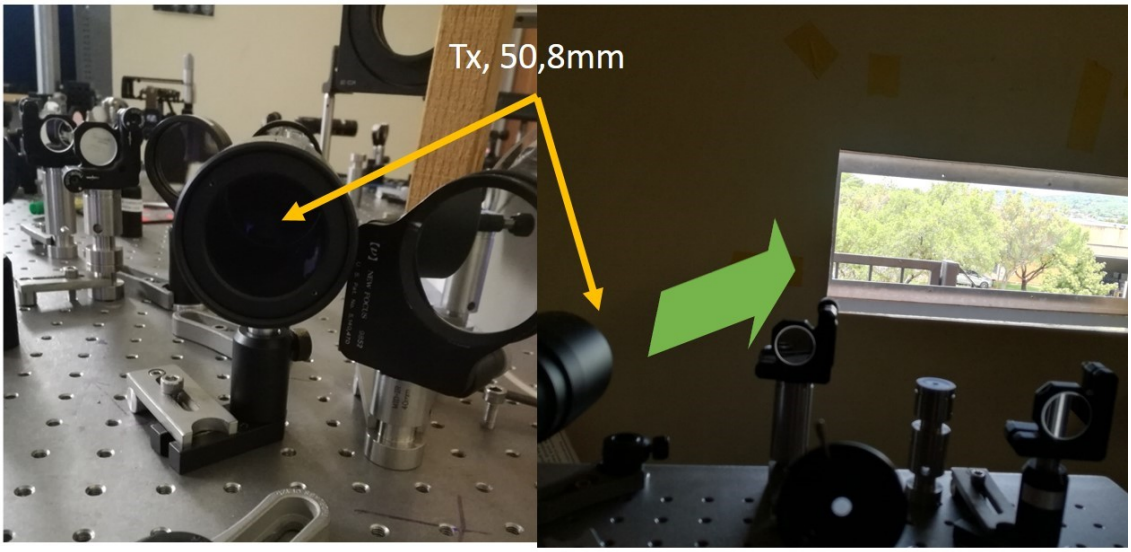


FIGURE 4.3: (A) The two inch transmitter in the lab setup and (B) the window from which the laser was transmitted outside.

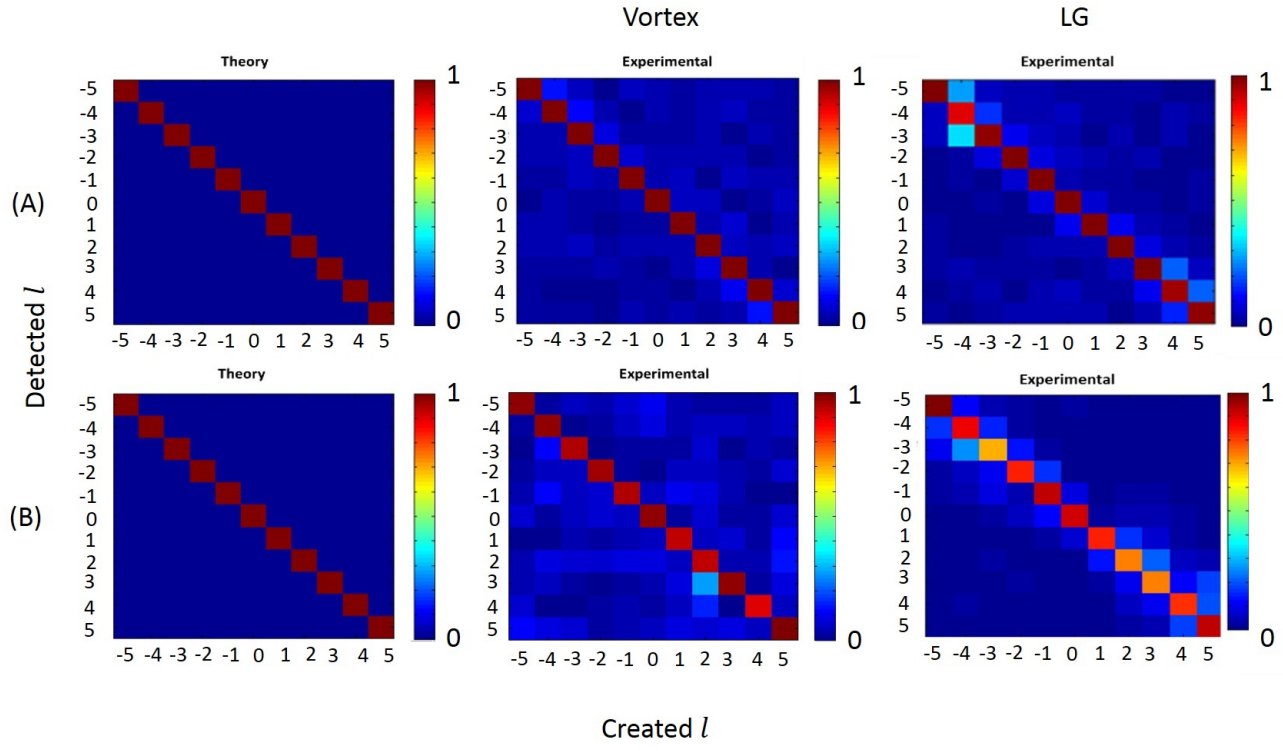


FIGURE 4.4: Decomposition results over (A) $z = 0m$ and (B) $z = 10m$ for both vortex and LG modes

measure of how much energy was shared between the modes. The theoretical plots show how an ideal communication system should perform in the absence of cross talk. From fig 4.6 it is evident

that there is good agreement between theory and experiment. The decomposition results for $z = 150$

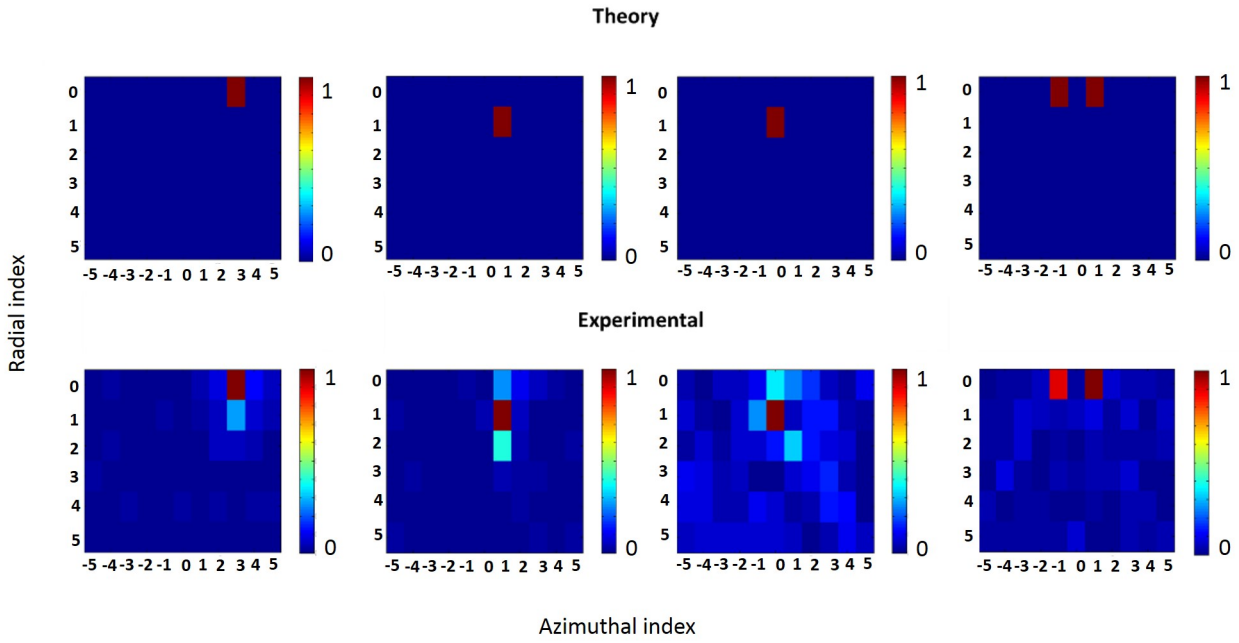


FIGURE 4.5: Decomposition of LG modes for various p and l

m are shown in fig 4.6. The results we taken at specific times of the day on different days (23 and 24 of November 2017). The decomposition results were taken at 12 pm and 12 am on the same day for comparison. The objective in establishing a communication link is to demonstrate data transfer. Using the results obtained from the azimuthal and LG decomposition we were able to demonstrate information transfer represented by a grey scale picture using 11 free space modes.The data transfer was performed with the experimental setup based on raw data received from the system in which we simulated how the received image would have been transmitted in real time. Matlab was used to write a program which performed multiple vector multiplications (the code is found in the code appendix section). An image made up of a square matrix of 400×400 pixels was rescaled to be made up of 11 grey scale values.

In fig 4.7 we used the crosstalk matrices to simulate real data transfer. The correlation between the received and sent image was calculated. A single measurement crosstalk matrix was used to simulate real data transfer and we found a 88.49% agreement between the sent and received image. For the averaged crosstalk matrix we found a 99.56% agreement between the sent and received images.

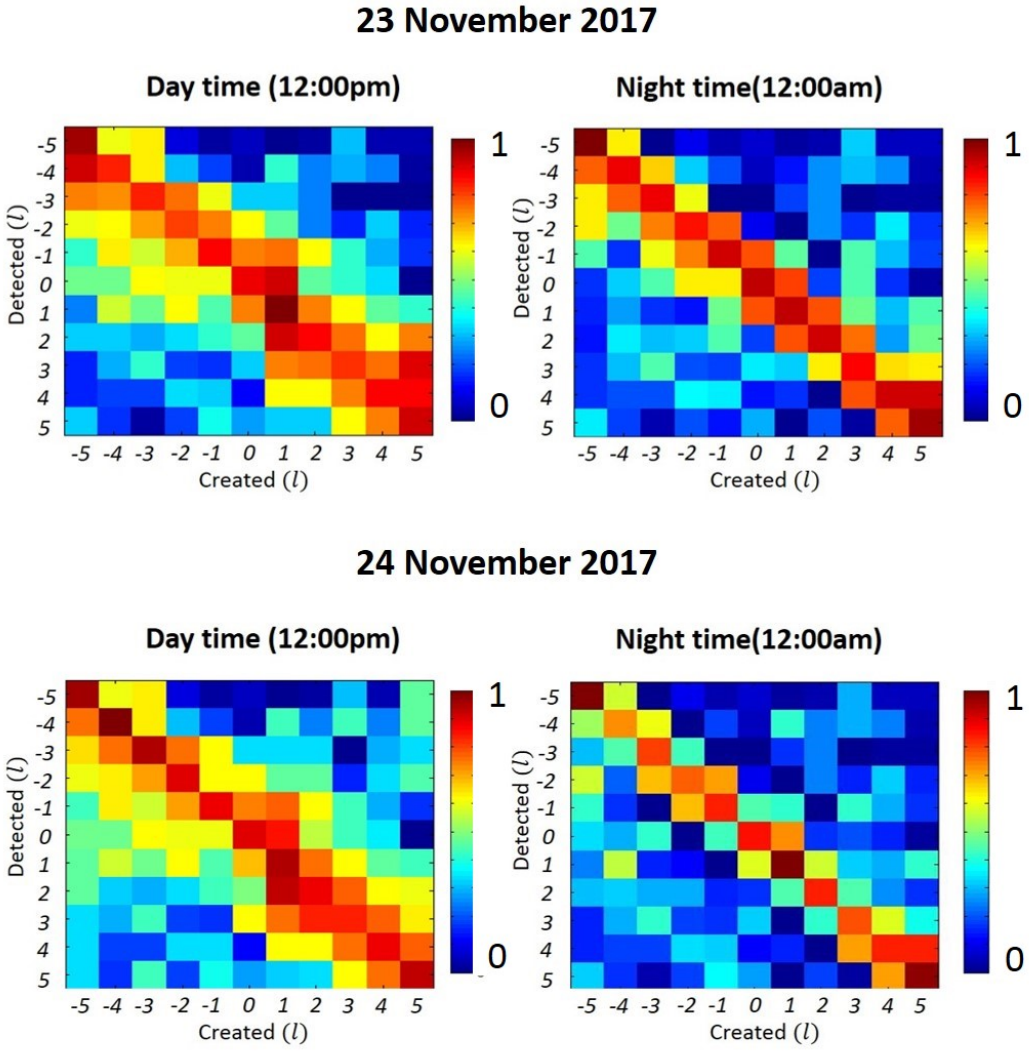


FIGURE 4.6: LG decomposition results over the 150m link. The cross talk during day time was more severe compared to night time. a single measurement was averaged over 50 measurements to get result.

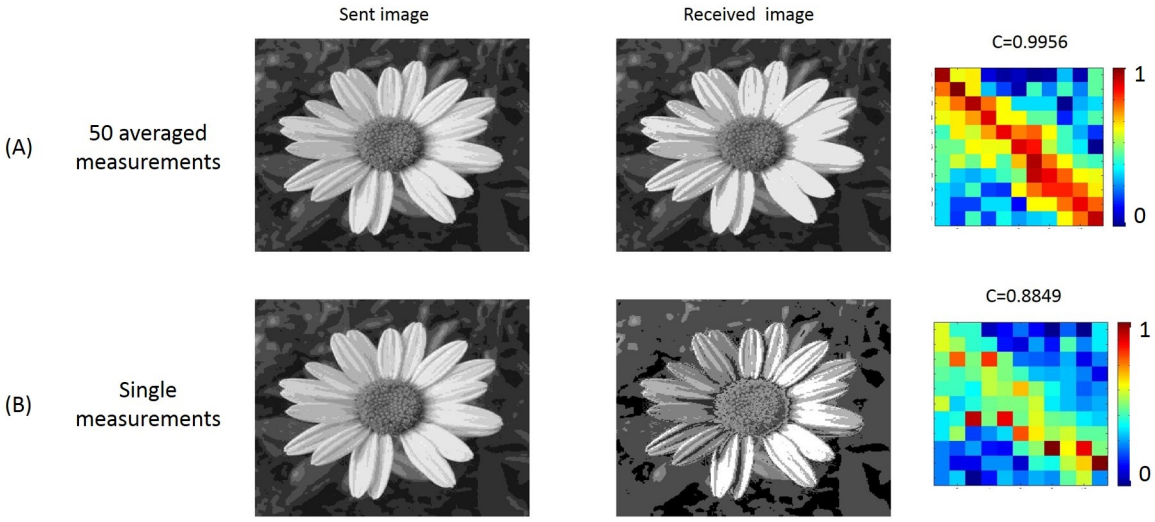


FIGURE 4.7: Simulation of data transfer using the crosstalk matrix that was over (A) 50 measurements and also (B) data transfer over a single measurement. The correlation between sent and received image was 0.9956 as compared to a single measurement with 0.8849.

Chapter 5

Conclusions and future work

In this dissertation we discussed how one can use the spatial properties of light to send information over a long distance. In chapter 1, the theoretical behaviour of light was discussed by using Maxwell's equations to derive the wave equation. We also discussed the various properties that arise for laser beam propagation such us the radius of the curvature, Rayleigh range, beam waist and also solutions to the wave equation i.e. Gaussian beams (fundamental solution to the wave equation), LG beams (beams that have an azimuthal and radial dependence) and Vortex beam (beams that have an azimuthal dependence). We then extended the laser propagation properties from a vacuum to a turbulent medium. The theory for propagating fields in a turbulent medium are discussed based on the Kolmgorov model of turbulence. The theory showed the influence of large turbulent cells on the laser beam that resulted in beam wander and also the influence of small turbulent cells which resulted in beam scintillation. We also modelled optical turbulence by making use of three models: The Pamela model, Hufnagel-Valley model and Polynomial regression model. These models use meteorological data such as temperature, wind speed, pressure and humidity as inputs (received from the South African Weather Services) to estimate the strength of optical turbulence.

In chapter 2, we discussed how we can generate and detect light beams that carry orbital angular momentum (OAM) by making use of a Spatial Light Modulator (SLM). We first gave an introduction to how SLMs work and how we also implement holograms to shape light dynamically. The creation and detection was demonstrated in the lab as a proof-of-concept by showing the various LG intensity profiles and the results from their modal decomposition which where in good agreement with theoretical predictions with an error of 2%. We also discussed the importance of calibrating SLMs before implementation and how we calibrated SLMs using interferometric techniques. In chapter 3, we discussed the importance of a link budget and how we can calculate the losses that incur as the laser beam propagates through optics and in free space. We proceeded further by measuring the optical turbulence strength by using a simple setup and compared it with theoretical predictions from the optical turbulence models discussed in chapter 2. We found that the measured experimental data for optical turbulence was in good agreement with the Polynomial regression model as shown in other literature [84] whereas the Pamela model and Hufnagel-Valley model were not in agreement with measured data. Other parameters where calculated these include the Fried parameter and Strel ratio

which describe the image formation or the quality of the data received at the detector. It was noted that on a clear day with and less turbulence in the atmosphere the quality of the intensity profiles of the modes received was 90% and on a gloomy day it peaked at 80% but nevertheless the link was still efficient.

In chapter 4, we then extended the link to 150 meters long link at the CSIR campus between two buildings. The distance between the two building was approximated to 75 meters by using the Google earth application. A retro-reflector was mounted on one of the two building so as to transmit the light back. Eleven Vortex modes were prepared and sent across the link. The crosstalk matrix which quantifies the modal power sharing between adjacent modes was calculated. We found that over a single measurement the crosstalk was almost 12% and when we averaged the results from multiple modal decompositions the crosstalk lowered to a value of 1%. Using the modal decomposition result from a single and averaged measurement we then simulated data transfer with a gray scale image of a flower scaled down to 11 values ranging from back to white. The correlation between the sent image was shown to be 99.56% for 50 averaged measurements while it was 88.49% for a single measurement.

The link was robust in sending data across the 150 meters and we wish to test other types of spatial modes as future work that are non-diffracting and self healing such as long distance Bessel beams [85; 86]). We also wish to multiplex multiple modes so as to increase the data capacity.

Appendix A

Matlab codes

```
%%%%%% Convert data from crosstalk matrix to grayscale values %%%%%%

%%% Use this if the code and images are in different folders.
% path = 'C:\Users\Downloads\';
% data = csvread([ path 'Azimuthal_deco_10m.csv']);
% picture = double(imread([path 'image to be sent.jpg']));

data = csvread('modal_night_time.csv');

normdata = zeros(size(data));
for lauf = 1:size(data,1)
    normdata(lauf,:) = floor(data(lauf,:)./max(data(lauf,:)));
end
inputvector = (1:size(data,1));
outputvector = zeros(size(inputvector));

for lauf = 1:length(outputvector)
     outputvector(lauf) = find(normdata(lauf,:) == max(normdata(lauf,:)));
end

%%%%%% Encoding an image using 11 grayscale values %%%%%%

%%% Rescale the image to have 11 grayscale values

picture = double(imread('image to be sent.jpg'));
scale = length(outputvector)-1;
sentpicture = uint8(picture./max(picture(:))*scale)+1;
imagesc(sentpicture);

%%% Produce received image using the mapping in outputvector
receivedpicture = zeros(size(sentpicture));
for lauf = 1:size(sentpicture,1)*size(sentpicture,2)
    idx = sentpicture(lauf);
    receivedpicture(lauf) = outputvector(idx);
end

%%% Display images
figure('units','normalized','outerposition',[0 0 1 1]);
subplot(1,2,1)
imagesc(sentpicture); axis off; title('Image sent')
subplot(1,2,2)
imagesc(receivedpicture); axis off; title('Image received')
r = corr2(sentpicture,receivedpicture) %%% Compute correlation between sent and recieved image
```

FIGURE A.1: Simulation code for sending information using the cross talk matrix

```
clear all
clc
% Code by Lucas Gailele

user_input_time = 60*60*24; % in seconds ((over 24 hours)
L=150; % Communication distance
lambda=0.532e-6; % wavelength
background=10000; % noise
k=2.*pi/lambda; % wavenumber
a=k.^(7/6);
b=L.^(11/6);

cacy1= 312; % pixel location , Point detector
cacx1=447;

fprintf('Measurement started at %s\n', datestr(now,'HH:MM:SS.FFF'))
count=1;
tic;
while (toc < user_input_time)  % always include a failsafe!
  pause(0)
    vid1 = videoinput('pointgrey',1,'Mono16_1280x960');
             start(vid1)
             src.Brightness = 0;
             src.Exposure = -7.58496;
             src.Shutter = 0.006378;
             Amean = double(getdata(vid1));
             colourvalue1(count)=Amean(cacy1,cacx1)-background;
             count=count+1;
             stop(vid1); delete(vid1);
end

fprintf('Measurement stopped at %s\n', datestr(now,'HH:MM:SS.FFF'))
c1=(mean(colourvalue1.^2)-(mean(colourvalue1).^2))./(mean(colourvalue1).^2)
% Calculates the first and second momemets


Cn1=c1./(1.23.*a.*b) % Computes Rytov variance

figure(1)
 plot(colourvalue1)
```

FIGURE A.2: Code used to measure the optical turbulence parameter based on the Rytov theory

```
clc
clear all

pixel=8;
x=1024;              %6 mm width
y=1024;
yy=linspace(-(y/2),(y/2),y);
xx=linspace(-(x/2),(x/2),x);
xx=xx.*pixel*10^-6;     %Pixel pitch of SLM
yy=yy.*pixel*10^-6;
[YY ,XX]=meshgrid(yy,xx);
r=sqrt(XX.^2+YY.^2);


p=0; % azimuthal index
l=0; % radial index
w=1; %beam size
lambda=532*10^-9;
flens=1000;
k = (2.*pi)./lambda;
Focus=exp((1i.*k.*r.^2)./(2.*(flens/1000)));

Incidentbeam=lg(x,y,p,l,w,2,0,lambda,0,pixel);
 Aperture=circle(x,y,pixel,1);
%Aperture=screen2(x,y,r0,pixel);
Outbeam=Incidentbeam.*Focus;
Propbeam=convol2d(lambda,yy,xx,Outbeam,-1000/1000);
FF=Outbeam;
Farfield=convol2d(lambda,yy,xx,FF,-(flens/1000));

B1=abs(Incidentbeam.^2);
B1=B1./max(B1(:));
B2=abs(Outbeam.^2);
B2=B2./max(B2(:));
B3=abs(Propbeam.^2);
B3=B3./max(B3(:));

 figure(1),imagesc(abs(Incidentbeam.^2)), axis off, axis square
figure(2),imagesc(Aperture), axis off, axis square
figure(3),imagesc(abs(Outbeam.^2)), axis off, axis square
figure(4),imagesc(abs(Propbeam.^2)), axis off, axis square
figure(5),imagesc(abs(Farfield.^2)), axis off, axis square
% figure(6), plot(B1((x+1)/2,:),'red'), hold on, plot(B3((x+1)/2,:),'black'), axis square
figure(7),imagesc(abs((1i.*k.*r.^2)./(2.*(flens/1000)))), axis off, axis square
```

FIGURE A.3: Optical field propagation code

Bibliography

[1] Robert G Hunsperger and Andrew J Maltenfort. *Optical wavelength division multiplexing/demultiplexing system*. US Patent 4,773,063. 1988.

[2] Yuanquan Wang et al. "Gigabit polarization division multiplexing in visible light communication". In: *Optics Letters* 39.7 (2014), pp. 1823–1826.

[3] Dave M Spirit, Andrew D Ellis, and Pete E Barnsley. "Optical time division multiplexing: Systems and networks". In: *IEEE Communications Magazine* 32.12 (1994), pp. 56–62.

[4] DJ Richardson, JM Fini, and LE Nelson. "Space-division multiplexing in optical fibres". In: *Nature Photonics* 7.5 (2013), pp. 354–362.

[5] Andrew R Chraplyvy. "Limitations on lightwave communications imposed by optical-fiber nonlinearities". In: *Journal of Lightwave Technology* 8.10 (1990), pp. 1548–1557.

[6] Les Allen et al. "Orbital angular momentum of light and the transformation of Laguerre-Gaussian laser modes". In: *Physical Review A* 45.11 (1992), p. 8185.

[7] Andrew Forbes. *Laser beam propagation: generation and propagation of customized light*. CRC Press, 2014.

[8] Wei-Chih Wang. *Electromagnetic wave theory*. Wiley, New York, 1986.

[9] Ole Steuernagel. "Equivalence between focused paraxial beams and the quantum harmonic oscillator". In: *American Journal of Physics* 73.7 (2005), pp. 625–629.

[10] J Durnin, JH Eberly, and JJ Miceli. "Comparison of Bessel and Gaussian beams". In: *Optics Letters* 13.2 (1988), pp. 79–80.

[11] D McGloin and K Dholakia. "Bessel beams: diffraction in a new light". In: *Contemporary Physics* 46.1 (2005), pp. 15–28.

[12] David Maurice Brink and George Raymond Satchler. "Angular momentum". In: (1968).

[13] AT O'neil et al. "Intrinsic and extrinsic nature of the orbital angular momentum of a light beam". In: *Physical Review Letters* 88.5 (2002), p. 053601.

[14] S Zhang and Z Yang. "Intrinsic spin and orbital angular momentum Hall effect". In: *Physical Review Letters* 94.6 (2005), p. 066602.

[15] Joseph W Goodman. *Introduction to Fourier optics*. Roberts and Company Publishers, 2005.

[16] Robert W Boyd. "The wavelength dependence of seeing". In: *JOSA* 68.7 (1978), pp. 877–883.

[17] Ronald L Fante. “Electromagnetic beam propagation in turbulent media”. In: *Proceedings of the IEEE* 63.12 (1975), pp. 1669–1692.

[18] Isaac I Kim, Bruce McArthur, and Eric J Korevaar. “Comparison of laser beam propagation at 785 nm and 1550 nm in fog and haze for optical wireless communications”. In: *Optical Wireless Communications III*. Vol. 4214. International Society for Optics and Photonics. 2001, pp. 26–38.

[19] Debbie Kedar and Shlomi Arnon. “Optical wireless communication through fog in the presence of pointing errors”. In: *Applied Optics* 42.24 (2003), pp. 4946–4954.

[20] HT Yura and WG McKinley. “Optical scintillation statistics for IR ground-to-space laser communication systems”. In: *Applied Optics* 22.21 (1983), pp. 3353–3358.

[21] Larry C Andrews and Ronald L Phillips. *Laser beam propagation through random media*. Vol. 152. SPIE Press Bellingham, WA, 2005.

[22] Guy Potvin. “General Rytov approximation”. In: *JOSA A* 32.10 (2015), pp. 1848–1856.

[23] Andrey Nikolaevich Kolmogorov. “Dissipation of energy in locally isotropic turbulence”. In: *Dokl. Akad. Nauk SSSR*. Vol. 32. 1. 1941, pp. 16–18.

[24] Hector E Nistazakis, Theodoros A Tsiftsis, and George S Tombras. “Performance analysis of free-space optical communication systems over atmospheric turbulence channels”. In: *IET Communications* 3.8 (2009), pp. 1402–1409.

[25] Larry C Andrews. “Field guide to atmospheric optics”. In: SPIE Bellingham. 2004.

[26] Xiaoming Zhu and Joseph M Kahn. “Free-space optical communication through atmospheric turbulence channels”. In: *IEEE Transactions on communications* 50.8 (2002), pp. 1293–1300.

[27] Robert R Beland. “Propagation through atmospheric optical turbulence”. In: *Atmospheric Propagation of Radiation* 2 (1993), pp. 157–232.

[28] Larry C Andrews et al. “Beam wander effects on the scintillation index of a focused beam”. In: *Atmospheric Propagation II*. Vol. 5793. International Society for Optics and Photonics. 2005, pp. 28–38.

[29] Linyan Cui and Lei Cao. “Theoretical expressions of long term beam spread and beam wander for Gaussian wave propagating through generalized atmospheric turbulence”. In: *Optik-International Journal for Light and Electron Optics* 126.23 (2015), pp. 4704–4707.

[30] Hemani Kaushal, VK Jain, and Subrat Kar. “Free-Space Optical Channel Models”. In: *Free Space Optical Communication*. Springer, 2017, pp. 41–89.

[31] David H Tofsted. “Outer-scale effects on beam-wander and angle-of-arrival variances”. In: *Applied Optics* 31.27 (1992), pp. 5865–5870.

[32] James H Churnside. “Aperture averaging of optical scintillations in the turbulent atmosphere”. In: *Applied Optics* 30.15 (1991), pp. 1982–1994.

[33] Italo Toselli et al. “Scintillation index of optical plane wave propagating through non-Kolmogorov moderate-strong turbulence”. In: *Optics in Atmospheric Propagation and Adaptive Systems X*. Vol. 6747. International Society for Optics and Photonics. 2007, 67470B.

[34] Larry C Andrews et al. “Theory of optical scintillation: Gaussian-beam wave model”. In: *Waves in Random Media* 11.3 (2001), pp. 271–291.

[35] LC Andrews, RL Phillips, and PT Yu. “Optical scintillations and fade statistics for a satellite-communication system”. In: *Applied Optics* 34.33 (1995), pp. 7742–7751.

[36] Troy T Leclerc et al. “Prediction of the ground-level refractive index structure parameter from the measurement of atmospheric conditions”. In: *Proc. SPIE*. Vol. 7685. 2010, 76850A.

[37] Marvin L Wesely. “The combined effect of temperature and humidity fluctuations on refractive index”. In: *Journal of Applied Meteorology* 15.1 (1976), pp. 43–49.

[38] Bun Oh et al. *Estimating optical turbulence using the PAMELA model*. Tech. rep. NAVAL RESEARCH LAB WASHINGTON DC, 2004.

[39] Steve Doss-Hammel et al. *A comparison of optical turbulence models*. Tech. rep. NAVAL RESEARCH LAB WASHINGTON DC, 2004.

[40] A. Arockia Bazil Raj, J. Arputha Vijaya Selvi, and S. Durairaj. “Comparison of different models for ground-level atmospheric turbulence strength (Cn2) prediction with a new model according to local weather data for FSO applications”. In: *Appl. Opt.* 54.4 (2015), pp. 802–815. DOI: 10.1364/AO.54.000802. URL: http://ao.osa.org/abstract.cfm?URI=ao-54-4-802.

[41] Larry C. Andrews David T. Wayne Paul Sauer Robert Crabbs Troy T. Leclerc Ronald L. Phillips. *Prediction of the ground-level refractive index structure parameter from the measurement of atmospheric conditions*. 2010. DOI: 10.1117/12.852426. URL: http://dx.doi.org/10.1117/12.852426.

[42] Sergey Bendersky, Norman S. Kopeika, and Natan Blaunstein. “Atmospheric optical turbulence over land in middle east coastal environments: prediction modeling and measurements”. In: *Appl. Opt.* 43.20 (2004), pp. 4070–4079. DOI: 10.1364/AO.43.004070. URL: http://ao.osa.org/abstract.cfm?URI=ao-43-20-4070.

[43] Ro S Lawrence, GR Ochs, and SF Clifford. “Measurements of atmospheric turbulence relevant to optical propagation”. In: *JOSA* 60.6 (1970), pp. 826–830.

[44] RE Good et al. “Atmospheric models of optical turbulence”. In: *Modeling of the Atmosphere*. Vol. 928. International Society for Optics and Photonics. 1988, pp. 165–187.

[45] Dan Sadot and Norman S Kopeika. “Forecasting optical turbulence strength on the basis of macroscale meteorology and aerosols: models and validation”. In: *Optical Engineering* 31.2 (1992), pp. 200–212.

[46] Yitzhak Yitzhaky, Itai Dror, and Norman S Kopeika. “Restoration of atmospherically blurred images according to weather-predicted atmospheric modulation transfer functions”. In: *Optical Engineering* 36.11 (1997), pp. 3064–3073.

[47] V Yu Bazhenov, MV Vasnetsov, and MS Soskin. “Laser beams with screw dislocations in their wavefronts”. In: *Jetp Lett* 52.8 (1990), pp. 429–431.

[48] Victor V Kotlyar et al. “Generation of phase singularity through diffracting a plane or Gaussian beam by a spiral phase plate”. In: *JOSA A* 22.5 (2005), pp. 849–861.

[49] Keiichi Sueda et al. “Laguerre-Gaussian beam generated with a multilevel spiral phase plate for high intensity laser pulses”. In: *Optics Express* 12.15 (2004), pp. 3548–3553.

[50] SSR Oemrawsingh et al. “Production and characterization of spiral phase plates for optical wavelengths”. In: *Applied Optics* 43.3 (2004), pp. 688–694.

[51] Andrew Forbes, Angela Dudley, and Melanie McLaren. “Creation and detection of optical modes with spatial light modulators”. In: *Advances in Optics and Photonics* 8.2 (2016), pp. 200–227.

[52] Victor Arrizón et al. “Pixelated phase computer holograms for the accurate encoding of scalar complex fields”. In: *JOSA A* 24.11 (2007), pp. 3500–3507.

[53] Eliot Bolduc et al. “Exact solution to simultaneous intensity and phase encryption with a single phase-only hologram”. In: *Optics Letters* 38.18 (2013), pp. 3546–3549.

[54] Christian Schulze et al. “Measurement of the orbital angular momentum density of light by modal decomposition”. In: *New Journal of Physics* 15.7 (2013), p. 073025.

[55] Christian Schulze et al. “Measurement of the orbital angular momentum density of Bessel beams by projection into a Laguerre–Gaussian basis”. In: *Applied Optics* 53.26 (2014), pp. 5924–5933.

[56] Angela Dudley, Igor A Litvin, and Andrew Forbes. “Quantitative measurement of the orbital angular momentum density of light”. In: *Applied Optics* 51.7 (2012), pp. 823–833.

[57] Christian Schulze et al. “Wavefront reconstruction by modal decomposition”. In: *Optics Express* 20.18 (2012), pp. 19714–19725.

[58] Oliver A Schmidt et al. “Real-time determination of laser beam quality by modal decomposition”. In: *Optics express* 19.7 (2011), pp. 6741–6748.

[59] Daniel Flamm et al. “Fast M 2 measurement for fiber beams based on modal analysis”. In: *Applied Optics* 51.7 (2012), pp. 987–993.

[60] Igor A Litvin et al. “Azimuthal decomposition with digital holograms”. In: *Optics Express* 20.10 (2012), pp. 10996–11004.

[61] atmospheric absorption spectrum Google Search. *atmospheric absorption spectrum Google Search*. 2018. URL: https://www.google.co.za/search?q=atmospheric+absorption+spectrum&tbm=isch&tbs=rimg:.

[62] A Arockia Bazil Raj. *Free space optical communication: system design, modelling, characterization and dealing with turbulence*. Walter de Gruyter DmbH & Co KG, 2016.

[63] Hemani Kaushal and Georges Kaddoum. "Optical communication in space: Challenges and mitigation techniques". In: *IEEE communication surveys % tutorials* 19.1 (2017), pp. 57–96.

[64] Lucie Dordová and Otakar Wilfert. "Calculation and comparison of turbulence attenuation by different methods". In: *Radioengineering* 19.1 (2010), pp. 162–167.

[65] Korhan Öztürk. "Simulation of free space optical links under different atmospheric conditions". PhD thesis. 2011.

[66] ThorLabs. *Transmission curve for a 10 mm thick uncoated sample of UV fused silica.* [Online; accessed July 2018, 2018]. 2018. URL: https://www.thorlabs.com/newgrouppage9.cfm?objectgroup_id=126.

[67] ThorLabs. *Reflectance curve for protected silver coated mirror.* [Online; accessed July 27, 2018]. 2018. URL: https://www.thorlabs.com/newgrouppage9.cfm?objectgroup_id=3831.

[68] Arnold Tunick et al. "Characterization of optical turbulence (Cn2) data measured at the ARL A_LOT facility". In: *US Army Research Laboratory, Adelphy, Md* (2005).

[69] Arnold Tunick. "Optical turbulence parameters characterized via optical measurements over a 2.33 km free-space laser path". In: *Optics Express* 16.19 (2008), pp. 14645–14654.

[70] Yijun Jiang et al. "Measurement of optical intensity fluctuation over an 11.8 km turbulent path". In: *Optics Express* 16.10 (2008), pp. 6963–6973.

[71] Arnold Tunick. "Statistical analysis of optical turbulence intensity over a 2.33 km propagation path". In: *Optics Express* 15.7 (2007), pp. 3619–3628.

[72] Arnold Tunick. "Analysis of free-space laser signal intensity over a 2.33 km optical path". In: *Proc. SPIE*. Vol. 6708. 2007, p. 670802.

[73] Wenhe Du et al. "Measurements of angle-of-arrival fluctuations over an 11.8 km urban path". In: *Laser and Particle Beams* 28.1 (2010), pp. 91–99.

[74] Shlomi Arnon. "Effects of atmospheric turbulence and building sway on optical wireless-communication systems". In: *Optics Letters* 28.2 (2003), pp. 129–131.

[75] Andrey Nikolaevich Kolmogorov. "Dissipation of energy in the locally isotropic turbulence". In: *Proc. R. Soc. Lond. A*. Vol. 434. 1890. The Royal Society. 1991, pp. 15–17.

[76] Alan E Willner et al. "Optical communications using orbital angular momentum beams". In: *Advances in Optics and Photonics* 7.1 (2015), pp. 66–106.

[77] Graham Gibson et al. “Free-space information transfer using light beams carrying orbital angular momentum”. In: *Optics Express* 12.22 (2004), pp. 5448–5456.

[78] Yoshinari Awaji, Naoya Wada, and Yasunori Toda. “Demonstration of spatial mode division multiplexing using Laguerre-Gaussian mode beam in telecom-wavelength”. In: *Photonics Society, 2010 23rd Annual Meeting of the IEEE*. IEEE. 2010, pp. 551–552.

[79] Mario Krenn et al. “Communication with spatially modulated light through turbulent air across Vienna”. In: *New Journal of Physics* 16.11 (2014), p. 113028.

[80] D Elser et al. “Feasibility of free space quantum key distribution with coherent polarization states”. In: *New Journal of Physics* 11.4 (2009), p. 045014.

[81] Glenn A Tyler and Robert W dd. “Influence of atmospheric turbulence on the propagation of quantum states of light carrying orbital angular momentum”. In: *Optics Letters* 34.2 (2009), pp. 142–144.

[82] Carl Paterson. “Atmospheric turbulence and orbital angular momentum of single photons for optical communication”. In: *Physical Review Letters* 94.15 (2005), p. 153901.

[83] Ronald L Phillips and Larry C Andrews. “Spot size and divergence for Laguerre Gaussian beams of any order”. In: *Applied Optics* 22.5 (1983), pp. 643–644.

[84] Sergey Bendersky, Norman S Kopeika, and Natan Blaunstein. “Atmospheric optical turbulence over land in middle east coastal environments: prediction modeling and measurements”. In: *Applied Optics* 43.20 (2004), pp. 4070–4079.

[85] I Litvin, L Burger, and A Forbes. “Self-healing of Bessel-like beams with longitudinally dependent cone angles”. In: *Journal of Optics* 17.10 (2015), p. 105614.

[86] Vladimir Belyi et al. “Bessel–like beams with z–dependent cone angles”. In: *Optics Express* 18.3 (2010), pp. 1966–1973.